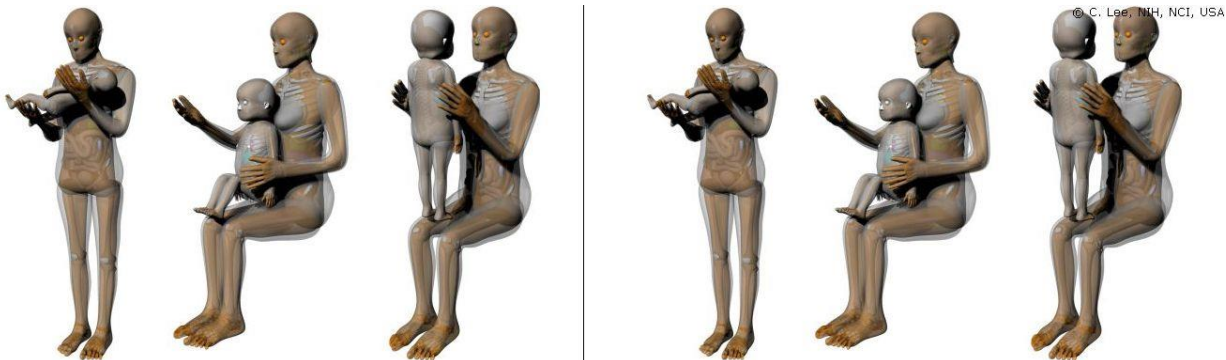
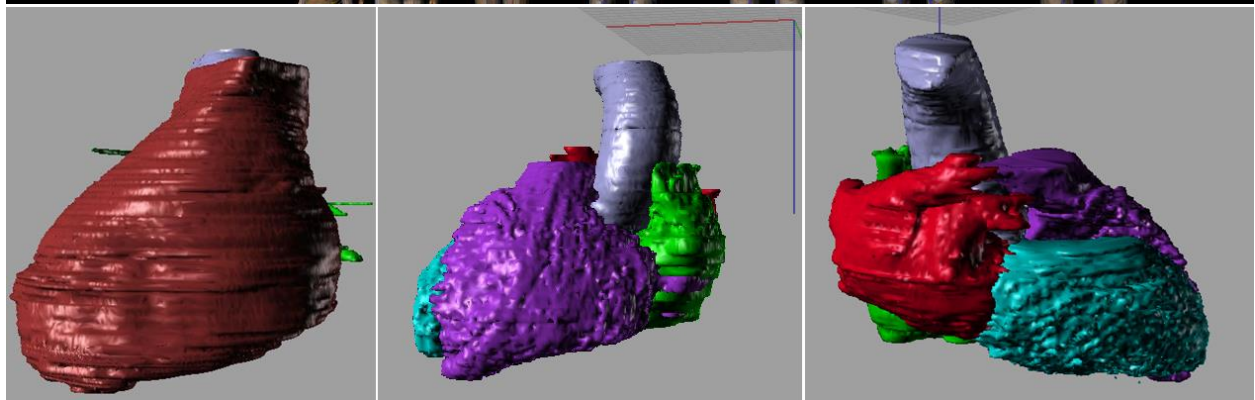


# 7<sup>th</sup> International Workshop on *Computational Human Phantoms*

22-24 July 2019

Neuherberg, Germany



**Book of Abstracts**

<https://cp2019.helmholtz-muenchen.de>

# Scientific Session

Monday, 22 July 2019

10:30 – 11:30	Opening Plenary Session Chair: X. George Xu, Co-Chair: Weibo Li
10:30	Opening Remarks
10:40	Invited Talk: Radiation dose and biological response: a modeller's perspective on a multi-scale issue Werner Friedland
11:30 – 12:30	Scientific Session "Phantom Development I" Chair: X. George Xu, Co-Chair: Weibo Li
11:30	Development of ICRP pediatric mesh-type reference computational phantoms Chansoo Choi, Chan Hyeong Kim, Bangho Shin, Haegin Han, Hanjin Lee, Xujia Zhang, Yeon Soo Yeom, Choonsik Lee, Thang Tat Nguyen, Wesley E. Bolch, Maria Zankl, Nina Petoussi-Henss, Beom Sun Chung, Rui Qiu, and Keith Eckerman
11:50	Incorporation of micro-CT based bone models into mesh-type reference Korean phantoms to improve skeletal dosimetry Bangho Shin, Chansoo Choi, Haegin Han, Yeon Soo Yeom, and Chan Hyeong Kim
12:10	The first series of Iranian BREP phantoms Elie Hoseinian-Azghadi, Laleh Rafat-Motavalli, Niloofar Rafat-Motavalli, and Hashem Miri-Hakimabad

# Radiation dose and biological response: a modeller's perspective on a multi-scale issue

Werner Friedland

Institute of Radiation Medicine, Helmholtz Zentrum München – German Center of Environmental Health, Neuherberg, Germany  
friedland@helmholtz-muenchen.de

**Abstract**—An overview on the multi-scale nature of radiation effects in biological context is given. This includes in particular the top-down modelling approaches as included in the PARTRAC[1] software tools. Energy depositions on nano- and micrometric scales are important determiners of biological radiation effects. Recent innovative experiments with focused ion beams, combined with model calculations, allow separation of their impact on cellular radiation effects.

**Index Terms**—Monte Carlo modeling, track structure calculations, radiation quality, DNA damage, DNA damage response

## I. INTRODUCTION

Ionizing radiation is widely used in medicine, science and technology. Its medical applications serve both diagnostic and therapeutic purposes: Diagnostic methods based on ionizing radiation include X-ray imaging, computed tomography, positron or single photon emission tomography and other techniques. Therapeutic applications include external radiotherapy using photon, electron, proton or ion beams or brachytherapy with short-range radiation sources placed into or close to the cured region, for the curative treatment of cancer or palliative treatment of painful diseases.

In optimizing these and future applications, a balance must be found between benefits and potential long-term health risks of radiation exposure. The health risks follow from the fact that ionizing radiation elicits a number of adverse biological effects, including its pro-carcinogenic action and enhancement of cardiovascular diseases.

Detailed understanding of the mechanisms and processes that underpin the biological effects of ionizing radiation is needed in order to allow the benefits of radiation applications being fully exploited and at the same time its negative effects being reduced as far as possible. Mechanistic modelling plays an important role towards achieving these goals. Modelling serves as a useful complement to experimental studies: It integrates the knowledge gained from the experiments. It allows alternative hypotheses on the underlying processes and mechanisms to be tested. Modelling results inform experimental research on conditions and endpoints where additional experiments should be performed to foster the existing knowledge or rule out alternative hypotheses. Modelling also allows interpolations between measurements and extrapolations to conditions not measured yet or experimentally not accessible at all.

Figure 1. Scales of radiation effects in biological context. The development of radiation effects proceeds in multiple stages that cover distinct time scales and are related to objects of generally increasing size. The timescales, objects and processes are largely exemplary items. The underlying processes are theoretically assessed by various model approaches that typically also utilize model representations of the objects.

Stage	Time [s]	Size [m]	Object	Process	Model
physical	10 <sup>-20</sup>	10 <sup>-15</sup>	α-particle	nuclear reaction	cross section
	10 <sup>-15</sup>	10 <sup>-10</sup>	atom	ionization excitation	track structure
physico-chemical			molecule	dissociation	radiation chemistry
			radical	diffusion reaction	
biochemical	10 <sup>-5</sup>	10 <sup>-9</sup>	DNA helix	breakage	initial damage
			biomolecule	phosphorylation	
biological	10 <sup>0</sup>	10 <sup>-6</sup>	gene	upregulation	damage response
			chromosome	aberration	systems biology
medical	10 <sup>5</sup>	10 <sup>-3</sup>	organelle	dysfunction	treatment planning
			cell	survival	
epidemiological	10 <sup>10</sup>	10 <sup>0</sup>	tissue	inflammation	disease and risk
			organ	cancer	
			organism	death	
			population	life expectancy	

## II. MULTI-SCALE NATURE OF RADIATION AND ITS EFFECTS

Ionizing radiation affects biological systems over multiple spatial as well as temporal scales (Figure 1) [2]. These scales are linked with objects that undergo modifications by certain processes, and usually specific modelling approaches are adopted to describe the underlying mechanisms. The fastest events with temporal scales down to  $\sim 10^{-20}$  s or even shorter are processes which involve the atomic nucleus, such as fragmentation of an incident  $\alpha$ -particle upon hitting another nucleus. This spatial scale is also related to radioactive decay events that lead to the emission of energetic helium nuclei (alpha particles), electrons or positrons (beta particles), photons (gamma rays), or other particle types in further decay modes. However, time scales of these events cover essentially the whole range shown in Figure 1, indicating that the listed relation of objects and processes to time scales is not mandatory. Key events setting the scene for the biological effects of ionizing radiation are ionizations and excitations of individual atoms and molecules within the traversed medium; these processes occur on spatial scales given by the size of atoms and small molecules,  $\sim 10^{-10}$  m, and temporal scales of  $\sim 10^{-15}$  s. Within the subsequent physico-chemical phase up to

$\sim 10^{-12}$  s, reactive species are produced from excited and ionized water molecules, which are major constituents of most biological materials. During the following chemical phase, up to  $\sim 10^{-6}$  s, biologically important macromolecules are damaged via attacks of radicals (primarily hydroxyl radicals,  $\cdot\text{OH}$ ) in addition to the damage resulting from direct energy deposits. The target molecules include, first of all, DNA within the cell nucleus, the carrier of the cell's genetic information. Although the total length of a human DNA molecule is a few metres, it is highly compacted within a cell nucleus into chromosomes with micrometre dimensions. The initial radiation damage on sub-cellular scales is induced within microseconds to seconds, but the cell possesses a number of dedicated repair pathways that aim at removing the damage and restoring the original functionality; these repair processes typically operate on timescales of seconds to hours. Unremoved damage to biologically important macromolecules and/or the shift in redox balance upon radiation exposure may then manifest over the timescales of hours to days in malfunctioning of organelles, induction of mutations, or even cell death. At the tissue level, inflammation or diverse types of tissue damage can be observed, corresponding to spatial scales of millimetres to decimetres and a broad range of temporal scales, hours to years. On even larger and longer scales, radiation-induced effects include organ dysfunction and enhanced or accelerated induction of cancer or cardiovascular diseases. Spatial and temporal scales may be even further extended when risks for populations are considered, e.g., in the framework of nuclear waste disposal strategies. All the mentioned effects depend on the quality of radiation (particle type and energy), applied dose, dose rate, and in the context of medical applications on the selected fractionation scheme.

Being a multi-scale issue, biological effects of ionizing radiation require multi-scale modelling approaches. Model approaches addressing particular processes and topics are listed in the last column of Figure 1; moreover, model representations of objects (e.g. DNA, tissue, etc.) are needed for the assessment of radiation effects. Cross section models provide datasets of interaction probabilities for the traversed medium in dependence on the incident particle type and its energy. They are used as input for track structure models that aim at reproducing detailed patterns of energy deposition and their stochastic nature. The initial radiation damage is assessed then by combining the resulting track structure with the structure of the relevant target; some models work with a short piece of DNA, while advanced approaches include the total genomic DNA inside a single cell nucleus. The physical track structures are complemented by a chemistry model for indirect damage due to radical attack, including a target model and assumptions on the susceptibility of the target to damage induction.

During the past three decades a variety of track structure models have been developed and used for calculations of radiation-induced DNA damage [3]; this work is focused on the PARTRAC code and its modules [1]. In some models, endpoints such as cell killing have been linked with initial damage in a semi-phenomenological manner using suitable parameterisations, which offers simplicity, efficiency and robustness needed for applications in treatment planning [4]. A mechanism-oriented, dynamic simulation of DNA damage

response has been addressed by a few research groups only; this computationally expensive approach may provide data for the integration into complementary top-down approaches of biology-based models of carcinogenesis [5].

In general, radiation effects are presented and assessed in dependence on the absorbed dose. However, since the main target objects are of nanometric (DNA molecule) or micrometric (cell nucleus) size, the distribution of energy in corresponding volumina is of particular importance. This is reflected in nanodosimetric analyses, where the numbers and sizes of ionization clusters in nm-sized spheres, and microdosimetric analyses, where energy depositions in (sub-)cellular volumes, are related to biological effects, such as DNA damage in relation to the linear energy transfer (LET) [6]. Changing radiation quality, e.g. varying energy (and maybe also type) of fast ions, alters nanodosimetric as well as microdosimetric properties, and thus does not allow separation of the impact of both scales on the resulting effect. Recent innovative experiments with focused ion beams have overcome this limitation. Focusing low-LET protons to carbon ion-like microscale dose distributions increases induction of dicentric and cell killing whereas focusing of high-LET carbon ions has the opposite effect [7, 8]. These experimental results continue to challenge the DNA damage response simulation within PARTRAC [9].

## REFERENCES

- [1] W. Friedland, M. Dingfelder, P. Kunderát and P. Jacob, "Track structures, DNA targets and radiation effects in the biophysical Monte Carlo simulation code PARTRAC," *Mutat. Res.*, vol. 711, pp. 28-40, 2011.
- [2] W. Friedland and P. Kunderát, 2018. "Stochastic multi-scale modeling of biological effects induced by ionizing radiation" in *A Guide to Outcome Modeling in Radiotherapy and Oncology*, I. El Naqa, Ed., Boca Raton, CRC Press, 2018, ch. 10, pp. 147-180.
- [3] H. Nikjoo, S. Uehara, D. Emfietzoglou and F. A. Cucinotta, "Track-structure codes in radiation research," *Radiat. Measurements*, vol. 41, pp. 1052-1074, 2006.
- [4] T. Friedrich, M. Durante and M. Scholz, "Modeling cell survival after photon irradiation based on double-strand break clustering in megabase pair chromatin loops," *Radiat. Res.*, vol. 178, pp. 385-394, 2012.
- [5] W. Rühm, M. Eidemüller and J. C. Kaiser, "Biologically-based mechanistic models of radiation-related carcinogenesis applied to epidemiological data," *Int. J. Radiat. Biol.*, vol. 93, pp. 1093-1117, 2017.
- [6] W. Friedland, E. Schmitt, P. Kunderát, M. Dingfelder, G. Baiocco, et al., "Comprehensive track-structure based evaluation of DNA damage by light ions from radiotherapy-relevant energies down to stopping," *Sci. Rep.* vol. 7:45161, 2017.
- [7] T. E. Schmid, W. Friedland, C. Greubel, S. Girst, J. Reindl et al., "Sub-micrometer 20 MeV protons or 45 MeV lithium spot irradiation enhances yields of dicentric chromosomes due to clustering of DNA double-strand breaks," *Mutat. Res.*, vol. 793, pp. 30-40, 2015.
- [8] T. Friedrich, K. Ilicic, C. Greubel, S. Girst, J. Reindl et al., "DNA damage interactions on both nanometer and micrometer scale determine overall cellular damage," *Sci. Rep.* vol. 8:16063, 2018.
- [9] W. Friedland, P. Kunderát, E. Schmitt, J. Becker, K. Ilicic, et al., "Modeling studies on dicentric induction after sub-micrometer focused ion beam grid irradiation," *Radiat. Prot. Dosim.*, vol. 183, pp. 40-44, 2019.

# Development of ICRP Pediatric Mesh-type Reference Computational Phantoms

Chansoo Choi<sup>1</sup>, Chan Hyeong Kim<sup>1,\*</sup>, Bangho Shin<sup>1</sup>, Haegin Han<sup>1</sup>, Hanjin Lee<sup>1</sup>, Xujia Zhang<sup>1</sup>, Yeon Soo Yeom<sup>2</sup>, Choonsik Lee<sup>2</sup>, Thang Tat Nguyen<sup>3</sup>, Wesley E. Bolch<sup>4</sup>, Maria Zankl<sup>5</sup>, Nina Petoussi-Henss<sup>5</sup>, Beom Sun Chung<sup>6</sup>, Rui Qiu<sup>7</sup>, and Keith Eckerman<sup>8</sup>

<sup>1,\*</sup>Department of Nuclear Engineering, Hanyang University, 04763, 222 Wangsimni-ro, Seongdong-gu, Seoul, Republic of Korea

<sup>2</sup>Division of Cancer Epidemiology & Genetics, National Cancer Institute, 9609 Medical Center Drive, Bethesda, MD 20892-9760, USA

<sup>3</sup>School of Nuclear Engineering and Environmental Physics, Hanoi University of Science and Technology, 1 Dai Co Viet road, Hai Ba Trung district, Hanoi, Vietnam

<sup>4</sup>J. Crayton Pruitt Family Department of Biomedical Engineering, University of Florida, P.O. Box 116131, Gainesville, FL 32611-6131, USA

<sup>5</sup>Helmholtz Zentrum München German Research Center for Environmental Health, Institute of Radiation Protection, Ingolstädter Landstraße 1, 85764 Neuherberg, Germany

<sup>6</sup>Department of Anatomy, Ajou University School of Medicine, 16499, 206 Worldcup-ro, Suwon, Republic of Korea

<sup>7</sup>Department of Engineering Physics, Tsinghua University, 100084, Beijing, P.R. China

<sup>8</sup>Environmental Sciences Division, Oak Ridge National Laboratory, Oak Ridge, TN 37831-6480, USA

\*Corresponding author: [chkim@hanyang.ac.kr](mailto:chkim@hanyang.ac.kr)

**Abstract**—In 2016, the International Commission on Radiological Protection (ICRP) formulated a Task Group (TG) 103 with the purpose to develop new mesh-type reference computational phantoms (MRCPs) to overcome the limitations of the currently used voxel-type reference computational phantoms. TG 103 recently completed developing adult MRCPs and has undertaken to develop pediatric MRCPs. This paper reports the current progress of the project for the pediatric MRCPs.

**Index Terms**—ICRP; reference phantoms; pediatric; mesh; Monte Carlo

## I. INTRODUCTION

The International Commission on Radiological Protection (ICRP) has used the adult and pediatric voxel-type reference computational phantoms (VRCPs) [1–2] to calculate dose values for various exposure scenarios of interest in the field of radiation protection [3–4]. However, the VRCPs do not precisely represent very thin or small organs/tissues which are below their voxel resolutions (= hundreds of micrometers to several millimeters), leading to unreliable dose calculations particularly for weakly penetrating radiations. Moreover, it is difficult to deform them to different body sizes or postures. In 2016, to address the limitations of the VRCPs, the ICRP formulated a Task Group (TG) 103 under Committee 2 with the purpose to develop new adult and pediatric mesh-type reference computational phantoms (MRCPs) by converting the VRCPs into a high-quality/fidelity mesh format. Recently, TG 103 completed developing the adult MRCPs [5] and a report for the phantom distribution is now in a near-final stage before the publication. As the development of adult MRCPs was completed, the TG 103 has undertaken to develop the pediatric MRCPs. In this paper, we report the progress of the project for developing the pediatric MRCPs, explaining the current progress, raised issues, and future plan.

## II. METHODS

The overall procedure for the development of pediatric MRCPs is: (1) to produce the high-quality polygon-mesh (PM) replicas of pediatric VRCPs; (2) to include the blood content in the organs/tissues; (3) to construct the complex organs/tissues; and (4) to characterize the constructed pediatric MRCPs. Currently, steps 1 and 2 have been completed, and step 3 is in progress. Details of each step are as follows:

**Step 1**—In this step, the high-quality PM replicas of pediatric VRCPs are produced using the UF/NCI pediatric phantom series [6] as well as the pediatric VRCPs. Note that the UF/NCI phantoms are the original form of pediatric VRCPs before the voxelization process and that they are in NURBS/PM format which can be more easily converted into PM models than voxel structures. First, the UF/NCI pediatric phantoms were converted into primitive PM models via surface rendering and refinement procedures using the 3D programs. Then, the organs/tissues of the PM models were adjusted to those of pediatric VRCPs, completing the development of the high-quality PM replicas of which organs/tissues faithfully preserve the topology of those of pediatric VRCPs.

**Step 2**—In this step, the organs/tissues are modified to include the blood content. The pediatric VRCPs were constructed based on reference values given in Table 2.8 of ICRP *Publication* 89 [7] which are the masses of organ/tissue parenchyma, *i.e.*, not including blood content. However, in a living person, a large portion of blood in small vessels and capillaries is distributed in the organs/tissues. To consider the intra-organ blood content, it was decided to adjust the PM phantoms to match the organ/tissue masses and densities inclusive of the blood content. For this, the organ/tissue masses and densities were recalculated by using the regional blood volume fractions for children and adolescents provided by

Wayson *et al.* [8]. Then, the organs/tissue volumes of PM model were globally enlarged, thereby matching the blood-inclusive reference masses and densities.

**Step 3**—In this step, the complex organs/tissues of the phantoms are constructed. While most of the simple organs/tissues of the pediatric MRCPs can be directly constructed from the pediatric VRCPs through steps 1 and 2, several organs/tissues (*e.g.*, eyes, fontanelle cartilage, spine and hand/foot bones, teeth, intestines), which contain anatomical or technical issues due to their complex or small structure, cannot be constructed by the direct conversion process; therefore, they should be remodeled or newly developed. The issues were also discussed in the ICRP Committee 2 meeting in 2018 and the decisions are as follows.

For the eyes, considering the complicated changes in ocular dimensions with growth, it was decided to develop a set of detailed models for pediatrics by using the specific dimensions for each age. Accordingly, the pediatric eye models were developed based on nine anatomical parameters determined from various scientific literatures for the eye in each age, following the approach used for the development of the eye model installed in adult MRCPs. The developed models were then incorporated into the phantoms considering the position of eye socket in cranium.

The fontanelle cartilage models in the newborn and 1-year-old cranium were decided to be remodeled due to its abnormally large size. For this, the anterior and posterior fontanelle sizes and suture widths were determined from various scientific literatures, and the fontanelle cartilages were then carefully remodeled following these parameters.

For the spine and hand/foot bones of 1-, 5-, 10-, and 15-year-old phantoms, due to their low quality, it was decided to install the existing high-quality adult bone models after the adjustments to the bone models of pediatric VRCPs. Note that intervertebral cartilage and spinal cord were also remodeled for the consistency with the new spine model.

For the intestines, it was found that the masses/densities of luminal contents are significantly different from the reference masses or conventional content densities (*i.e.*, 1.03 g/cm<sup>3</sup>); thus, it was decided to modify them to match both the reference masses and conventional densities. The small intestines were simply modified following the similar approach used in step 2. The colons, however, cannot be modified by the same approach due to the dislocations at the subdivision boundaries of the colons (*i.e.*, right colon, left colon, and rectosigmoid colon). The colon models are thus currently being remodeled in the shape of connected truncated cone models which can match the reference masses and densities of each region.

For the teeth, it was decided to install detailed models for use in dose reconstruction by electron paramagnetic resonance (EPR) or electron spin resonance (ESR) dosimetry. For this, the eruption period of each tooth and anatomical parameters of components that consist of each tooth were determined from various scientific literatures. Based on these parameters, the

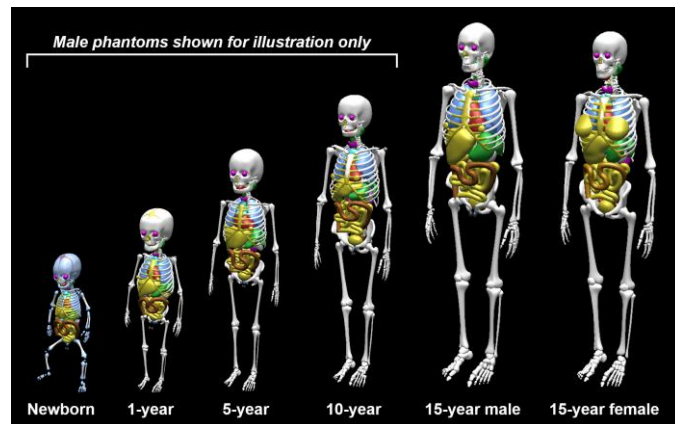


Figure 1. Preliminary results for the development of pediatric MRCPs.

detailed tooth models are currently being developed, and will be incorporated into the phantoms.

In addition, the muscle, blood vessels, and lymphatic nodes will be constructed with methodology similar to the one used for the construction of adult MRCPs. Finally, micron-thick target and source regions within skin, urinary bladder, and alimentary and respiratory tract systems will be included in the phantoms by using the *offset* function of the *Rapidform* software (INUS Technology Inc., Korea). Figure 1 shows the preliminary results of the development of pediatric MRCPs.

**Step 4**—In this step, the constructed pediatric MRCPs are characterized. For this, first, the organ-depth distribution and chord-length distribution will be calculated to observe the geometric similarity between the pediatric VRCPs and MRCPs. Then, the dose coefficients will be calculated for some selected external and internal exposures to investigate the dosimetric impacts of the developed phantoms.

### III. CONCLUSION

In this paper, the progress of the project for developing the pediatric MRCPs is explained with issues, current progress, and future plan. TG 103 is currently in Step 3, and the construction is planned to be completed by the CP 2019 workshop. In the workshop, we are planning to discuss the developed pediatric MRCPs and their dosimetric impacts.

### REFERENCES

- [1] ICRP, “Adult reference computational phantoms,” ICRP Publication 110, *Ann. ICRP*, 2009.
- [2] ICRP, “Pediatric reference computational phantoms,” in preparation for publication.
- [3] ICRP, “Conversion coefficients for radiological protection quantities for external radiation exposures,” ICRP Publication 116, *Ann. ICRP*, 2010.
- [4] ICRP, “The ICRP computational framework for internal dose assessment for reference adults: specific absorbed fractions,” ICRP Publication 133, *Ann. ICRP*, 2016.
- [5] C. H. Kim *et al.*, “New mesh-type phantoms and their dosimetric applications, including emergencies,” *Ann. ICRP*, vol. 47, pp. 45-62, 2018.
- [6] C. Lee *et al.*, “The UF family of reference hybrid phantoms for computational radiation dosimetry,” *Phys. Med. Biol.*, vol. 55, pp. 339-363, 2010.
- [7] ICRP, “Basic anatomical and physiological data for use in radiological protection: reference values,” ICRP Publication 89, *Ann. ICRP*, 2002.
- [8] M. B. Wayson *et al.*, “Suggested reference values for regional blood volumes in children and adolescents,” *Phys. Med. Biol.*, vol. 63, 155022, 2018.

# Incorporation of Micro-CT Based Bone Models into Mesh-type Reference Korean Phantoms to Improve Skeletal Dosimetry

Bangho Shin<sup>1</sup>, Chansoo Choi<sup>1</sup>, Haegin Han<sup>1</sup>, Yeon Soo Yeom<sup>2</sup>, and Chan Hyeong Kim<sup>1,\*</sup>

<sup>1</sup>\*Department of Nuclear Engineering, Hanyang University, 222 Wangsimni-ro, Seongdong-gu, Seoul 04763, Korea

<sup>2</sup>Division of Cancer Epidemiology & Genetics, National Cancer Institute, 9609 Medical Center Drive, Bethesda, MD 20892-9760, USA

\*Corresponding author: chkim@hanyang.ac.kr

**Abstract**—In the present study, a set of site-specific detailed bone models for Korean were developed for 32 skeletal sites and fully incorporated into the Mesh-type Reference Korean Phantoms (MRKPs). The MRKPs incorporating the detailed bone models were then used to calculate electron absorbed fractions (AFs) to red bone marrow and bone endosteum for cortical bone as a source, and the calculated values were compared with the results of a previous research.

**Index Terms**—skeletal dosimetry; micro-CT images; mesh phantoms; red bone marrow; bone endosteum

## I. INTRODUCTION

Recently a set of new Korean adult reference computational phantoms, called Mesh-type Reference Korean Phantoms (MRKPs), were developed for use in calculation of organ/tissue doses and effective doses to the Korean adult population for radiation protection purpose [1]. The MRKPs were constructed in an advanced geometry format, *i.e.*, tetrahedral mesh geometry, to overcome the limitations of the previous voxel-type Korean reference phantoms due to the limited voxel resolutions and the nature of voxel geometry. The MRKPs are very detailed model, and even the micron-scale radiosensitive target and source regions in the alimentary and respiratory tract systems, skin, eye lens, and urinary bladder are all defined in the MRKPs.

The detailed structures of the skeletal target tissues (*i.e.*, red bone marrow (RBM) and bone endosteum (BE)), however, due to their complex microscopic structure, were not defined in the spongiosa regions of the MRKPs. Therefore, the use of approximate techniques for skeletal dosimetry [2] was inevitable to estimate doses to the skeletal target tissues for the MRKPs. In order to overcome this limitation, we have developed a set of site-specific detailed bone models for Korean based on the micro-CT data of Chinese adult cadavers [3] and incorporated the detailed bone models into the MRKPs. The MRKPs incorporating the detailed bone models were then used to calculate electron absorbed fractions (AFs) to the RBM and BE for the cortical bone (CB) as a source and the calculated values were compared with the results of Gao *et al.* [3].

## II. METHODS

### A. Development of Site-specific Detailed Bone Models

In the present study, the site-specific detailed bone models for Korean adult were developed based on the micro-CT images of trabecular bone for 32 skeletal sites of Chinese adult male and female cadavers [3]. The micro-CT image for each skeletal site contains  $63 \times 63 \times 63$  ( $= 250,047$ ) voxels; the voxel size is  $19 \times 19 \times 19 \mu\text{m}^3$ . The four skeletal tissues (RBM, yellow bone marrow (YBM), trabecular bone (TB), and BE) were modelled in the micro-CT images as shown in Figure 1. First, the TB (high density) and marrow cavity (low density) were simply segmented by using the contrast threshold method. In the marrow cavity, the RBM and YBM were randomly distributed while matching the reference RBM mass of Korean for each skeletal site. Finally, the BE was defined in the marrow cavity by using a multi-resolution approach; that is, the marrow cavity region was subdivided into  $1\text{-}\mu\text{m}^3$  voxels and the voxels, of which centers were within  $50 \mu\text{m}$  from the trabecular bone surface, were defined as BE.

### B. Incorporation of Detailed Bone Models into MRKPs

The site-specific detailed bone models were incorporated into the MRKPs by using the parallel world geometry feature of the Geant4 Monte Carlo simulation code [4]. The site-specific detailed bone models were registered in the *real world* according to the positions of each site, and MRKPs was registered in the *parallel world* with void in spongiosa regions. Note that the organs/tissues are in tetrahedral mesh formats except for the spongiosa regions. In this way, the spongiosa

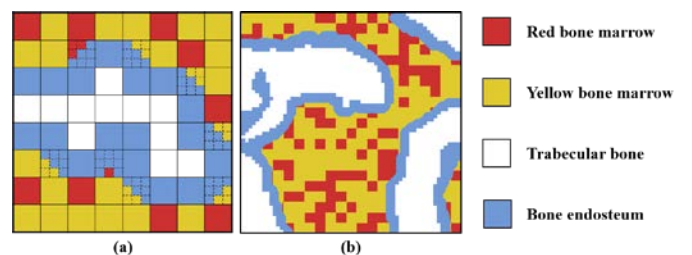


Figure 1. The bone endosteum (BE) definition method of the present study (a) and the BE defined spongiosa model of the frontal bone for male using the method (b).

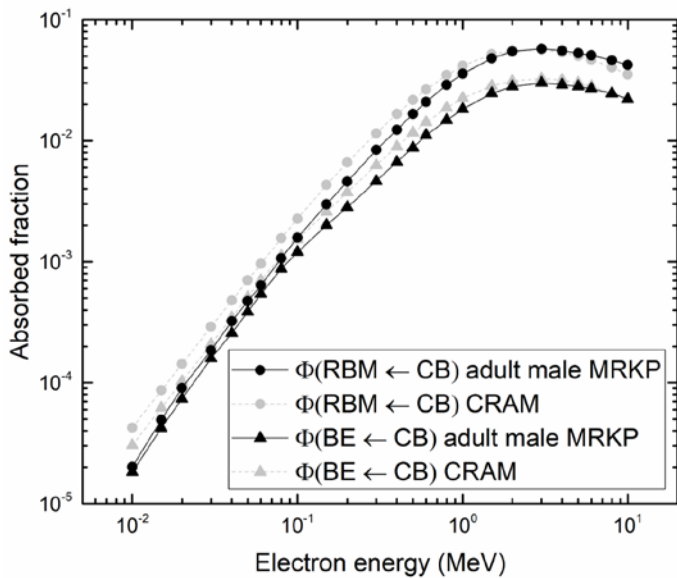


Figure 2. Electron absorbed fractions (AFs) to red bone marrow (RBM) and bone endosteum (BE) for the cortical bone (CB) as source region.

models in voxel formats were successfully incorporated into the MRKPs, maintaining the smooth surfaces of the mesh-based CBs.

### C. Monte Carlo Simulation for Skeletal Dose Calculations

The MRKPs with the site-specific detailed bone models were used to calculate AFs for the RBM and BE as the source is CB for electron exposures by performing Monte Carlo simulations with the Geant4 code. The user limit on the range cut value for secondary production and maximum step length were set as 0.1  $\mu\text{m}$  and 1  $\mu\text{m}$ , respectively, considering the microscopic structures. The electron AFs were calculated for 25 energy points ranging from 0.01 MeV to 10 MeV, and the statistical relative errors were within 1% for all the energy points.

## III. RESULTS

Figure 2 shows the electron AFs to the RBM and BE for cortical bone as a source calculated with the adult male MRKP as an example, along with those calculated with the voxel-type Chinese Reference Adult Male (CRAM) phantom by Gao *et al.* [3]. For low energies, the AFs calculated with the adult male MRKP are lower than those of the CRAM phantom; the maximum differences are  $\sim 2.1$  times and  $\sim 1.7$  times at 0.01 MeV for RBM and BE, respectively. These differences are mainly due to the difference in the geometry format of the phantoms (*i.e.*, mesh vs. voxel). The overestimation of AFs for the CRAM phantom is occurred by the stair-stepped shape of the voxels [5] which increases the interface surface area between CB and spongiosa regions. At high energies, on the other hand, the AFs calculated with the adult male MRKP are slightly higher than those of the CRAM phantom by up to  $\sim 20\%$  and  $\sim 3\%$  at 10 MeV for RBM and BE, respectively. These differences are due to the crossfire effect that was considered in this study by fully incorporating all the 32 spongiosa models into the phantom. The AFs to BE, which

showed the smaller differences than RBM, are due to the differences in defining the BE layer. Note that Gao *et al.* [3] overestimated the BE layer owing to the voxel resolution of 19  $\mu\text{m}$ . The overestimation of the BE layer resulted in the overestimation of the AFs.

## IV. CONCLUSION

In the present study, the site-specific detailed bone models for the 32 skeletal sites were developed for Korean phantoms and fully incorporated into the spongiosa regions of the MRKPs. To our knowledge, this is the first study in which the voxel-based detailed bone models are fully incorporated into the mesh phantoms and used in Monte Carlo dose calculation without voxelization. The results of this study show that tetrahedral mesh phantoms coupled with the detailed bone models significantly improve the accuracy of dosimetry for skeletal target tissues (*i.e.*, RBM and BE).

## ACKNOWLEDGMENT

The authors would like to thank Prof. Rui Qiu and Dr. Li Ren of Department of Engineering Physics, Tsinghua University for providing the micro-CT images of spongiosa bones for adult male and female.

## REFERENCES

- [1] C. Choi, T. T. Nguyen, Y. S. Yeom, et al., "Mesh-type reference Korean phantoms (MRKPs) for adult male and female for use in radiation protection dosimetry," *Phys. Med. Biol.*, <https://doi.org/10.1088/1361-6560/ab0b59>, 2019.
- [2] C. Lee, C. Lee, A. P. Shah, and W. Bolch, "An assessment of bone marrow and bone endosteum dosimetry methods for photon sources," *Phys. Med. Biol.*, vol. 51, pp. 5391-5407, 2006.
- [3] S. Gao, L. Ren, R. Qiu, et al., "Electron absorbed fractions in an image-based microscopic skeletal dosimetry model of chinese adult male," *Rad. Prot. Dos.*, vol. 175, pp. 450-459, 2017.
- [4] S. Agostinelli, J. Allison, K. Amako, et al., "Geant4—a simulation toolkit," *Nucl. Instrum. Methods. Phys. Res. A*, vol. 506, pp. 250-303, 2003.
- [5] D. A. Rajon, P. W. Patton, A. P. Shah, C. J. Watchman, and W. E. Bolch, "Surface area overestimation within three-dimensional digital images and its consequence for skeletal dosimetry," *Med. Phys.*, vol. 29, pp. 682-693, 2002.

# The first series of Iranian BREP phantoms

Elie Hoseinian-Azghadi, Laleh Rafat-Motavalli, Niloofar Rafat-Motavalli, and Hashem Miri-Hakimabad\*

Physics Department, Faculty of Science, Ferdowsi University of Mashhad, Mashhad, Iran

e-mail address if desired:

\*Corresponding author: mirihakim@um.ac.ir

**Abstract**— A new family of boundary representation (BREP) reference phantoms, based on the Iranian reference masses for adults of both genders and also three non-reference Iranian pediatric phantoms were developed. We further extended this phantom series to include pregnant women with fetuses of various ages and weight percentiles for radiation protection purposes.

**Index Terms**—BREP phantoms; reference phantoms; pediatric phantoms; other ethnic groups

## I. INTRODUCTION

Looking at the soaring mountains of computational phantoms' applications from where we stand on the hillside, the highest visible mountaintop is the scientific contribution of personalized phantoms in medicine. As an Iranian research group, we are standing on the first station through the climbing route which is the development of Iranian BREP phantoms. Toward this goal, we could get a detailed understanding of human anatomy, and an invaluable experience in reading medical images such as CT and MR, and in 3D graphical modeling with polygon mesh surfaces and NURBS. Also, we explored systematic anatomical differences between Iranians and other ethnic/racial groups. Further, we gathered a large library of HU values, shapes and locations for various organs and tissues. In addition, our perception of which components of secondary radiation could be important was influenced by performing dosimetric calculations for these phantoms in different exposure scenarios. Here, we have a better understanding of our next stations toward the mountaintop which we think are (1) auto-segmentation, (2) real-time specific-posture modeling, (3) fast Monte Carlo simulation, and (4) radiobiological modeling. Through this way, the inscriptions left by previous investigators were our guides [1-3], and we would be so proud to share our experiences with this workshop.

## II. METHODS

### A. Anthropometric characteristics of Iranian individuals

Total weight, height and extremities and trunk weight, were obtained from a commercially available body analyzer. The collected data showed a normal distribution of weight and height which confirmed appropriate homogenous sampling of individuals.

### B. Specifications of internal organs

The CT images of chest-abdomen-pelvis and head-neck of 100 patients were provided and the contours of their distinguishable organs were determined [4]. The organ volumes were then evaluated and utilized for determination of reference organs' mass of Iranian individuals.

### C. Conversion of patient-specific models to reference phantoms

Two adult male and female volunteers were recruited which had heights and weights close to Iranian average values. The total body of volunteers were partially imaged using a 1.5T Siemens MagneTom vision. The patient-specific models were then converted to reference models using 3D tools in Rhinoceros software.

### D. Pregnant females

The adult female reference phantom was then converted to pregnant models at gestational ages using the method discussed in [5-8].

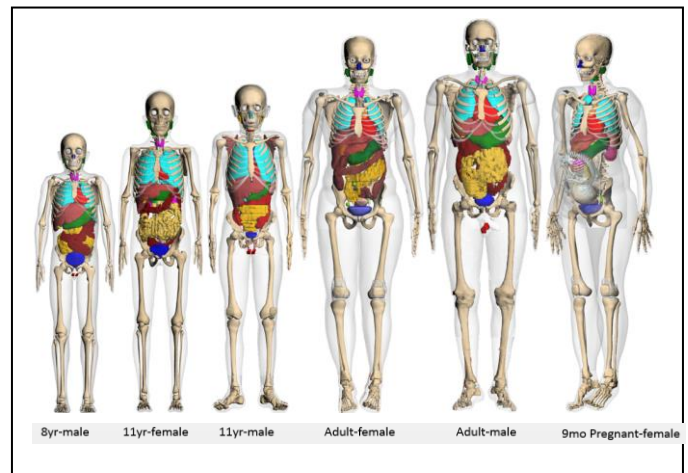


Figure 1. 3D front view of Iranian computational phantoms.

## III. RESULTS

A family of BREP reference phantoms are presented including two adult male and female reference phantoms, a subgroup of pregnant reference phantoms at 3, 6 and 9 months of gestation, and three non-reference pediatric phantoms. The

organs' mass values of the reference models are conformed to the reference data of Iranian population.

The pregnant subgroup involves fetuses at 10<sup>th</sup>, 50<sup>th</sup>, and 90<sup>th</sup> growth percentiles. Moreover, the fetal models include age-specific skeletal structures pertained to the ossification of fetal skeleton. The non-reference pediatric models also include two 11 years old male and female models, in addition to an 8 years old male phantom.

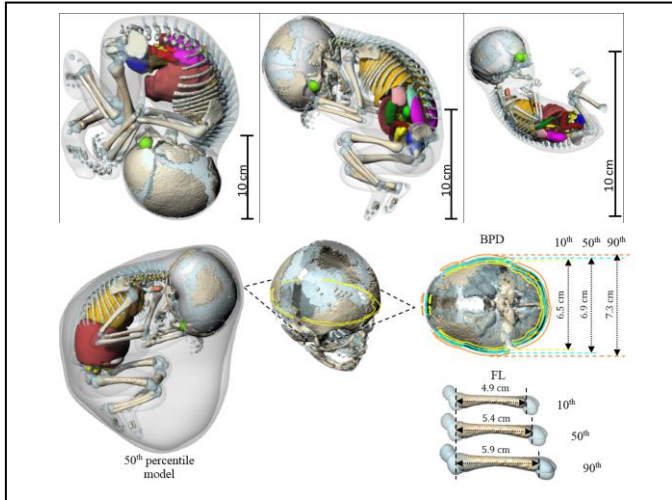


Figure 2. 3D models of the reference fetus at 1<sup>st</sup>, 2<sup>nd</sup>, and 3<sup>rd</sup> trimester of pregnancy (Top). A illustration of differences between 10<sup>th</sup>, 50<sup>th</sup>, and 90<sup>th</sup> percentiles for 6 month fetus (Bottom).

#### IV. CONCLUSION

This phantom series is being constructed based on Iranian reference data. This advantage makes them appropriate to use for producing dose estimates for specific radiation protection purposes in our country. We intend to update photon and electron SAFs for internal emitters as well as organ dose conversion coefficients using our phantoms following the recent ICRP Recommendations.

Another advantage of this series is to be BREP phantoms, the latest generation of phantoms ever created worldwide. However, the children models are non-reference models which may be known as one of the drawbacks of this phantom series. The children models remained patient-specific because the lack of the data from Iranian pediatrics.

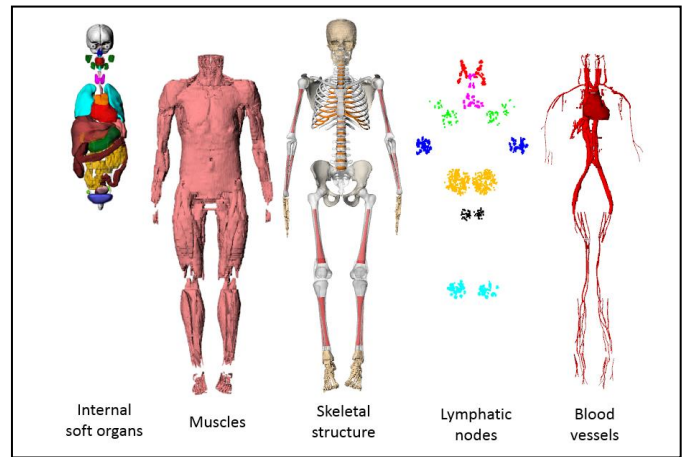


Figure 3. Detailed structure of Iranian adult female reference phantom.

In future, we will improve this series to high quality BREP phantoms by adding details of thin target layers to respiratory and alimentary tract models according to the latest ICRP publications.

Albeit, our secondary objective in developing phantoms for people lives in our country was exploring the way of phantom construction manually, in order to make an automatic process in near future to obtain patient specific models.

#### REFERENCES

- [1] ICRP, "Adult reference computational phantoms, ICRP Publication 110," *Ann ICRP*, vol. 39(2), pp. 61-2, 2009.
- [2] X. G. Xu, and K. F. Eckerman, 2009. "Handbook of anatomical models for radiation dosimetry,," CRC press.
- [3] X. G. Xu, "An exponential growth of computational phantom research in radiation protection, imaging, and radiotherapy: a review of the fifty-year history," *Phys. Med. Biol.* vol. 59(18), pp. R233–R302, 2014.
- [4] E. Hoseinian-Azghadi, H. Miri-Hakimabad, L. Rafat-Motavali, "Population of whole-body statistical adult phantoms and assessing the uncertainty of organ doses in hyperthyroid treatment with <sup>131</sup>I," In 5th International Workshop on Computational Human Phantoms, 2015, pp. 22-23
- [5] E. Hoseinian-Azghadi, L. Rafat-Motavali, H. Miri-Hakimabad, "Development of a 9-month pregnant hybrid phantom and its internal dosimetry for thyroid agents," *J. Radiat. Res.* vol. 55(4), pp. 730-747, 2014.
- [6] L. Rafat-Motavali, H. Miri-Hakimabad, E. Hoseinian-Azghadi, "Fetal and maternal dose assessment for diagnostic scans during pregnancy," *Phys. Med. Biol.* vol. 61(9), pp. 3596-3608, 2016.
- [7] L. Rafat-Motavali, H. Miri-Hakimabad, E. Hoseinian-Azghadi, "Hybrid pregnant reference phantom series based on adult female ICRP reference phantom," *Radiat. Phys. Chem.* vol. 144, pp. 386-395, 2018.
- [8] L. Rafat-Motavali, H. Miri-Hakimabad, E. Hoseinian-Azghadi, "Dosimetric factors for diagnostic nuclear medicine procedures in a non-reference pregnant phantom," *J. Radiol. Prot.* vol. 38(3), pp. 908. 2018.

# Scientific Session

Monday, 22 July 2019

<b>13:30 – 15:00</b>	<b>Scientific Session “Phantom Development II”</b> <b>Chair: Rui Qiu, Co-Chair: Tomoaki Nagaoka</b>
13:30	Keynote Lecture Anthropomorphic breast phantoms in virtual clinical imaging trials Andrew Maidment
14:00	Registering of potential based organ contours to medical images Janine Becker and Mattia Fedrigo
14:20	Mathematical human phantoms for SPECT and PET research Natalya Denisova , Hunor Kertész, Thomas Beyer, Marina Ondar
14:40	NEUROMAN: Realization of neurofunctionalized computational phantoms Bryn Lloyd, Silvia Farcito, Antonino Cassara, Esra Neufeld, Beom Sun Chung, Jin Seo Park, Min Suk Chung, and Niels Kuster

# Keynote Lecture

## Anthropomorphic breast phantoms for use in virtual clinical imaging trials

Andrew Maidment

Department of Radiology, University of Pennsylvania, Philadelphia, USA  
Andrew.Maidment@penmedicine.upenn.edu

**Abstract—** In 2014, it was estimated that there were just 450 anatomic phantoms in the world. Today, based on advanced models of anatomy simulation, an infinite number of models exist. As such, it is possible to simulate individuals and specific pathologies from the population of all humans with increasingly higher accuracy. This, together with advanced models of image simulation, image processing and image reconstruction, means that we can create arbitrarily large databases of simulated images. At the same time, advances in machine observer methods mean that it is possible to conduct virtual clinical trials using these simulated images, together with simulations of medical displays, human optical perception and cognition.

In 2009, we coined the phrase “Virtual Clinical Trials” (or VCT) to describe the intersection of computer simulations of medical imaging and psychophysics experiments with machine observers. The thought was that the two technologies were

sufficiently mature that we could consider simulating entire clinical trials; meaning that both the patient accrual phase and the reader phase were conducted *in silico*. At the time, we conducted a Google search for “Virtual Clinical Trials” and “Imaging” and got less than 10 hits. Today, the same search will lead to over 56,000 results. The advent of advanced computational methods and graphic processor unit (GPU) computing has placed VCTs in the hands of almost every imaging researcher. We routinely conduct trials of 1000 virtual patients comparing digital mammography and digital breast tomosynthesis in approximately 30 hours of GPU time. Today, hundreds of labs conduct VCT in various forms worldwide. In this lecture, the fundamentals of VCTs will be reviewed, and phantom design requirements for VCTs will be explained both at a high-level and through examples.

**Index Terms—***image simulation; machine observer; phantom design requirements*

# Registering of potential based organ contours to medical images.

Janine Becker<sup>1</sup> and Mattia Fedrigo<sup>2</sup>

<sup>1</sup>Helmholtz Zentrum München, Institute of Radiation Medicine, Ingolstädter Landstraße 1, 85764 Neuherberg  
<sup>2</sup>mattia.fedrigo@web.de

**Abstract**—The segmentation of medical images for the extraction of patient anatomy is still a challenge involving also manual interaction despite the amount of different algorithms and their adaptation to individual questions during the last years. Methods for registering already segmented contours to the organ outlines in medical images are preferred because they promise to be less time-consuming. The complex physically based method of potential based contours [1] offers not only a data compressed modelling of organ outlines but also an adjustment to their counterparts inside the medical image (e.g. CT-data) not yet segmented. The first results work in 2D and organs slices of the heart were generated.

## I. INTRODUCTION

Computational human phantoms are becoming more detailed and realistic in terms of anatomy. The benefit of their application in different field of biomedical engineering is out of question. It would be a big step forwards having individual models of individual persons to improve the realistic approach of simulations. Therefore the use of medical data is essential being the only way of gaining information about a persons internal anatomy. Generating a computational phantom from medical images is still a difficult task due to the problem of extracting the correct organ outlines from the image data. To achieve an even better closeness of an already segmented organ to the respective one of an individual patient a registration between organ model and medical image data is often preferred over a de novo segmentation. [2]

### A. Methods

The authors introduced the principle of potential based contours in [1], [3]. Organ contours may be described by a set of source points generating a field in analogy to electrical point charges. Their resulting equipotential lines provides an appropriate model for the contour of a compact organ like heart, stomach and bladder. A constellation of source points, i.e. an organ contour, is inserted in the medical image. Now this organ contour by source points shall be adapted to the organ outlines of the medical image, see fig. 1. The registration is done by following expression.

$$M = \int \frac{|T(\nabla f) \cdot \nabla \varphi|}{|T(\nabla f)| |\nabla \varphi|} \cdot \exp[-\beta(\varphi - \varphi_0)^2] dvol \quad (1a)$$

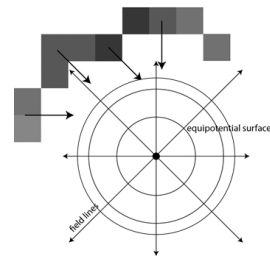


Fig. 1: Potential field and edges of the CT slice

and the optimization criterion

$$M = \operatorname{argmax} \int \frac{|T(\nabla f) \cdot \nabla \varphi|}{|T(\nabla f)| |\nabla \varphi|} \cdot \exp[-\beta(\varphi - \varphi_0)^2] dvol. \quad (1b)$$

The truncated edges  $|T(\nabla f)|$  of the image  $f$  are overlain with the field  $\nabla \varphi$  and the equipotential line  $\varphi_0$ , i.e. the initial organ contour, whereas  $\beta$  serves as a parameter. For a good overlap between initial contour and the edges  $M$  is maximized. Edge detection is performed on medical images by means of gradient methods. The source points are able to be moved within a given area thus the equipotential line is flexible, too. The place of the individual source points towards the image edges shall be optimized to automatically generate a suggestion for an adapted organ contour.

## II. RESULTS

As a first proof of principle the phantom “Laura” [4] (1.875x1.875x5mm voxel resolution) and her original CT data were used. As a first guess, the transversal heart slices M260 of “Laura” was transferred to a constellation of source points providing a potential based organ contour for the organ slice. These source points were transferred in the corresponding CT data and served as initial contour for the neighbouring z-slices 261, 262 and 259, 258, 257. The changes between the neighbouring z-slices are expected to be small, the number of source points  $Q$  should remain unchanged. For each organ slice a contour was provided after the matching criterion Eq. 1b. The algorithm respects the hardly detectable borders between trunk muscle or aorta and heart.

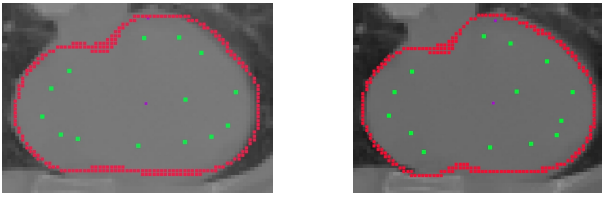


Fig. 2: Q-distribution in T262 (M=219.3, left) and optimized (M=298.97, right)

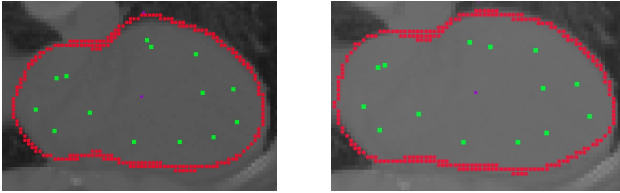


Fig. 3: Q-distribution in T257 (M=252.9, left) and optimized (M=289.5, right)

After the principle proved to be working on medical images the data set of a whole heart was segmented. The principle of potential based organ contours was combined with grayscale windowing. The data set consists of 313 slices, each with  $512 \times 512$  voxels of  $0.35 \times 0.35 \times 0.8 \text{ mm}^3$  resolution.

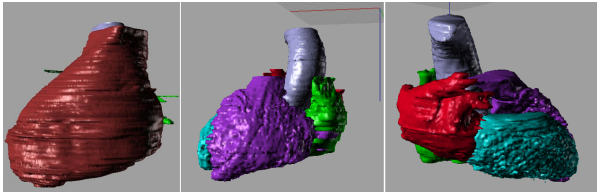


Fig. 4: Computational model of heart with ventricles, vestibules and aorta.

### III. CONCLUSION

A new method for registering organ contours with the edges of CT images was introduced. A constellation of source points provided the initial contour which were replaced in a predefined area to better match the edges after the optimization criterion of formula [1b]. In case there was no better place found, the source point remained at the initial position. Thus a suggestion for the organ contour was provided. After first steps proving the basic principle the algorithm was combined with grayscale windowing to segment the data set of a heart with  $0.35 \times 0.35 \times 0.8 \text{ mm}^3$  voxel resolution. The presented method could be another tool for approaching the difficult task of organ segmentation and registration. It represents a way of organ modelling suitable for the matching of organ contours in medical images being a data compression at the same time. A number of 8-14 source points is sufficient to represent the outline of a heart slice for

both resolutions. It is a continuous data representation. This aspects makes it very interesting to implement this type of modelling into Monte Carlo radiation transport code. In the future effort shall be made to analyse if the potential based contours can be combined with radiation transport code. Furthermore shall be explored if this contour representation is also suitable for other points of interests like cells addressing the idea of a transition from organs down to cell level.

### REFERENCES

- [1] Fedrigo M. Becker, J. Introducing the concept of potential-based organ contours. *IEEE TRPMS*, 3(1).
- [2] W. Kainz, E. Neufeld, W. E. Bolch, C. G. Graff, C. H. Kim, N. Kuster, B. Lloyd, T. Morrison, P. Segars, Y. S. Yeom, M. Zankl, X. G. Xu, and B. M. W. Tsui. Advances in computational human phantoms and their applications in biomedical engineering—a topical review. *IEEE Transactions on Radiation and Plasma Medical Sciences*, 3(1):1–23, Jan 2019.
- [3] J. Becker. Beschreibung von Organgrenzen als Äquipotentialverlauf finiter Quellpunkte mit Q/r-Potentialen. *Dissertation*, Technische Universität Ilmenau, 2015.
- [4] N. Petoussi-Henss, M. Zankl, U. Fill, and D. Regulla. The GSF family of voxel phantoms. *Physics in Medicine and Biology*, 47:89–106, 2002.

# Mathematical human phantoms for SPECT and PET research

Natalya Denisova<sup>1</sup>, Hunor Kertész<sup>2</sup>, Thomas Beyer<sup>2</sup>, Marina Ondar<sup>1,3</sup>

<sup>1</sup> Khristianovich Institute of Theoretical and Applied Mechanics, Novosibirsk, Russia

<sup>2</sup> QIMP Team, Center for Medical Physics and Biomedical Engineering, Medical University of Vienna, Austria

<sup>3</sup> Novosibirsk State Technical University, Novosibirsk, Russia

\*Corresponding author: email address NVDenisova2011@mail.ru

**Abstract**—Simulation studies play an important role in PET and SPECT imaging for studying the causes of image artifacts and uncertainties on clinical situations. For simulation of clinical cases, numerous changes of phantom anatomical parameters are required. Stylized phantoms are most appropriate for calculating a large number of variants because they can be easily and quickly manipulated to change locations, sizes and shapes of organs. However, existing stylized phantoms are too simple. Here, we propose new stylized phantoms with a high level of anatomic realism that were developed for simulations in SPECT and PET.

**Index Terms**—medical imaging; mathematical phantoms;

## I. INTRODUCTION

Solutions of SPECT and PET reconstruction problems (i.e., images quality) depend on the details of a source function (i.e., patient anatomy). As such, small difference in anatomical structures between two patients may result in good image quality for one patient and appearance of artifacts on the second patient image. Clinical methods are limited in studying the problem of images quality because, firstly, it is impossible to carry out the extensive studies with patients and volunteers. And secondly, quantitative assessments of images quality can be obtained only by comparison of reconstructed images with the exact activity distribution. Such studies should be performed with anthropomorphic physical or mathematical phantoms, which can be regarded as reference standard.

Applications of physical manufactured phantoms to study the dependence of reconstructed images quality on patient anatomy are very limited because it would be very expensive to create phantoms with different anatomical structures. Therefore, computational human phantoms are used in SPECT and PET imaging research. There are two approaches to generate the human phantoms with various anatomies: first to develop a large population of phantoms with different body constitutions and different sizes, shapes, positions of organs, and, second, to develop several basic (stylized) phantoms, which could be manipulated to create phantoms with different anatomical structures [1-3]. Both of these approaches can contribute to solving image enhancement problems in SPECT and PET technologies. In simulations of clinical cases, numerous of slight changes of anatomical parameters are often necessary [4]. The stylized phantoms are more appropriate for

such type of studies because they can be easily and quickly manipulated to change the position, size and shape of organs.

## II. METHODS

The phantoms development was performed on the basis of detailed analysis of images presented in Atlas of Human Anatomy [5] and by using clinical CT and MR images. To create the phantoms, the technique of constructive solid geometry (CSG) was applied. A set of suitable figures was used to create models of each organ and each bone. The complex forms were compiled by using Boolean operators. The modelling of each organ is performed through separate procedures and the whole model is assembled in the main program. This allows the user to change shapes and sizes of ‘organs’ easily, and to add lesions of different forms and different locations. Two basic phantoms are created: Mathematical Model of Torso (MMT) and Mathematical Model of a whole Body (MMB).

## III. SIMULATIONS

### A. Mathematical Model of Torso (MMT)

3D anthropomorphic Mathematical Model of Torso (MMT) is intended for simulations of myocardial perfusion SPECT/CT imaging in nuclear cardiology and describes the radiopharmaceutical distribution in thoracic organs. The phantom is shown in Fig.1.

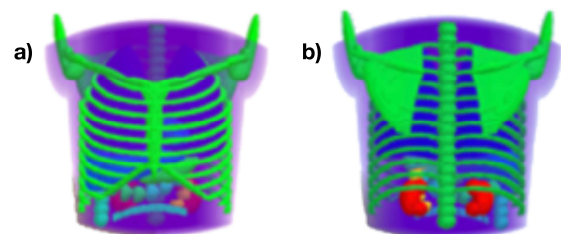


Figure1. Mathematical Model of Torso (MMT) for numerical simulations of myocardial perfusion imaging in nuclear cardiology. Anterior (a) and posterior (b) views of MMT are shown.

MMT simulates a patient position with arms up. MMT is a stylized phantom, which can be easily modified to simulate normal and obese patients with various myocardial left ventricle size and different wall thickness. MMT was applied in our previous paper [4] where more than 1000 numerical experiments were performed to study false apical defect. In computer simulation of SPECT myocardial perfusion imaging, MMT plays the role of a virtual patient and models spatial distribution of  $^{99m}\text{Tc}$ -MIBI. Virtual projection data for the virtual patient were calculated by using home-made codes. As an example, one of 64 simulated projections is shown in Fig.2. Accurate comparison with clinical data was performed for each view. The clinical data were obtained in the Meshalkin National Medical Research Center (Novosibirsk) using GE Infinia Hawkeye SPECT/CT system with LEHR collimator.

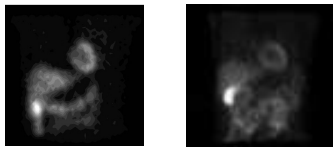


Figure 2. Computer simulation of SPECT/CT myocardial imaging procedure: (left) virtual raw projection data; (right) the corresponding clinical data.

#### B. Mathematical Model of whole Body (MMB)

Mathematical Model of a whole Body (MMB) is developed for simulations of PET imaging in oncology. Anterior, left lateral and posterior views of MMB are shown in Figure 3. In this case, MMB simulates ‘an adult patient with a normal body type’. The model includes the main internal organs, skeletal system and soft tissues.

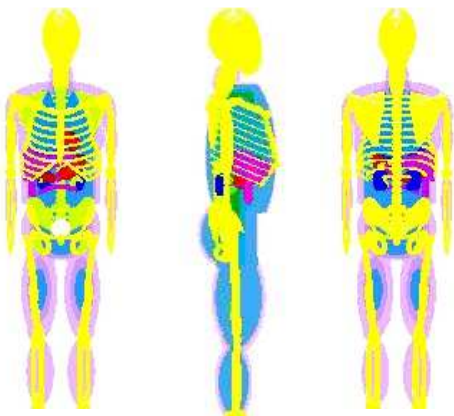


Figure3. Mathematical Model of whole Body (MMB) for numerical simulations of whole body PET scanning in nuclear oncology. Anterior, lateral and posterior views are shown

Modeling of the skeletal system is the most difficult part of the stylized MMB phantom. As noted above, the stylized phantoms allow to vary the size and position of bones. Fig.4 shows an example, in which the MMB skeletal system of an adult patient was transformed into the skeletal system of a teenager.

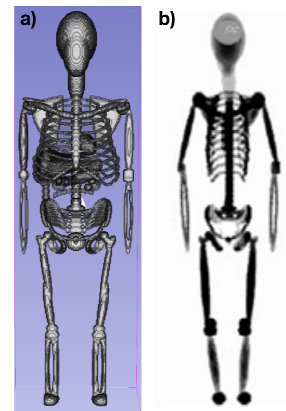


Figure4. An example of MMB skeletal system transformation is presented in these figures. MMB skeletal system of an adult patient (a) was transformed into the skeletal system of a teenager (b).

#### IV. CONCLUSION

With the practical use of PET and SPECT methods, problems arise that are difficult (or impossible) to solve by using only clinical studies. Computer-based simulations with anthropomorphic phantoms that serve as ‘reference standard’ can help studying clinical cases and understanding the causes of artifacts and uncertainties on clinical images.

#### ACKNOWLEDGMENT

This work was supported by Russian Foundation for Basic Research grant № 17-52-14004 and by the Austrian Science Funds 3451-N32.

#### REFERENCES

- [1] Xu X G An exponential growth of computational phantom research in radiation protection, imaging, and radiotherapy: A review of the fifty-year history *Phys. Med. Biol.* **59** R233-R302, 2014.
- [2] Segars W P, Tsui B M W MCAT to XCAT: the evolution of 4D computerized phantoms for imaging research *Proc. IEEE* **97** 1954-68, 2009.
- [3] Bolch W, Lee Ch., Wayson M., Jonson P. Hybrid computational phantoms for medical dose reconstruction *Radiat Envir Biophys* **49** 155-168, 2010.
- [4] Denisova N V, Ansheles A A A study of false apical defects in myocardial perfusion imaging with SPECT/CT *Biomed. Phys. Eng. Express* **4** 065018 2018.
- [5] Sinelnikov RD, Sinelnikov YaR, Sinelnikov AYa Atlas of human anatomy 2007 (in Russian)

# NEUROMAN: Realization of Neurofunctionalized Computational Phantoms

Bryn Lloyd<sup>1,\*</sup>, Silvia Farcito<sup>1</sup>, Antonino Cassara<sup>1</sup>, Esra Neufeld<sup>1</sup>, Beom Sun Chung<sup>3</sup>, Jin Seo Park<sup>4</sup>, Min Suk Chung<sup>3</sup>, and Niels Kuster<sup>1,2</sup>

<sup>1</sup>IT<sup>2</sup>IS Foundation Zurich, Switzerland

<sup>2</sup>Swiss Federal Institute of Technology (ETH) Zurich, Switzerland

<sup>3</sup>Dept. of Anatomy, Ajou Univ., Suwon, Republic of Korea

<sup>4</sup>Dept. of Anatomy, Dongguk Univ., Gyeongju, Republic of Korea

\*Corresponding author: cassara@swiss.ch

**Abstract**— To develop novel therapeutic electrostimulation devices, there is a need to build predictive computational tools, which allow to investigate mechanisms, and optimize treatments. While much progress has been made in recent years, computational electrophysiology still is lacking anatomical models with detailed peripheral nerve connectivity. To this end, we are developing reference human anatomical models with unprecedented details in the peripheral nervous system, connectivity to organs and muscles, and functionalized with compartmental nerve models to investigate interactions with neuronal electrophysiology. The first of models, the Korean female Yoon-Sun V4, was recently released and the male Jeduk V4, will become available shortly.

**Index Terms**—Neurostimulation, MRI, Virtual Population

## I. INTRODUCTION

There is a growing trend towards applying electrical stimulation to the nervous system to control and modify functions of the body. This new category of therapeutic agents, the so called “electroceuticals”, includes numerous types of neurostimulation devices used e.g. to help restore motor function in paraplegics, to treat chronic diseases such as asthma and diabetes, hypertension and other heart conditions, or for the treatment of Parkinson’s disease.

An important step in developing such approach is to employ predictive tools to study nerve electrophysiology within the complex human anatomical environment to

- study the mechanisms of action
- optimize treatments
- ensure the safety of such devices and treatments

We previously developed a modeling approach [1], which we called neuro-functionalization, that represents populations of axons as splines geometrically embedded in the body. Electrophysiological models assigned to the spline trajectories are used to predict the responses of axons and nerves to electromagnetic stimuli. Embedding the nerve models in the anatomy facilitates coupled simulations of the neuro-physiology with induced electrical fields and non-trivial field gradients that result from the complex dielectric material distributions inside

the body. This methodology has been successfully demonstrated in different contexts, e.g., the development of electroceuticals [2], concerning the risk of unwanted neurostimulation by MRI gradient switching [3], and in studies aimed at critical revision of current safety standards [4]. While these investigations are able to predict observed corrections, the lack of realistic anatomical models with detailed nerve trajectories extracted from 3D image data prevents quantitative prediction, e.g. in the context of MRI safety.

To overcome this limitation, within the NEUROMAN project we are developing computational anatomical human (female and male) and animal phantoms with unprecedented details in the peripheral nervous system (PNS) and connectivity to organs and muscles, functionalized with compartmental nerve models. The first human model, a Korean female, was completed and released recently. The male human model will be available shortly.

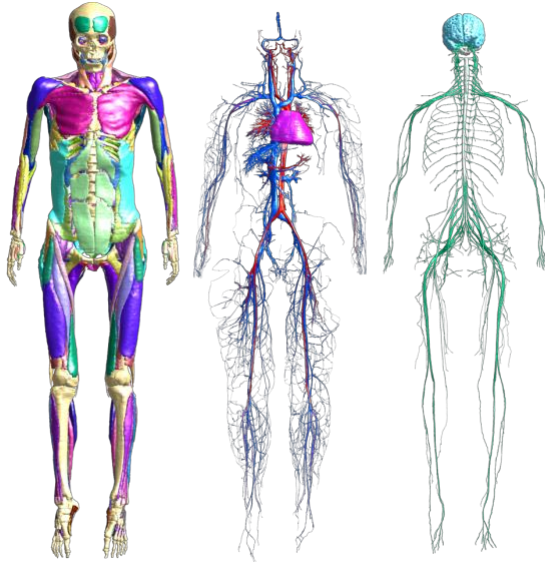
## II. METHODS

The new models were segmented from high resolution cryosection image data, obtained in the Visible Korean Human (VKH) project [5]. While the segmentation data from the VKH was used as a basis, substantial improvements were made to achieve consistent tissue assignments in both the male and female phantoms, as well as compared to Virtual Population (ViP) [6] models following our established ViP QA guidelines. Examples of improvements include: curation of naming and assignment of all tissues, detailed veins and arteries, organ lumens, differentiation between cortical, cancellous and marrow in bones, and structures in the brain and spinal cord, leading to similar quality and details as Virtual Population V3.x models.

The main effort, however, was put into creating an extremely detailed segmentation and neuro-electro-functionalization of the peripheral nervous system. In a first step individual nerves were segmented separately with semi-automatic tools. In a second step, the anatomically correct nerve connectivity was encoded in a rule book (Excel file) and compared to the connectivity extracted programmatically from the segmented label field. Topological and connectivity errors, such as gaps and loops were then identified, visualized and

fixed. In a third step, connected paths following the centerlines of the nerves from the nerve roots to the terminal/endpoints of the connected nerves were extracted automatically based on the rule book. In the fourth and final step, electrophysiological models of myelinated and unmyelinated axons were assigned to nerve (axon) trajectories based on histological investigations documented in the literature.

Figure 2 The female Korean model Yoon-sun V4.0. The figure on the left depicts the muscles (each in a different color) and bones. In the middle, the circulatory system is shown. On the right the brain, spinal cord and peripheral nerves are shown.



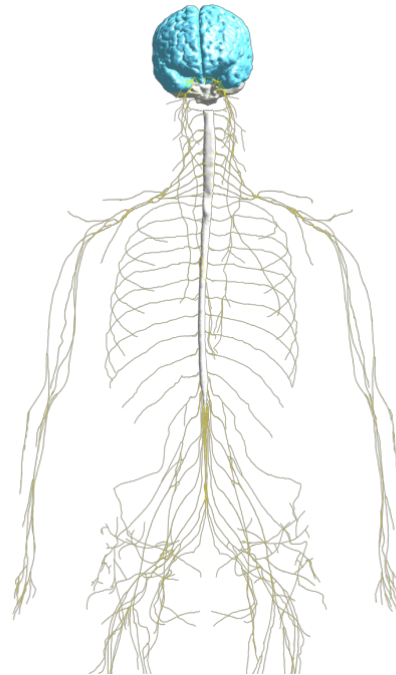
### III. RESULTS AND DISCUSSION

The female model Yoon-sun V4.0 (26y, 1.52m, 55kg) was recently released and will be followed shortly by the male Jeduc V4.0 (33y, 1.64m, 55kg). The models are extremely detailed, with more than 1100 tissues and close to 1000 nerve trajectories. They include the somatic and autonomic nervous systems, with all major peripheral nerves, e.g. vagus nerve and all other cranial nerves. The segmentation also includes the dorsal and ventral roots, and the brachial and sacral plexus. While the focus was on the nervous system, many other tissues are available, enabling a variety of research questions to be investigated, e.g. the importance of the small vasculature on RF induced heating. To validate this model for specific contexts of use, our first target is MRI safety. Other applications are being identified within the scope of the NIH funded SPARC program, which is trying to understand how nerve stimulation controls organ functionality, where these models will become an integration center for multi-scale organ and tissue models.

### IV. CONCLUSION

The NEUROMAN models represent unique tools for the scientific community, which enable multi-scale modelling studies with realistic anatomies and electrophysiology. The results obtained with these models will provide test-beds for new therapeutic approaches and devices, helping to increase treatment specificity with reduced risk of side effects, perform safety studies or performing regulatory submissions and standardization activities.

Figure 1 The trajectories are modeled as splines, which follow the centerline from the nerve roots to the terminal points of the connected nerve(s). Due to the voxel resolution false connections are possible, and are filtered out based on a set of encoded rules.



### ACKNOWLEDGMENT

This research has received funding and support by Innosuisse (CTI 25290.1 PFLS-LS), the Korean Institute for Advancement of Technology, and Common Fund's Stimulating Peripheral Activity to Relieve Conditions (SPARC) of the National Institutes of Health under the transaction award number 1OT3OD025348-01.

### REFERENCES

- [1] E. Neufeld, A. Cassara, H. Montanaro, N. Kuster, and W. Kainz, "Functionalized anatomical models for EM-neuron interaction modeling," *Phys. Med. Biol.*, Feb. 2016.
- [2] A. Cassara, E. Neufeld, and N. Kuster, "Vagus Nerve Stimulation: Comparison of Thresholds for A-, B- and C-Fiber Recruitment for Cuff Electrodes and Alternative Stimulation Configurations in Functionalized Generic and Anatomical Models," in *Proceeding of COST-EMF-MED workshop on 'Vagus Nerve Stimulation'*, Warsaw (PL), 2017.
- [3] A. Cassara, E. Neufeld, and N. Kuster, "Peripheral Nerve Stimulation in MRI: Insight from a three level analysis and coupled EM-electrophysiological simulations in neuro-functionalized human models," in *Proceedings of the 25th International Society of Magnetic Resonance in Medicine (ISMRM) Conference*, Honolulu (Hawaii, USA), 2017.
- [4] E. Neufeld, I. Vogiatzis, M. Iacono, L. Angelone, W. Kainz, and N. Kuster, "Investigation of assumptions underlying current safety guidelines on EM-induced nerve stimulation," *Phys. Med. Biol.*, Feb. 2016.
- [5] J. S. Park, M. S. Chung, S. B. Hwang, Y. S. Lee, D.-H. Har, and H. S. Park, "Visible Korean human: improved serially sectioned images of the entire body," *Med. Imaging IEEE Trans. On*, vol. 24, no. 3, pp. 352–360, 2005.
- [6] M.-C. Gosselin *et al.*, "Development of a new generation of high-resolution anatomical models for medical device evaluation: the Virtual Population 3.0," *Phys. Med. Biol.*, vol. 59, no. 18, p. 5287, 2014.

# Scientific Session

Monday, 22 July 2019

<b>15:30 – 16:50</b>	<b>Scientific Session “Biomedical Imaging”</b> <b>Chair: Niels Kuster, Co-Chair: Andrew Maidment</b>
15:30	A 4D CT/MRI digital phantom and its application in carbon-ion therapy of abdominal lesions Paganelli C, Meschini G, Vai A, Muller M, Keall P, Riboldi M, and Baroni G
15:50	MRI radio-frequency heating: effect of small vasculature Manuel Murbach, Bryn Lloyd, Silvia Farcito, Esra Neufeld, and Niels Kuster
16:10	Neurostimulation safety investigations using neurofunctionalized anatomical models Antonino Cassara, Bryn Lloyd, Esra Neufeld, Silvia Farcito, and Niels Kuster
16:30	Creation of a population of patient phantoms for deep learning-based denoising of SPECT brain imaging Clifford Lindsay, Benjamin Auer, Yongi Yang, Lars R. Furenlid, and Michael A. King

# A 4D CT/MRI digital phantom and its application in carbon-ion therapy of abdominal lesions

Paganelli C<sup>1,\*</sup>, Meschini G<sup>1</sup>, Vai A<sup>2</sup>, Muller M<sup>3</sup>, Keall P<sup>3</sup>, Riboldi M<sup>4</sup> and Baroni G<sup>1,2</sup>

<sup>1</sup>Dipartimento di Elettronica, Informazione e Bioingegneria, Politecnico di Milano, Milano, Italy

<sup>2</sup>Centro Nazionale di Adroterapia Oncologica, Pavia, Italy

<sup>3</sup>ACRF Image X Institute, Sydney Medical School, University of Sydney, Sydney, Australia

<sup>4</sup>Department of Medical Physics, Ludwig-Maximilian-Universität München, Munich, Germany

\*Corresponding author: chiara.paganelli@polimi.it

**Abstract**—We propose the use of a 4DCT/MRI anthropomorphic digital phantom (named CoMBAT) to evaluate the derivation of a virtual 4DCT from 4DMRI data in carbon ions treatment of abdominal tumors.

**Index Terms**—4DCT/MRI anthropomorphic digital phantom, radiotherapy, organ motion, particle therapy

## I. INTRODUCTION

External beam radiotherapy represents a cancer treatment technique which aims to deliver the maximum radiation dose to the target while sparing healthy organs. It is well-known that motion of both tumor and nearby organs at risk introduces geometric uncertainties, leading to potential geographical miss of the target and overdosage to surrounding organs [1]. This has even more impact in case of advanced treatments such as particle therapy, where the higher geometrical selectivity and radiobiological effectiveness with respect to conventional X-ray radiotherapy require additional care to plan and deliver the treatment accurately [2]. Time-resolved 4D Computed Tomography (4DCT) represents the imaging clinical standard in the presence of organ motion, however an increasing interest has been put on the use of novel radiation-free, well-contrasted 4D Magnetic Resonance Imaging (MRI) techniques to complement or replace 4DCT [3]. Different studies enhanced the potential of 4DMRI, however multi-modal physical or digital phantoms are required to provide a proper validation, due to the lack of a ground truth when patient data is used. However, the well-known limitation of the most of physical phantoms is related to the lack of an anthropomorphic description.

In this work we therefore exploit the use of an anthropomorphic 4D CT/MRI digital phantom that we implemented in a previous study [4] to validate a virtual 4DCT derived from 4DMRI data [5] in carbon ion treatment of abdominal tumors.

## II. DATASET

For the derivation of the 4D CT/MRI Breathing Anthropomorphic Thorax (CoMBAT) phantom [4], a 4D CT XCAT [6] phantom of the abdomen was generated with 4 respiratory bins (30%-exhale, end-exhale, 30%-inhale, end-inhale) and a maximum motion of 7mm in the superior-inferior (SI) direction (matrix: 522×522×125 voxels with

0.98×0.98×0.98mm spacing). This 4DCT served as ground truth for 4DMRI simulation and phantom clinical application.

For MRI simulation, we referred to T2/T1-weighted balanced steady-state free precession sequence (i.e. TrueFISP) typically used in MRI-guidance for respiratory motion quantification and 4DMRI reconstruction (TR/TE: 228.07ms/1.5ms;  $\alpha$ : 33°; scan matrix: 256×256 pixels with spacing of 1.33×1.33 mm; slice thickness of 5 mm; acquisition time: 310ms/slice with 25 slices × 30 frames. K-space percentage sampling: 65%; acceleration factor: 2 with a generalized auto-calibrating partially parallel acquisition (GRAPPA) using 16 auto-calibration (AC) lines). To derive specific MR tissue parameters, dedicated MRI sequences (i.e. DESPOT1 and DESPOT2 at different flip angles) were acquired with a 1.5-T MR scanner on healthy volunteers [5].

## III. COMBAT SIMULATION

The CoMBAT phantom [4] was described in k-space through a combination of several weighting functions and transformations:

$$P(k, t) = R \cdot F \cdot [S(N_{coil}) \cdot T(T1, T2, \rho) \cdot C(TE, TR, \alpha) \cdot O(x, t) + n(x, t)]$$

where  $O(x, t)$  represents the 4D XCAT phantom defined in space and time and  $n(x, t)$  is the noise model, simulated by adding a Gaussian noise (SNR set equal to 20).  $T$  is the tissue contribution as a function of relaxation times  $T1$  and  $T2$  and proton density  $\rho$ , derived from DESPOT1 and DESPOT2 in vivo acquisitions. The MR sequence is described by the operator  $C$ , which expresses the acquired signal as a function of  $TR$ ,  $TE$  and  $\alpha$  of the TrueFISP sequence.  $S$  describes the sensitivity of  $N_{coil}$  coils. The sensitivity coil maps were simulated as a linear fall-off from the individual coils that were placed uniformly on a circle around the abdomen ( $N_{coils}=8$ ). These physical space functions undergo Fourier transformation  $F$ , and the sampling of k-space  $R$  is applied to produce the raw k-space phantom  $P(k, t)$ . Specifically, for k-space sampling, 65% of the k-space was sampled based on the GRAPPA scheme. In the GRAPPA algorithm, k-space was undersampled in the phase encoding direction (i.e., sampling factor=2, acquisition of interleaved lines) and the missing k-space lines were synthesized by a linear combination of acquired neighboring k-space data using spatial information

contained in the coil elements. The acquisition of additional lines in the k-space center was used as a form of self-calibration (i.e., AC=16). Once all k-space samples were obtained for a specific coil, an inverse Fourier transform was used to generate the uncombined image for that coil. The full set of  $N_{\text{coils}}$  images was then combined using a conventional sum of squares reconstruction. Figure 1 reports a comparison between the MRI and CT phantom.

#### IV. COMBAT APPLICATION: THE VIRTUAL 4DCT

The application validated with the CoMBAT phantom consists in the generation of a simulated virtual 4DCT from 4DMRI data [4] to be used in carbon ion treatment of the abdominal site. Specifically, the virtual 4DCT was generated as follows: deformable image registration was used to register each respiratory phase of the 4DMRI to a reference respiratory phase (i.e. end-exhale); the end-exhale CT was registered to this reference MR volume; finally, the virtual 4DCT was obtained by warping the registered CT according to previously obtained deformation fields.

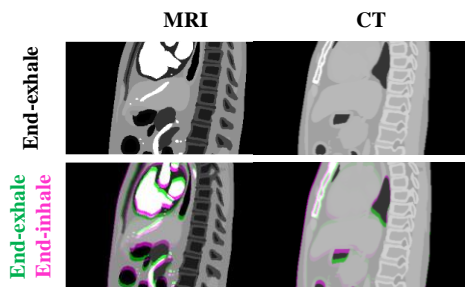
##### A. Treatment planning and analysis

A plan with a single beam passing through the abdomen was optimized on the reference end-exhale CT (planCT) and recalculated on the virtual CTs (vCT) and on the ground truth CTs (GT) with the RayStation treatment planning system. The recalculated doses were compared in terms of: gamma pass rate and DVHs. The dose to the 5% and 95% of the tumor volume (D5% and D95%) and tumor volume with dose  $\geq 95\%$  of the prescription dose (V95%). Additionally, the tumor center of mass displacements between the planCT and the GT, and between vCT and GT were computed to quantify organ motion and the virtual CT geometrical error, respectively.

##### B. Results and Discussion

In Figure 2, dose alteration due to motion of the bowel (highlighted in yellow) within the beam path is visible. For all the respiratory phases, the gamma pass rate was  $> 98\%$ . In Table 1, the percentage variation of the tumor D5%, D95% and V95% are listed, highlighting variations  $< 2\%$ , attesting the validity of the simulated CT. The tumor maximum displacement in the GT with respect to the planCT was 5.77mm at end-inhale. An error up to 2.85mm was found for the 30%-exhale vCT, which remains below the MR resolution ( $1.33 \times 1.33 \times 5\text{mm}$ ) and it is likely due to the interpolation occurring during automatic contour warping.

Figure 1. CoMBAT phantom. MRI and CT corresponding sagittal slices, with overlap at two extreme respiratory phases.



#### V. CONCLUSION

The 4DCT/MRI phantom we implemented represents a viable tool for validation. To date, it is undergoing further developments including the simulation of additional MR sequences and a model of MR geometrical distortions and inhomogeneities. It is currently used as a validation tool in several MRI-guided strategies for radiotherapy. Here, we showed its potential in evaluating a virtual 4DCT derived from 4DMRI data for carbon ion therapy of the abdominal site, providing ground truth information which would not be available when using patient data.

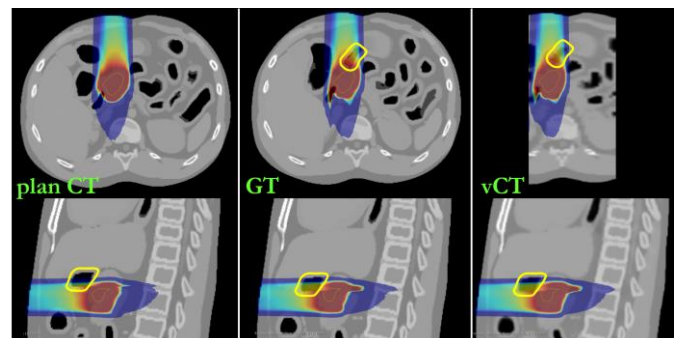
#### REFERENCES

- [1] P. Keall, G.S. Mageras, et al. "The management of respiratory motion in radiation oncology report of AAPM Task Group 76" *Med. Phys.* 33, 3874-900, 2006.
- [2] M. Riboldi, R. Orecchia and G. Baroni, "Real-time tumour tracking in particle therapy: technological developments and future perspectives" *Lancet Oncol.*, 13, 383-91, 2012.
- [3] C. Paganelli, B. Whelan, M. Peroni, et al. "MRI-guidance for motion management in external beam radiotherapy: current status and future challenges", *Phys. Med. Biol.*, 63, 22TR03, 2018.
- [4] D. Boye, T. Lomax and A. Knopf. "Mapping motion from 4D-MRI to 3D-CT for use in 4D dose calculations: a technical feasibility study" *Med. Phys.*, 40, 061702, 2013.
- [5] C. Paganelli, P. Summers, C. Gianoli, et al. "A tool for validating MRI-guided strategies: a digital breathing CT/MRI phantom of the abdominal site", *Med Biol Eng Comput*, 55, 2001-2014, 2017.
- [6] P. Segars, G. Sturgeon, S. Mendonca, et al. "4D XCAT phantom for multimodality imaging research", *Med Phys* 37, 4902-4915, 2010.

TABLE I. DOSIMETRIC AND GEOMETRIC DIFFERENCES BETWEEN THE ESTIMATED VIRTUAL CT (vCT) AND THE GROUND TRUTH (GT).

Phase	Dose metrics			Displacement [mm]	
	$\Delta D5\%$	$\Delta D95\%$	$\Delta V95\%$	planCT vs. GT	vCT vs. GT
30%-exhale	0.9%	0.0%	0.0%	0.69	2.85
End-exhale	0.0%	0.0%	0.0%	0.10	0.95
30%-inhale	1.7%	0.0%	0.0%	2.14	0.26
End-inhale	0.4%	0.0%	0.1%	5.77	0.91

Figure 2. Planned dose distribution on the (end-exhale) planCT, recalculated dose on the end-inhale GT and end-inhale vCT.



# MRI Radio-Frequency Heating: Effect of Small Vasculature

Manual Murbach<sup>1</sup>, Bryn Lloyd<sup>1,\*</sup>, Silvia Farcito<sup>1</sup>, Esra Neufeld<sup>1</sup>, and Niels Kuster<sup>1,2</sup>

<sup>1</sup>IT'IS Foundation Zurich, Switzerland

<sup>2</sup>Swiss Federal Institute of Technology (ETH) Zurich, Switzerland

\*Corresponding author: lloyd@swiss.ch

**Abstract**— The numerical assessment of the radiofrequency (RF)-induced local temperature increase inside a patient undergoing magnetic resonance imaging (MRI) diagnostics is state-of-the-art in MRI safety studies. In light of the continuous improvement in the resolution of anatomical models, we investigated the impact of the level of detail in the vasculature models on estimates of temperature increase. Results show that the difference of the peak temperature increase for the investigated high-exposure scenario is in the order of 20%. Future investigations should broaden the studied exposure scenarios and consider vascular convection.

**Index Terms**—MRI Safety; RF Heating; Virtual Population; Yoon-sun

## I. INTRODUCTION

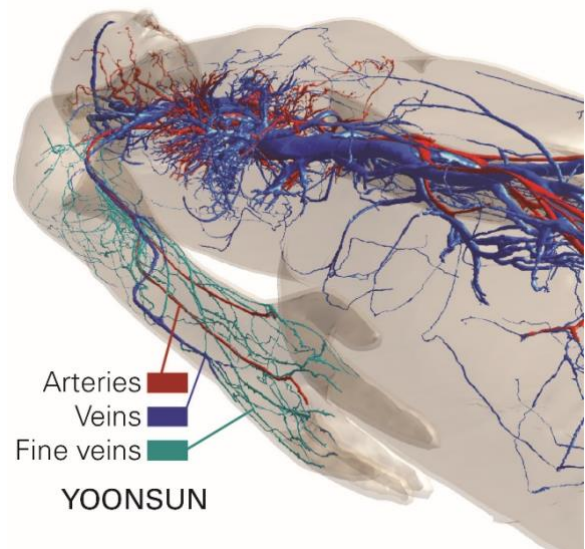
Magnetic resonance imaging (MRI) radiofrequency (RF) safety with regard to associated induced tissue heating can be studied by means of simulations involving computational anatomical models. These thermal simulations are becoming more and more important in academia and regulatory safety assessment sectors, yet they require a large data set of thermal and physiological parameters, including the tissues' thermal conductivity and blood perfusion. A further requirement is that the anatomical human model studied is sufficiently detailed. The latest generation of the Virtual Population (ViP) [1] includes YOONSUN V3.1, a female model with unprecedented detail in nerve and vasculature anatomy. While the impact of microvasculature is typically handled through a homogeneous and distributed heat-sink term, the thermal impact of large vessels is typically simulated by imposing a Dirichlet boundary condition [2] (37°C) – corresponding to the assumption that such vessels effectively cool their surfaces. We investigated the influence of the level of detail in the vasculature model with regard to its effect on RF-induced temperature increase estimations, by comparing simulations with the newly available extremely detailed YOONSUN vasculature to simulations where the YOONSUN vessels with diameters <2 mm are not treated as boundary conditions. This provides insight into the influence of the vessel tree detail on thermal modelling as well as likely allows estimation of an upper bound on the impact of medium-sized vasculature.

## II. METHODS

ViP model YOONSUN was investigated in the abdominal MRI imaging position, which constitutes a high exposure scenario [3] with a thermal hotspot in the right forearm. The

Pennes bioheat equation [4] has been applied with thermo-physical and physiological parameters from the literature [5]. The medium-sized vessels with diameters <2 mm in the comparison-simulation were cut off and assigned the properties of fat tissue.

Figure 1 Vessel system of the right forearm of ViP model YOONSUN, showing the large vessels with veins in blue and arteries in red and the newly available medium-sized vasculature shown in turquoise. In other images, all veins are shown in blue.



The vessel system with the division into large and small vessels is illustrated in Figure 1. The exposure level was normalized to the first level controlled operating mode with a whole-body averaged specific absorption rate (wbSAR) of 4 W/kg. Thermo-regulated perfusion values were not considered for this study, which explains the high steady-state peak temperature of >45°C.

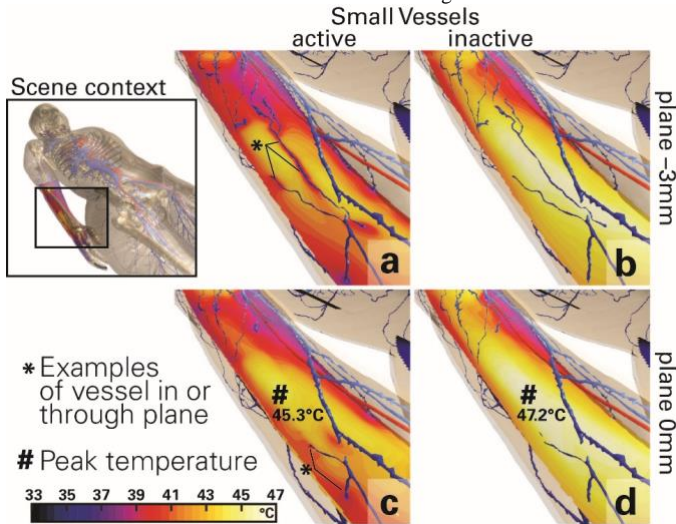
## III. RESULTS AND DISCUSSION

The steady-state temperature distributions for the detailed vessel system and the situation with only large-sized vessels considered are shown in Figure 2. Two slice-views at a vertical distance of 3 mm are provided: panels (a,b) show the situation with a high degree of vasculature detail and panels (c, d) show the location of the actual thermal hotspot. While the simulated medium-sized vessels considerably alter the temperature distribution around their location, the actual peak temperature increase in the thermal hotspot is affected less – a reduction from

47.2°C to 45.2°C, 20% of the temperature increase – when the medium-sized vessels are modeled as boundary conditions. The hotspot location was identical for both simulations (Figure 3).

The real impact of medium-sized vasculature is likely to be between the two simulated scenarios, as medium-sized vessels do not act as perfect coolers – due to Dirichlet boundary conditions – but rather as convective boundary conditions. Also, the heating of the blood in such vessels can no longer be neglected. The situation is further complicated by the active transport of heated blood, which results in less effective cooling or even heating at remote locations.

Figure 3 Local steady-state temperature distributions after >50 min heating in two different horizontal planes. When the medium-sized vessels are modeled as Dirichlet boundary conditions (a,c), the temperature is reduced in the tissues surrounding these vessels (\*); the images in (b,d) show the situation when no boundary conditions are applied for medium-sized vessels. The thermal peak (#) is at the same location in both scenarios. The veins in all images are shown in 3D.

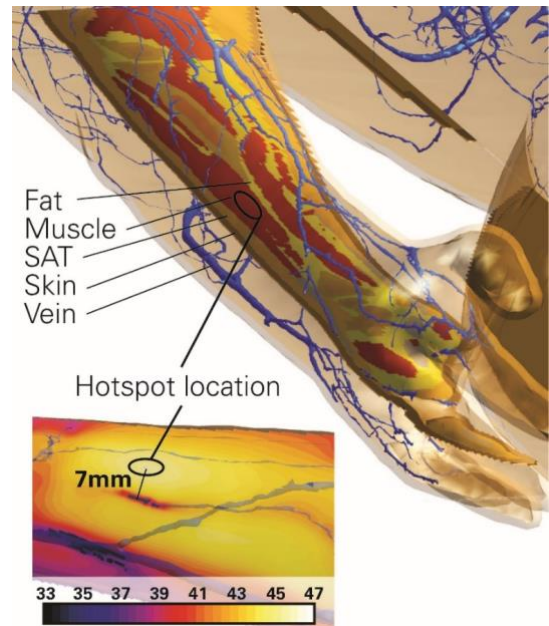


While a peak temperature increase uncertainty of 20% associated with the modeling of medium-sized vasculature might be smaller than the uncertainty associated with the tissue perfusion parameters and the impact of thermoregulation (on the order of 30% [2]), it should be noted that the uncertainty in the temperature increase elsewhere – potentially in thermally sensitive tissues – can be much larger, and that only a single, illustrative MRI exposure scenario has currently been studied.

#### IV. CONCLUSION

Future investigations of more exposure scenarios and more realistic modeling of the impact of the thermal vasculature (e.g., based on the DIVA model [6] that couples 1D convective vascular tree thermal simulations with 3D thermal modelling) must be performed.

Figure 2 Voxeled slice at the position of the thermal hotspot: the large forearm muscle with the nearest medium-sized vein is located approximately 7 mm below the plane (not visible). The temperature distribution around the hotspot and the closest vessel is shown in the lower image, which reveals a slice nearly vertical to the nearest vein below the hotspot. The in-plane vessel, with the assignment of a 37°C Dirichlet boundary condition, appears black.



#### ACKNOWLEDGMENT

This project is supported by funding from the MRInext and NEUROMAN projects.

#### REFERENCES

- [1] M.-C. Gosselin *et al.*, “Development of a new generation of high-resolution anatomical models for medical device evaluation: the Virtual Population 3.0.,” *Phys Med Biol*, vol. 59, no. 18, pp. 5287–5303, Aug. 2014.
- [2] M. Murbach *et al.*, “Thermal tissue damage model analyzed for different hole-body SAR and scan durations for standard MR body coils,” *Magn Reson Med*, vol. 71, no. 1, pp. 421–431, Feb. 2014.
- [3] M. Murbach *et al.*, “Virtual population-based assessment of the impact of 3 Tesla radiofrequency shimming and thermoregulation on safety and B1+ uniformity,” *Magn. Reson. Med.*, vol. 76, pp. 986–997, 2016.
- [4] H. H. Pennes, “Analysis of tissue and arterial blood temperatures in the resting human forearm,” *Appl. Physiol.*, vol. 1, no. 2, pp. 93–122, 1948.
- [5] P. A. Hasgall *et al.*, “IT’IS database for thermal and electromagnetic parameters of biological tissues. Version 4.0, May 15, 2018,” [www.itis.ethz.ch/database](http://www.itis.ethz.ch/database), 2018.
- [6] J. Lagendijk, A. Kotte, and B. Raaymakers, “Discrete Vasculature (DIVA) Model Simulating the Thermal Impact of Individual Blood Vessels for In Vivo Heat Transfer,” *Adv. Numer. Heat Transf. Vol. 3 Ser. Comput. Phys. Process. Mech. Therm. Sci. ISBN 978-1-4200-9521-0 CRC Press Ed. W Minkowycz E Sparrow J Abraham Pp 121-147*, vol. 3, pp. 121–147, Mar. 2009.

# Neurostimulation Safety Investigations using Neurofunctionalized Anatomical Models

Antonino Cassara<sup>1,\*</sup>, Bryn Lloyd<sup>1</sup>, Esra Neufeld<sup>1</sup>, Silvia Farcito<sup>1</sup>, and Niels Kuster<sup>1,2</sup>

<sup>1</sup>IT'IS Foundation Zurich, Switzerland

<sup>2</sup>Swiss Federal Institute of Technology (ETH) Zurich, Switzerland

\*Corresponding author: cassara@swiss.ch

**Abstract**— Investigations about the risk of Peripheral Nerve Stimulation (PNS) in magnetic resonance imaging (MRI) are fundamental to mitigate potential safety issues related to the new generation of MRI scanners that use larger Larmor fields and faster/higher gradients. In this study we evaluate the potential of in silico studies for determining the thresholds of PNS when taking into account the anatomical detail and electrophysiology of the peripheral nervous system. We used the latest hybrid electromagnetic (EM) and neuronal simulators combined with our recently released neuro-functionalized Virtual Population model Yoon-sun V4.0. The vision is to utilize such systems for pulse sequence optimization to reduce PNS, and to support the revision of low frequency exposure guidelines.

**Index Terms**—Neurostimulation, MRI, Virtual Population

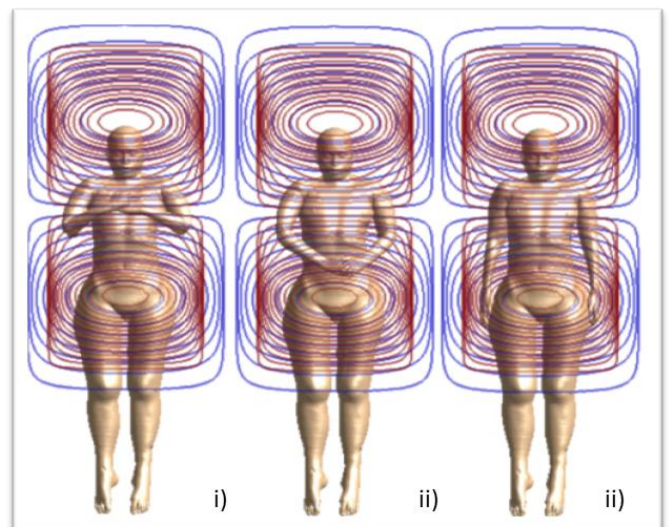
## I. INTRODUCTION

Current advances in MRI-based techniques to reduce imaging time and increase contrast, require higher Larmor field intensities (7 – 10T) and faster gradient switching and higher gradient intensities. Important projects, such as the Human Brain Connectome [1], critically depend on such developments. These novel imaging techniques may pose safety issues related to the enhanced risk of radio frequency (RF) tissue heating and unwanted peripheral (or cardiac) stimulation. In 2016, our group pioneered research [2] on the use of hybrid computational neuro-electrophysiology and electromagnetics to quantify gradient-induced contexts stimulation performing coupled EM and neuronal simulations centered on different computational human body models inclusive of realistic nerve trajectories. While that study provided results in qualitative and quantitative agreements with experiments about specificity of thresholds to pulse sequences, gradient units, human BMI and position as well as sites of spike initiation, shortcomings of the models (nerves were modeled according to anatomy textbooks, not from patient/anatomy-specific segmentations) limited the significance of our predictions. Here we present results obtained with the first neuro-functionalized Virtual Population (ViP) model [3], [4], “Yoon-sun V4.0”. The current work extends our work initiated in 2016 and provides additional insights into both the effects of typical body postures in MRI (e.g., position of hands and arms) and the identification of fiber type (i.e., sensory or motor fibers) specific stimulation thresholds.

## II. METHODS

The neuro-functionalized phantom Yoon-sun V4.0 was created on the basis of high-resolution cryosection images from the Visible Korean Human project [5] (Figure 1). All major peripheral nerves were segmented and spline nerve trajectories were automatically created by computing the centerlines from the surface models of the nerves. Three typical body postures were considered (Figure 2) with respect to arm positions as well as three different landmark positions of the whole body within the MRI scanner (head-, heart-, and pelvis-centered). The modelling pipeline was implemented in Sim4Life (ZMT Zurich MedTech AG, Switzerland). Nerve trajectories were assigned to electrophysiological models of myelinated sensory and motor axons (e.g., MRG [6]). EM simulations were executed using the Magneto-Quasistatic solver. Neurostimulation was investigated considering 3D EPI/ 3D Spiral waveforms typically used for brain imaging. Furthermore, the effect of gradient waveforms by individual and combined gradient units were included. Stimulation thresholds and site of spike initiation were identified for each nerve trajectory. Results are compared with experimental values and recently published computational work [7].

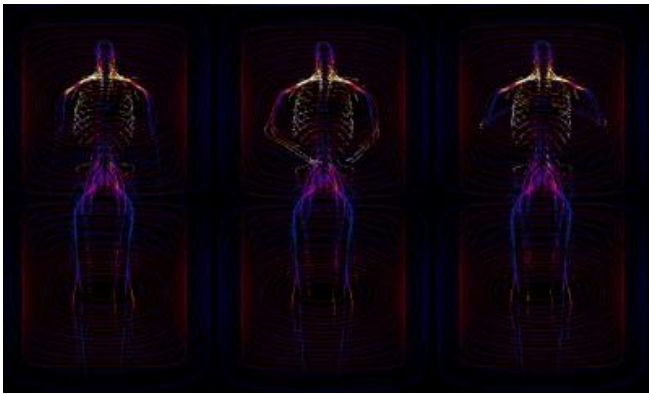
Figure 1 Example of different realistic postures for arms and hands for a subject within the scanner. For investigations about PNS, in the first two posture arms are touching each other.



### III. RESULTS AND DISCUSSION

The developed workflow allows to analyses all the different permutations of coil units, postures and landmark positions with respect to the MRI scanner. Figure 3 illustrates an example of E-field exposure extracted at the nerve entities for the x-gradient coil unit. Positions of the hands and arms affect the local E-field exposure on nerves, especially in the region of the arms and hands and around the brachial plexus, where typically neurostimulation is experienced in experiments. Regions of large E-field variations are also observed in the different postures that can be related to potential sites of neurostimulation. Precise identification of sites of spike initiation and quantification of stimulation thresholds will be provided by the hybrid EM-neuronal simulations currently in execution.

Figure 2 E-field interpolated at the surface of the nerve entities.



### IV. CONCLUSION

The newly developed Yoon-sun V4.0 model permits quantitative predictions of the risk of PNS in MRI environments and arbitrary postures. After confirming the predictive power of hybrid EM-electrophysiological simulations with more experimental data, we foresee applications in 1) scanning guidelines (posture, position) to reduce unwanted stimulation, 2) pulse sequence optimization that can also include stimulation

reduction as goal or constraint (in addition to image quality, scan time, etc.), and 3) should further results confirm mechanistic observations akin to those from [8], the low frequency exposure guidelines (e.g. ICNIRP, etc.) will require revision. The proposed modeling could be a valuable tool for that purpose.

### ACKNOWLEDGMENT

This project supported by the Swiss-Korean project NEUROMAN (CTI 25290.1 PFLS-LS).

### REFERENCES

- [1] A. Nowogrodzki, "The world's strongest MRI machines are pushing human imaging to new limits," *Nature*, vol. 563, no. 7729, pp. 24–26, Nov. 2018.
- [2] A. Cassara, E. Neufeld, and N. Kuster, "Peripheral Nerve Stimulation in MRI: Insight from a three level analysis and coupled EM-electrophysiological simulations in neuro-functionalized human models," in *Proceedings of the 25th International Society of Magnetic Resonance in Medicine (ISMRM) Conference*, Honolulu (Hawaii, USA), 2017.
- [3] A. Christ *et al.*, "The Virtual Family—development of surface-based anatomical models of two adults and two children for dosimetric simulations," *Phys. Med. Biol.*, vol. 55, no. 2, p. N23, 2009.
- [4] M.-C. Gosselin *et al.*, "Development of a new generation of high-resolution anatomical models for medical device evaluation: the Virtual Population 3.0," *Phys. Med. Biol.*, vol. 59, no. 18, p. 5287, 2014.
- [5] J. S. Park, M. S. Chung, S. B. Hwang, Y. S. Lee, D.-H. Har, and H. S. Park, "Visible Korean human: improved serially sectioned images of the entire body," *Med. Imaging IEEE Trans. On*, vol. 24, no. 3, pp. 352–360, 2005.
- [6] J. L. Gaines, K. E. Finn, J. P. Slopesema, L. A. Heyboer, and K. H. Polasek, "A model of motor and sensory axon activation in the median nerve using surface electrical stimulation," *J. Comput. Neurosci.*, vol. 45, no. 1, pp. 29–43, Aug. 2018.
- [7] "Predicting Magnetostimulation Thresholds in the Peripheral Nervous System using Realistic Body Models | Scientific Reports." [Online]. Available: <https://www.nature.com/articles/s41598-017-05493-9>. [Accessed: 08-Mar-2019].
- [8] E. Neufeld, A. Cassara, H. Montanaro, N. Kuster, and W. Kainz, "Functionalized anatomical models for EM-neuron interaction modeling," *Phys. Med. Biol.*, Feb. 2016.

# Creation of a Population of Patient Phantoms for Deep Learning-based Denoising of SPECT Brain Imaging

Clifford Lindsay<sup>1,\*</sup>, Benjamin Auer<sup>1</sup>, Yongi Yang<sup>2</sup>, Lars R. Furenlid<sup>3</sup>, and Michael A. King<sup>1</sup>

<sup>1</sup>University of Massachusetts Medical School Worcester, MA USA

<sup>2</sup>Illinois Institute of Technology Chicago, IL USA

<sup>3</sup>University of Arizona Tucson, AZ USA

\*Corresponding author: clifford.lindsay@umassmed.edu

**Abstract**—Using traditional digital phantoms based on the anatomical features of a small number of humans for training deep learning methods is generally not sufficient for most tasks. For these deep learning methods to perform well on clinical data, they must be trained with a significant number of images that exhibit feature variations similar to a clinical population, which can be difficult to produce with traditional digital phantoms, such as the XCAT phantom. We show that overcoming this limitation can be achieved by utilizing datasets from different domains and then adapting them to our purpose using opensource tools. Our target application is creating digital phantoms for SPECT GATE brain simulations, but these methods are applicable to many other fields.

**Index Terms**—Digital Phantoms; Brain Phantoms; Deep Learning; Image Domain Adaptation;

## I. INTRODUCTION

In the past, we have used the XCAT digital anthropomorphic phantom<sup>1</sup> to create the source and attenuation distributions from which we produce Monte Carlo simulated images approximating those that would be acquired clinically by our in construction dedicated brain SPECT called AdaptiSPECT-C. The source and attenuation distributions of the XCAT can be altered to match variations in physical size of patients<sup>2</sup>. The relative concentration of the activity in the different structures of the brain can also be altered. However, the shapes and spatial relationships of the brain structures in the XCAT are based on a single human, and therefore provide low variability in this respect.

For many machine learning (ML) methods, training data variability or the number of distinct examples in a dataset is a key component which contributes to their accuracy<sup>3</sup>. If a model is to generalize well to unseen examples, minimizing overfitting to the data is necessary by ensuring the model's learning capacity (i.e., how much information it can learn) is comparable to the size of the target data distribution<sup>4</sup>. Therefore, a set of digital phantoms based on the XCAT is unlikely to provide enough variations to allow generalization of most ML models to actual clinical data. In this work, we propose a different approach, one based on using public

datasets to create a population of digital phantoms with sufficient variation for training a deep learning denoising method for use as part of the AdaptiSPECT-C reconstruction software.

## II. BACKGROUND AND RELATED WORK

### A. AdaptiSPECT-C System

AdaptiSPECT-C is a novel dynamic and adaptive dedicated clinical brain SPECT imaging system being developed to image patients with a variety of imaging agents for various imaging tasks. The current design<sup>5</sup> of the AdaptiSPECT-C system comprised of 23 pinhole apertures (4mm) embedded in a 2 cm thick hemispherical collimator aperture assembly irradiating 23 hexagonal NaI(Tl) detector modules.

## III. METHODS

To avoid the significant over-fitting of our deep denoising method, which is based on convolutional neural networks (CNNs), on a single anatomical model, we are currently using a dataset of 101 morphometric brain segmentations. The brain segmentations dataset, called Mindboggle<sup>6</sup>, is publicly available and based on T1-weighted MR images of 101 different healthy individuals (57 males, 44 females, ages range from 20-61, ethnic identity not provided). The segmented regions was performed following the Desikan–Killiany–Tourville (DKT) cortical labeling protocol which supports robust anatomical features geared toward automated processing<sup>7</sup>. The Mindboggle dataset was developed to provide a benchmark for functional, diffusion, and structural magnetic resonance imaging research. Our methods, on the other hand, focused on adapting this data for deriving digital phantoms which could be used to produce SPECT attenuation and activity maps for SPECT GATE<sup>8</sup> Monte Carlo simulations, which will then be used to train a deep denoising method.

To produce appropriate attenuation maps corresponding to each labeled brain image, our first operation was to replace the extracted scalp and skull regions. Using the original MRI data that was provided with the segmented brain images, we

performed a segmentation operation using the Freesurfer<sup>9</sup> tool to produce a volumetric image of just the scalp and skull regions (and the voids between). The images of the skull and scalp was combined with the pre-segmented brain regions and were assigned unique labels to differentiate these layers from the labeled cortical regions.

The next step is to produce attenuation and activity maps from the raw labeled slices. Using custom built software, we processed the slice data (combined scalp, skull, and brain regions), replacing the segmentation labels with an appropriate attenuation coefficient from a lookup table (i.e., based on tissue type such as bone, skin, white and gray matter). Similarly, a second set of slices was generated with the segmentation labels values being replaced with pre-determined relative activity concentrations. Because each cortical region was labeled with the appropriate tissue type, we replaced each white and gray-matter cortical labels with a value representing the appropriate concentrations of Tc-99m for our simulations for perfusion imaging. Our custom designed software provided an easy method to automate this process, which could be altered to produce different digital phantoms by varying activity concentrations. Example slices of one of the generated digital phantoms is shown in Figure 1.

#### IV. SIMULATIONS

The digital phantoms can now be used as source and attenuation distributions for SPECT GATE Monte Carlo simulations of AdaptiSPECT-C hardware creating projection images of the brain. We used our standard method of inputting the 3D regions representing structures of the head with the same relative concentration into GATE to simulation of the projections (acquisition) of them. Variations in source distributions can be achieved by combining separate projections of different structures and weighting them according to their prescribed relative concentrations to generate a low-noise projection set from which we derive multiple Poisson noise realizations for the desired count levels (administered activity). This provides variations in uptake, and noise realizations which can be used to augment the anatomies available to provide populations of simulated studies for training, validating and final imaging-task-performance studies<sup>10</sup>.

#### V. CONCLUSION

In conclusion, we have shown that overcoming limitation using traditional digital phantoms for training deep learning can be achieved by utilizing datasets from different domains and then adapting them to our purpose using opensource tools. Even though our target application is creating digital phantoms for SPECT GATE brain simulations, we believe this idea is applicable to a wide variety of other fields.

#### ACKNOWLEDGMENT

Research reported in this publication was supported by the National Institute of Biomedical Imaging and Bioengineering of the National Institutes of Health under Award Number R01EB022521 and supplement 3R01EB022521-03S1. The content is solely the responsibility of the authors and does not necessarily represent the official views of the National Institutes of Health.

#### REFERENCES

1. Segars WP, Sturgeon G, Mendonca S, Grimes J, Tsui BMW. 4D XCAT phantom for multimodality imaging research. *Med Phys.* 2010;37(9):4902-4915.
2. Poston A. Human Engineering Design Data Digest. In: DOD, ed2000.
3. Figueroa RL, Zeng-Treitler Q, Kandula S, Ngo LH. Predicting sample size required for classification performance. *BMC Med Inform Decis Mak.* 2012;12:8.
4. Goodfellow I, Bengio Y, Courville A. *Deep Learning.* The MIT Press; 2016.
5. Kesava Kalluri TF, Justin Goding, Yulun He, Arda K onik, Benjamin Auer, Soumyanil Banerjee, George Zubal, Lars Furenlid and Michael King. Multi-Pinhole Brain-SPECT: Design and Simulation of Imaging with XCAT Phantoms. Paper presented at: 6th International Workshop on Computational

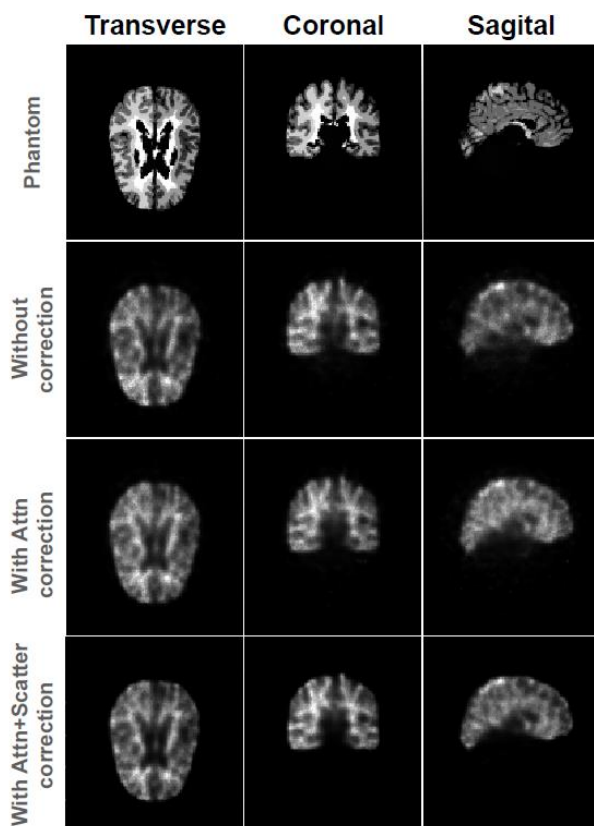


Fig 1. SPECT brain simulations performed using a digital phantom (top row) adapted from the Mindboggle brain segmentation data. Reconstruction images for 100 MLEM iterations using various correction of the phantom using our developed reconstruction software

Human Phantoms; August 28-30, 2017, 2017; Annapolis, MD, USA.

6. Klein A, Ghosh SS, Bao FS, et al. Mindboggling morphometry of human brains. *PLoS Computational Biology*. 2017;13(3).
7. Klein A, Tourville J. 101 Labeled Brain Images and a Consistent Human Cortical Labeling Protocol. *Frontiers in Neuroscience*. 2012;6(171).
8. Jan S, Santin G, Strul D, et al. GATE: a simulation toolkit for PET and SPECT. *Phys Med Biol*. 2004;49(19):4543-4561.
9. Dale AM, Fischl B, Sereno MI. Cortical surface-based analysis. I. Segmentation and surface reconstruction. *Neuroimage*. 1999;9(2):179-194.
10. King MA. Introduction to task-based assessment of image quality for investigators employing Monte Carlo simulation of imaging systems. In: Ljungberg M, Strand S-V, A. KM, eds. *Monte Carlo Calculations in Nuclear Medicine*. Second Edition ed. Boca Raton: CRC Press; 2012.

# Scientific Session

Tuesday, 23 July 2019

<b>9:00 – 10:40</b>	<b>Scientific Session “Phantom Development III”</b> <b>Chair: Wesley E. Bolch, Co-Chair: Niels Kuster</b>
9:00	Dynamic posture change method of mesh phantom based on motion capture system for accident dose reconstruction Yihan Jia, Rui Qiu, Zhen Wu, Chunyan Li, Hui Zhang, and Junli Li
9:20	Towards real-time 4D Monte Carlo dose calculation for radiation workers in motion Haegin Han, Chansoo Choi, Bangho Shin, Yeon Soo Yeom, and Chan Hyeong Kim
9:40	Assessing the realism of a 3D mammography phantom using radiomic texture features Raymond J. Acciavatti, Eric A. Cohen, Aimilia Gastounioti, Lauren Pantalone, Meng-Kang Hsieh, Jinbo Chen, Bruno Barufaldi, Predrag R. Bakic, Despina Kontos, and <u>Andrew D. A. Maidment</u>
10:00	A representative population of computer breast phantoms for virtual clinical trials Bruno Barufaldi, Predrag R. Bakic, and <u>Andrew D.A. Maidment</u>
10:20	Preliminary study on automatic organ segmentation using machine learning and application in personalized dosimetry for nuclear medicine Guoxun Zhang, Ruiyao Ma, Jiahao Wang, Liang He, Rui Qiu, Weibo Li, Junli Li

# Dynamic Posture Change Method of Mesh Phantom based on Motion Capture System for Accident Dose Reconstruction

Yihan Jia<sup>1</sup>, Rui Qiu<sup>1,\*</sup>, Zhen Wu<sup>1,3</sup>, Chunyan Li<sup>1,3</sup>, Hui Zhang<sup>1,2</sup>, Junli Li<sup>1,2</sup>

1. Department of Engineering Physics, Tsinghua University, Beijing, China

2. Key Laboratory of Particle & Radiation Imaging, Tsinghua University, Ministry of Education, Beijing, China

3. Joint Institute of Tsinghua University and Nuctech Company Limited, Beijing, China

\*Corresponding author: qiurui@mail.tsinghua.edu.cn

**Abstract**—Posture change of computational phantom is crucial for accidental dose evaluation, especially with acute uneven ionizing radiation. Although mesh-type phantom, compared with voxel-type phantom, is easier to change poses because of its deformability, posture change of polygonal mesh phantoms still depends heavily on manual operation, which is complicated and time-costing. In the present study, a posture change method based on motion capture system Kinect and 3D modeling software Blender is developed for posture change of mesh-type phantoms. Organs and bones are assembled into skin mesh to move as a whole. After voxelization and calculation in a dose calculation platform THUDose, accuracy is assessed with the dose reconstruction for a radiological accident at Nanjing(China).

**Index Terms**—motion capture; mesh-type phantom; posture change; polygonal meshes.

## I. INTRODUCTION

In radiation protection, computational human phantom is utilized to calculate effective doses in a simulated radiation field. Mesh-type phantom, following voxel phantom, is widely used for its deformability. [1] However, posture change of polygonal mesh phantoms still depends heavily on manual operation and causes errors on folded skin, costing a great deal of time to mend.

Various methods have been proposed to improve the flexibility of mesh phantoms. Vazquez J A modified CHAD phantom by adding spherical or hemispherical joints.[2] This method took motion capture data into consideration, but only as a reference of manual adjustment in Rhinoceros5. Yeon Soo Yeom used as-rigid-as-possible shape deformation algorithm to rotate segmented limbs with rotate matrix.[3] Chaoyong Ge adjusted CRAM\_S polygonal mesh phantom manually to convert standing posture to sitting posture. [4] In order to obtain phantoms of any posture more efficiently, in the present study, we developed a posture change method of mesh phantom that can utilize motion capture data directly and produce continuous posture sequence. The proposed method was then tested by simulating a radiological accident and compare calculated results with previous studies.

## II. METHODS

### A. The Collection of Motion Capture Data

Mo-Cap (short for Motion Capture) data can be obtained via a number of motion capture systems, such as VICON, OPTITRACK, etc. We adopted Kinect sensor, which features high-powered infrared camera and no need for motion capture suit. Besides, the full set of Kinect is at a relatively moderate price and highly portable.



Figure 1. Kinect sensor in our lab.

The most used MoCap data formats are C3D and BVH. C3D serves as the raw data exported by motion capture systems. BVH (short for Biovision Hierarchy) defines the markers as parent or child joints and build skeleton structure between these joints. In this work, we utilized Delicote NI Mate 2 to realize a real-time BVH file transfer to Blender.

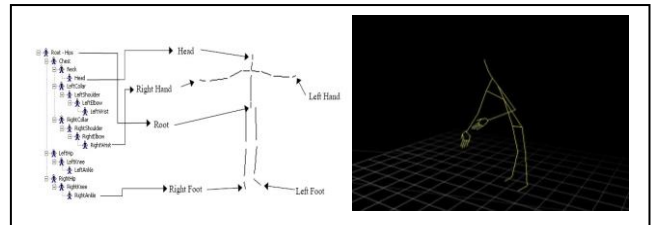


Figure 2. BVH skeletal structure [5] and the pose of sweeping floor demonstrated on NI Mate interface.

### B. Armature/rig Structure of CRAM\_S Mesh-type phantom

Firstly the skin of CRAM\_S female mesh phantom was imported to Blender from Rhinoceros 5 in OBJ format. Blender is an open-source 3D computer graphics software toolset used for creating animated films. We used the Rigify add-on to add a basic default armature (skeleton) to the skin model. Skin was then set parent to the skeleton to make them operate synchronously.

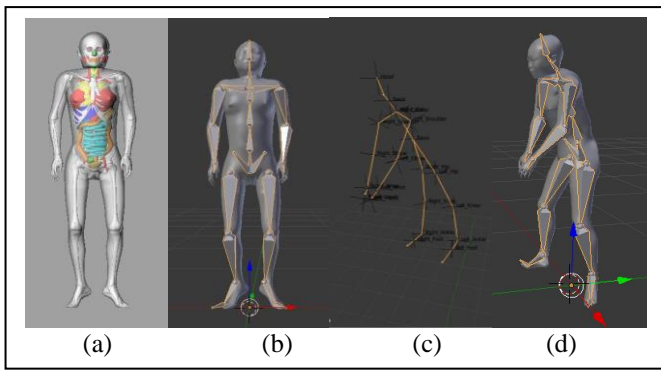


Figure 3. (a) Female of CRAM\_S. (b) Skin mesh linked with armature. (c) Kinect skeleton in sweeping posture imported to Blender. (d) Mesh phantom in sweeping posture.

The Kinect data was imported to Blender and builded a real-time skeleton. Then we copied the rotations of bones on Kinect skeleton and applied them on the mesh phantom skeleton.

### C. Assembly Process of Bones and Organs into Deformed Skin

Before the skin was deformed, we imported organs and bones in OBJ format from Rhinoceros 5 to Blender. Bones were inlayed into the skin shell, so that they could move with limbs automatically and realistically when we changed postures.

## III. SIMULATIONS

### A. Software: THUDose

THUDose is a toolkit for simulating radiation protection quantities using human phantoms developed by Tsinghua University based on Geant4. It integrates a wide range of functionality, including phantom conversion, physics simulation, statistics, and visualization components. [6]

Firstly, we voxelized every organ or tissue respectively. Secondly, each organ was labelled and assembled as a whole in Matlab. Then we define density and radiation weighting factor of every voxel according to the label of organ which contains that voxel. Finally, we input the information of source and conduct simulation.

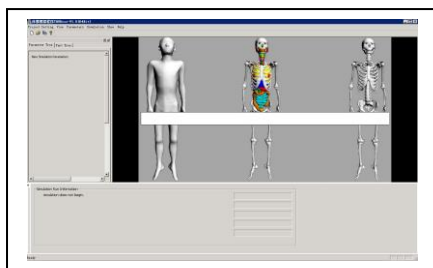


Figure 4. THUDose user interface.

### B. Accident Description

In this work, we simulate a radiological accident took place in Nanjing, China in 2014. In this accident, an industrial radiography source containing Ir-192 is picked up by a worker, causing acute radiation syndrome. The accident is a non-uniform irradiation and the organ dose is different at the standing and sitting posture according to a pervious study [6]. In this study, we recalculated organ doses at sitting posture and added other postures such as sweeping and walking, established with the pose change method proposed in this study.

## IV. CONCLUSION

In the present study, a posture change method based on motion capture system Kinect and 3D modeling software Blender is developed for posture change of mesh-type phantoms. Real-time MoCap data is imported to Blender in BVH format, vectoring the skeleton of imported polygonal skin of mesh phantom. Organs and bones are assembled into skin mesh to move as a whole. Finally the whole phantom is voxelized and calculated in THUDose. This method provides a convenient and quick way of obtaining mesh-type phantoms of any posture. It introduces interdisciplinary softwares and facilities and opens new thinking of cheap and more portable motion capture equipment. Furthermore, it avoids the conflicts and defects usually caused in polygonal mesh deformation and obtains realistic and flexible postures from a real-time motion sequence.

## ACKNOWLEDGMENT

This work was supported by the National Natural Science Foundation of China [Grant No. 11875036] and Tsinghua University Initiative Scientific Research Program [20151080355]. And I would like to show my gratitude to ACCAD motion lab of the Ohio State University for its MoCap Database.

## REFERENCES

- [1] Xu X G. "An exponential growth of computational phantom research in radiation protection, imaging, and radiotherapy: a review of the fifty-year history," *Physics in Medicine and Biology*, vol. 59, 18, 2014.
- [2] Justin A. Vazquez, Aiping Ding, Thomas Haley, Peter F. Caracappa, and X. George Xu. "A dose-reconstruction study of the 1997 Sarov criticality accident using animated dosimetry techniques," *Health Physics*, vol. 106, 5, 571-582, 2014.
- [3] Yeon Soo Yeom, Heagin Han, Chansoo Choi, Thang Tat Nguyen, Chan Hyeong Kim, et al. "Posture Change of Mesh-Type Computational Phantoms Using As-Rigid-As-Possible Shape Deformation Algorithm," *Proceedings of CP2017, 6<sup>th</sup> International Workshop on Computational Human Phantoms*, 2017, 16-17.
- [4] Chaoyong Ge. "Research on Deformation Technology and Application of Chinese Radiation Protection Reference Man," (In Chinese). Unpublished master dissertation, Tsinghua University, 2014.
- [5] BVH Motion Capture Data Animated , <http://www.cs.cityu.edu.hk/~howard/Teaching/CS4185-5185-2007-SemA/Group12/BVH.html>
- [6] Lu W , Wu Z , Qiu R , et al. "Physical Dosimetric Reconstruction of a Radiological Accident at Nanjing (China) for Clinical Treatment Using Thudose," *Health Physics*, vol. 113, 5, 327-334, 2017.

# Towards Real-time 4D Monte Carlo Dose Calculation for Radiation Workers in Motion

Haegin Han<sup>1</sup>, Chansoo Choi<sup>1</sup>, Bangho Shin<sup>1</sup>, Yeon Soo Yeom<sup>2</sup>, and Chan Hyeong Kim<sup>1,\*</sup>

<sup>1</sup>Department of Nuclear Engineering, Hanyang University, Seoul, Korea

<sup>2</sup>Division of Cancer Epidemiology and Genetics, National Cancer Institute, National Institute of Health, Bethesda, MD, USA

\*Corresponding author: chkim@hanyang.ac.kr

**Abstract**—For real-time 4D Monte Carlo dose calculation for radiation workers in motion, in the present study, a Geant4-based program was developed, which rapidly deforms the posture of a mesh-type computational phantom, i.e., within a few seconds, and directly calculate organ doses for the deformed phantoms. The computation procedures were parallelized by using MPI library, so that the performance can be further improved when a large number of nodes are secured. The developed program was used to calculate the time variation of organ absorbed doses for the data obtained from a motion capture system.

**Index Terms**—tetrahedral mesh phantom, posture, 4D Monte Carlo, Geant4, deformation

## I. INTRODUCTION

Recently, a tetrahedral mesh phantom was introduced by Yeom *et al.* [1], which overcomes most limitations of voxel phantoms, without exceedingly degrading the computational speed for dose calculations [2]. Acknowledging the advantages of mesh phantoms, in 2016, the ICRP decided to convert the current voxel-type reference phantoms into mesh, developing Mesh-type Reference Computational Phantoms (MRCPs). ICRP Task Group 103, which has undertaken this project, recently completed the conversion for adult male and female [3] and ICRP *Publication* on adult MRCPs will be released this year. The newly constructed phantoms are the first reference phantoms that include all the radiosensitive layers required for effective dose calculation, and at the same time they can be easily deformed into different body shapes or postures.

Taking these advantages, Yeom *et al.* [4] calculated dose coefficients for five different postures by using the deformed adult MRCPs. The result showed that posture can have a significant effect on organ absorbed doses, emphasizing the importance of consideration of postures. The methodology used by Yeom *et al.* [4], however, involves ~12 hours of automatic procedure and few days of additional manual procedure to construct a single posture-deformed MRCP, and thus it is impractical to be used for dose calculations for dynamic motion, especially when the duration of motion is over several minutes. Therefore, in the present study, we developed a Geant4-based program for real-time 4D Monte Carlo dose calculation for radiation workers in motion, which can rapidly deform the posture of mesh phantom, i.e., within a few seconds, and directly calculate doses for the deformed phantom. The developed program was then used to calculate organ absorbed doses for dynamic posture data obtained from a motion capture system.

## II. METHODS

### A. Construction of Stabilized Tetrahedral Mesh Phantom

In the present study, the adult male MRCP was separated into organless body phantom to be deformed in real-time and internal organ model to be pre-deformed as a database. Then, the organless phantom was slightly modified for mesh stabilization and the secure of enough space between bones in joint area. A database was constructed for internal organ models because they cannot be deformed in real-time due to the current limited computational performance.

### B. Posture Deformation Methodology

For the posture deformation of the organless body phantom, it was first segmented into 13 joint regions and each joint was deformed in sequence according to the corresponding rotation matrix provided by motion data. The mesh in each region was deformed by using the technique based on volumetric graph Laplacian (VGL) [5] which alleviated unnatural volume changes and local self-intersections for large deformations.

The database for internal organ phantoms was constructed by deforming them according to the rotation of spine joint. For this, rotation matrices to cover the range of spine joint movement were first selected, and the internal organ phantom was deformed for the selected matrices by using as-rigid-as-possible algorithm [6] which can be better applied to the rather complicated meshes than the technique based on VGL. For each rotation matrix, the outer skin surface of correspondingly deformed organless phantom was also considered to prevent the internal organ phantoms from being exposed.

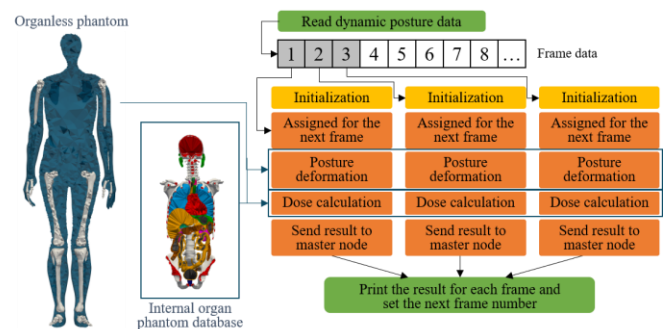


Figure 1. Procedure flow chart for the 4D Monte Carlo simulation program for posture-changing mesh phantom developed in the present study.

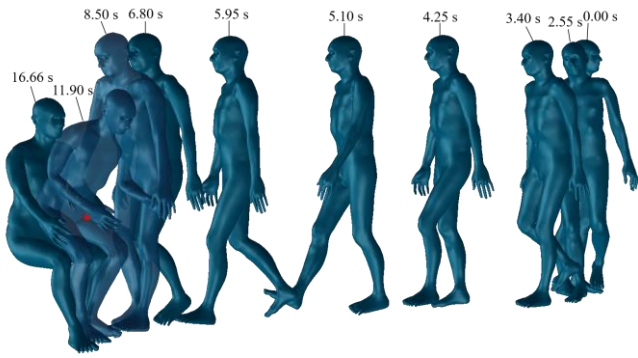


Figure 2. Position of  $^{60}\text{Co}$  source (red spot) and phantoms deformed by posture data obtained from motion capture system.

### C. Geant4-based 4D Monte Carlo Simulation Program

An integrated 4D Monte Carlo simulation program was developed by implementing a dedicated C++ program for posture deformation into Geant4 code, enabling it to calculate doses by directly using the deformed phantom data. For dose calculations, the separated internal organ models were also installed in the posture-deformed frame phantom by using the parallel world geometry feature of Geant4. The sequential tasks of deforming phantom and calculating doses were parallelized by MPI (Message Passing Interface), so that one task after another for each frame can be assigned to each node at the end of the task for previous frame. For the verification, the developed program was used to calculate time-dependent organ absorbed doses to 37MBq  $^{60}\text{Co}$  point source by using the posture data file in BVH (Biovision Hierarchy) format obtained from motion capture system. The simulations were performed on 40 cores of the Intel® Xeon® CPU E5-2698 v4 (@ 2.20 GHz CPU processor and 256 GB Memory).

### III. RESULT

Figure 2 shows the position of  $^{60}\text{Co}$  source and ten posture-deformed phantoms among the 98 phantoms (frame time: 0.17 s). It can be seen that the phantoms were deformed in realistic appearance both for walking and sitting motions. The volume loss by deformation was less than 3% for all the frames, and it was even less than 0.2% when we consider only walking frames (0-6.8 s).

Figure 3 shows the time-dependent organ-averaged absorbed doses calculated in the present study, for colon, liver, brain, and lungs. It can be seen that the organ doses for all organs gradually increase as the phantom walks toward the source (0-6.8 s), and that they plateau while it turns around to sit (6.8-10 s). Then a sudden drop follows during a short period at which the source is blocked by the right hand, and finally the doses increases as the phantom sits and plateaus after completion of sitting. It can also be seen that when the source is near the phantom (6.8-16.66 s), the organs near at the source level receive higher doses.

The initialization time was  $\sim 4$  min, and the time interval between frames at which the next phantom geometry is registered was  $\sim 90$  s. For the tasks for each frame, the time required for posture deformation was 4.5 s, and the averaged computation time for particle transportation, which may have large variance depending on the source position and energy, was  $\sim 0.04$  ms per event (transportation of a primary particle) in the present study.

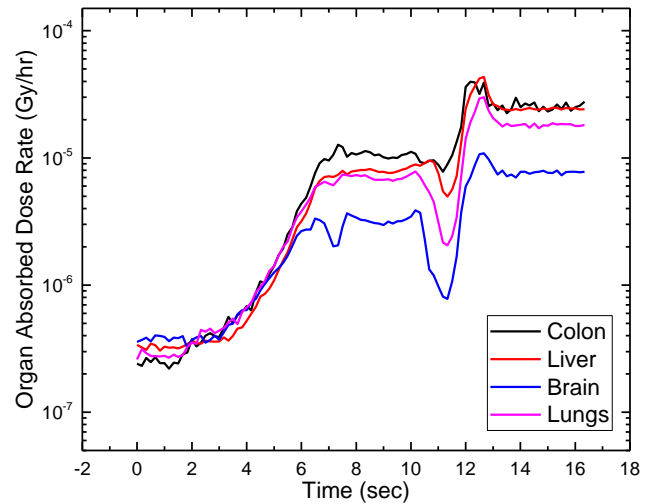


Figure 3. Variation of organ-average absorbed dose as function of time for colon, liver, brain, and lungs, calculated by using the phantoms deformed into continuous postures by using the data from motion capture system.

### IV. CONCLUSION

In the present study, a Geant4-based program for real-time 4D Monte Carlo dose calculation for radiation workers in motion was developed by integrating stable and fast posture deformation technique and Geant4-based simulation code. The developed program was coupled with posture data obtained from motion capture system and was used to calculate time-dependent organs doses for walking and sitting motions. To maximize the computation performance, the task for each frame was parallelized by MPI, and thus the computation speed can be further improved when a large number of nodes are secured. The final goal of the present study is to enable real-time organ dose monitoring by loading the motion data by streaming. When this succeeds, the program may be highly useful in various fields involving high radiation exposure situations, including high-dose radiation task and accident dose reconstructions.

### REFERENCES

- [1] Y. S. Yeom, J. H. Jeong, M. C. Han, and C. H. Kim, "Tetrahedral-mesh-based computational human phantom for fast Monte Carlo dose calculations," *Phys. Med. Biol.*, vol. 59, pp. 3173–3185, 2014.
- [2] C. Choi, Y. S. Yeom, M. C. Han, and T. T. Nguyen, "Computational Performance Evaluation of Monte Carlo Particle Transport Codes for Mesh-type ICRP Reference Computational Phantoms," *Trans. Korean Nucl. Soc. Spring Mtg.*, pp.300-301, 2018.
- [3] C. H. Kim *et al.*, "New mesh-type phantoms and their dosimetric applications, including emergencies," *Ann. ICRP*, vol. 47, pp.45-62, 2018.
- [4] Y. S. Yeom *et al.*, "Posture-dependent dose coefficients of mesh-type ICRP reference computational phantoms for photon external exposures," *Health Phys.*, in press.
- [5] K. Zhou *et al.*, "Large Mesh Deformation Using the Volumetric Graph Laplacian," *ACM Trans. Graph.*, vol. 24, pp. 496–503, 2005.
- [6] H. Yan *et al.* "Shape deformation using a skeleton to drive simplex transformations." *IEEE Tran. Vis. and Comput. Graph.*, vol. 14, pp. 693-706, 2008.

# Assessing the Realism of a 3D Mammography Phantom Using Radiomic Texture Features

Raymond J. Acciavatti\*, Eric A. Cohen, Aimilia Gastouniotti, Lauren Pantalone, Meng-Kang Hsieh, Jinbo Chen, Bruno Barufaldi, Predrag R. Bakic, Despina Kontos, and Andrew D. A. Maidment

Department of Radiology, Perelman School of Medicine at the University of Pennsylvania, Philadelphia, USA

\*Corresponding author: Raymond.Acciavatti@uphs.upenn.edu

**Abstract**—We assess the realism of a physical phantom for digital breast tomosynthesis (DBT) using radiomic texture features. These features measure breast parenchymal patterns, and may be indicators of breast cancer risk. The phantom was 3D printed based on a computational model of fibroglandular and adipose tissue developed by the University of Pennsylvania. X-ray images of the phantom were acquired with a clinical DBT system, and subsequently, 343 texture features were determined with a lattice-based pipeline. These calculations were done in the central slice of the reconstruction, as well as the synthetic 2D mammogram. Each feature was compared against the distribution of values in a clinical population with negative screening mammograms. The percentile rank relative to the clinical distribution was used to measure whether each feature in the phantom was an outlier. In the reconstruction, most features in the phantom were found to be realistic. The phantom lacked realism in terms of fine textural detail (for example, some co-occurrence and run-length features). In synthetic 2D imaging, fewer features were realistic. The realism of the phantom is therefore sensitive to the image processing method. There are inherent limitations to the fine detail that can be created with 3D printing, and hence future work should analyze virtual phantoms that can be simulated with even finer detail.

**Index Terms**—radiomics, digital breast tomosynthesis, image acquisition, image reconstruction, anthropomorphic phantom.

## I. INTRODUCTION

We analyze the realism of a physical phantom for DBT using radiomic texture features. The phantom was 3D printed by Computerized Imaging Reference Systems, Inc. (Norfolk, VA) under license from the University of Pennsylvania (Figure 1). The phantom is based on a computational breast model [1]-[4] that is used in virtual clinical trials (VCTs).

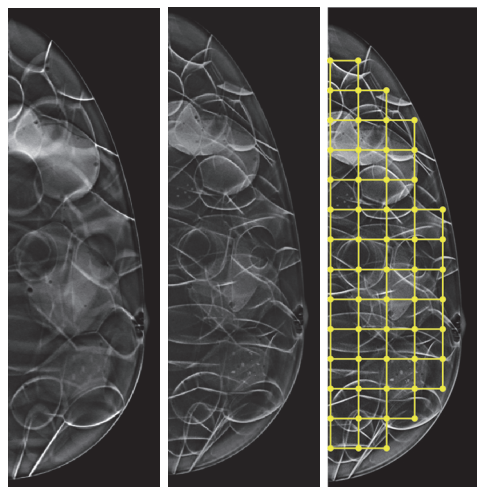
Our previous work demonstrated that VCTs can reproduce the results of a clinical trial [5], specifically the trial by Rafferty *et al.* comparing DBT and 2D digital mammography [6]. In VCTs, the characteristics of the phantoms should match a clinical population. Our previous work developed a method for matching breast density and thickness [7]. This paper develops a framework for assessing whether radiomic texture features are also matched.

## II. METHODS

Texture features in the phantom were compared against a screening population of 1,000 women with negative

mammograms. The data were obtained with the Selenia Dimensions DBT system (Hologic Inc., Bedford, MA) at the University of Pennsylvania. We analyzed the central slice of the reconstruction and the C-View™ image (a synthetic 2D mammogram) in mediolateral oblique (MLO) views. Multiple square windows were overlaid on each image, and texture features were calculated in each window [8]. The window width and the distance between adjacent windows were both set to 6.3 mm. The features were averaged over the windows.

Figure 1. Central slice of reconstruction (left), C-View™ image (center), and illustration of lattice for feature calculations (right).

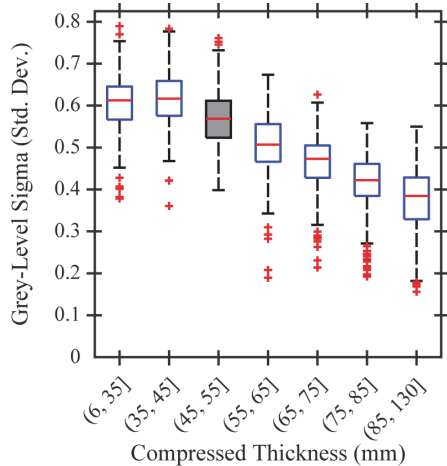


In the clinical data set, it was determined that features vary based on compressed breast thickness. An example of a feature (grey-level standard deviation in the reconstruction) demonstrating this idea is shown in Figure 2. For this reason, texture features in the phantom (50 mm thick) were compared against the subgroup of patients with comparable thickness (45-55 mm). In this subgroup of patients, the kV ranged between 30 and 32. The auto-timed settings for the phantom were 53, 43, and 36 mAs at these three respective kV. Each of these acquisitions was repeated twice with the phantom in the same position.

For each feature, the six data points derived from the phantom were compared against the clinical distribution. A feature was considered realistic in the phantom if all six data points were found to have a percentile rank between 2.5% and

97.5%, corresponding to the middle 95% of the clinical distribution [9]. Otherwise, a feature was considered unrealistic. Figure 3 shows an example of a realistic feature (grey-level sum) in synthetic 2D imaging. The six data points for the phantom (in red) are shown below the clinical distribution. We also investigated the effect of introducing a less stringent definition of realism; namely, features within the middle 99% of the clinical distribution were considered realistic.

Figure 2. Illustration of the thickness dependency of a feature in the central slice of the reconstruction.



### III. RESULTS

Table 1 provides a summary of the features demonstrating clinical realism. If realism is defined in terms of the middle 95% of the clinical distribution, it can be shown that 70.6% of features are realistic in the reconstruction (63.6% in synthetic 2D imaging). By contrast, if a less stringent definition of realism is applied, a larger number of features can be considered realistic; specifically, 86.6% of features in the reconstruction (84.8% in synthetic 2D imaging).

TABLE I. PERCENTAGE OF REALISTIC FEATURES.

Feature Family (Number of Features)	Reconstruction	Synthetic 2D
Co-occurrence (8)	50% <sup>a</sup> (62.5% <sup>b</sup> )	25% (50%)
Co-occurrence Laws (120)	52.5% (75%)	50% (73.3%)
Fractal Dimension (2)	50% (100%)	50% (50%)
Gabor Wavelet (32)	100% (100%)	100% (100%)
Grey Level (12)	100% (100%)	50% (75%)
Laws (125)	80.8% (95.2%)	72% (96%)
LBP (36)	69.4% (88.9%)	63.9% (86.1%)
Power Spectrum (1)	100% (100%)	0% (0%)
Run Length (7)	42.9% (57.1%)	57.1% (85.7%)

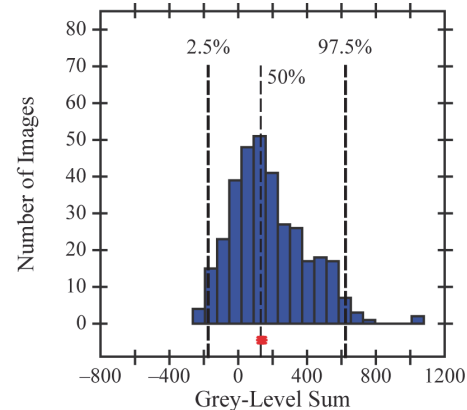
a. Realism based on middle 95% of clinical distribution  
b. Realism based on middle 99% of clinical distribution

### IV. CONCLUSION

Texture features in the phantom were overall realistic. The phantom lacks realism in terms of fine textural detail (for example, some co-occurrence and run-length features). We demonstrated that these results are sensitive to the way realism is defined. If a less stringent definition is introduced, more features were found to exhibit realism. Future work should

explore similar calculations in computational phantoms, which can be simulated with even finer detail than a physical phantom.

Figure 3. Example of a feature that exhibits realism in synthetic 2D imaging.



### ACKNOWLEDGMENT

Support was provided by grants R01CA154444, R01CA161749 and U54CA163313 from the National Institute of Health, and Burroughs-Wellcome Fund IRSA 1016451. The content is solely the responsibility of the authors and does not necessarily represent the official views of the funding agencies.

### REFERENCES

- [1] P. R. Bakic, C. Zhang, and A. D. A. Maidment, "Development and characterization of an anthropomorphic breast software phantom based upon region-growing algorithm," *Med. Phys.*, vol. 38, pp. 3165-3176, 2011.
- [2] A. Carton, P. Bakic, C. Ullberg, H. Derand, and A. D. A. Maidment, "Development of a physical 3D anthropomorphic breast phantom," *Med. Phys.*, vol. 38, pp. 891-896, 2011.
- [3] D. D. Pokrajac, A. D. A. Maidment, and P. R. Bakic, "Optimized generation of high resolution breast anthropomorphic software phantoms," *Med. Phys.*, vol. 39, pp. 2290-2302, 2012.
- [4] J. H. Chui, D. D. Pokrajac, A. D. A. Maidment, and P. R. Bakic, "Towards breast anatomy simulation using GPUs," *Lect. Notes Comput. Sci.*, vol. 7361, 506-513, 2012.
- [5] P. R. Bakic, B. Barufaldi, D. Higginbotham, S. P. Weinstein, A. N. Avanaki *et al.*, "Virtual clinical trial of lesion detection in digital mammography and digital breast tomosynthesis," *Proceedings of SPIE, SPIE Medical Imaging*, 2018, pp. 1057306-1 - 13.
- [6] E. A. Rafferty, J. M. Park, L. E. Philpotts, S. P. Ptoplack, J. H. Sumkin *et al.*, "Assessing radiologist performance using combined digital mammography and breast tomosynthesis compared with digital mammography alone: results of a multicenter, multireader trial," *Radiol.*, vol. 266, pp. 104-113, 2013.
- [7] B. Barufaldi, P. R. Bakic, D. Pokrajac, M. A. Lago, and A. D. A. Maidment, "Developing populations of software breast phantoms for virtual clinical trials," *Proceedings of SPIE, 14th International Workshop on Breast Imaging*, 2018, pp. 107181U-1 -9.
- [8] Y. Zheng, B. M. Keller, S. Ray, Y. Wang, E. F. Conant *et al.*, "Parenchymal textural analysis in digital mammography: a fully automated pipeline for breast cancer risk assessment," *Med. Phys.*, vol. 42, pp. 4149-4160, 2015.
- [9] R. J. Acciavatti, M. Hsieh, A. Gastouniotti, Y. Hu, J. Chen *et al.*, "Validation of the textural realism of a 3D anthropomorphic phantom for digital breast tomosynthesis," *Proceedings of SPIE, 14th International Workshop on Breast Imaging*, 2018, pp. 107180R-1 -8.

# A Representative Population of Computer Breast Phantoms for Virtual Clinical Trials

Bruno Barufaldi\*, Predrag R. Bakic, and Andrew D.A Maidment  
Department of Radiology, University of Pennsylvania, Philadelphia, US  
\*Corresponding author: Bruno.Barufaldi@uphs.upenn.edu

**Abstract**— Virtual Clinical Trials (VCTs) have been widely used for the evaluation of novel imaging systems through computer simulations. The virtual population of interest has an important role and affects directly the performance of VCTs. We developed a method for selecting representative populations of software breast phantoms to match the clinical distribution of breast thickness and percent density. The method was developed using clinical images of 10,705 women from the PROSPR study. Sub-populations were identified by  $k$ -means clustering to select patient-specific demographic features. Using 24 representative phantoms, we successfully matched the analyzed clinical population completely for the compressed breast thickness, and within three percentage points of the volumetric breast density.

**Index Terms**—Virtual clinical trial; anthropomorphic breast phantom; GPU programming;

## I. INTRODUCTION

We have developed an open-source virtual clinical trial (VCT) framework, which consists of a GPU-accelerated pipeline for the generation of computer breast phantoms and the simulation of imaging modalities: digital mammography (DM) and digital breast tomosynthesis (DBT). The performance of VCTs critically depends on the phantoms used. In this paper, we present a method for selecting a population of software phantoms to match the clinical distribution of compressed thickness and percent density of the breast.

## II. MATERIALS AND METHODS

The method for determining representative breast phantom populations is illustrated in Figure 1.

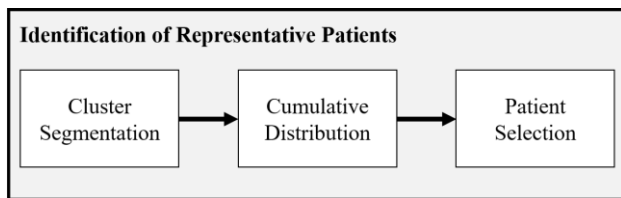


Figure 1. Flowchart that describes the method for determining representative breast phantom populations.

The clinical population consists of 10,705 women who had their screening exams at the Breast Imaging Center of the Hospital of the University of Pennsylvania, as part of an ongoing NIH Population-based Research Optimizing Screening through Personalized Regimes (PROSPR) Network grant [1] (Table I). For the purpose of developing a virtual population, we extracted the compressed breast thickness (CBT) information from anonymized DICOM headers of clinical

images, and calculated the breast percent density (PD%) from the clinical mammograms using the LIBRA software [2].

TABLE I. SUMMARY THE PROSPR POPULATION USED IN THIS STUDY.

Number of Patients, n	10,705
Number of Images, n	63,427
Compressed Breast Thickness, mm (avg $\pm$ SD)	54.48 $\pm$ 13.02
Breast Dense Area, % (avg $\pm$ SD)	21.06 $\pm$ 14.93
Age, years (avg $\pm$ SD)	56.62 $\pm$ 11.05

To identify clusters of clinical sub-populations, we used the  $k$ -means method, available in the clustering toolkit of MATLAB R2017b (MathWorks Inc., Natick, MA). This approach separates the clinical data into ' $k$ ' clusters and associates each data sample with the nearest cluster mean. In this study, we used  $k=2$  to obtain a bi-modal distribution of our clinical data, in terms of PD% and CBT.

A set of representative patients was selected from each cluster as follows: We have determined the number of representative patients by the relative probability of each cluster. The patients in each cluster were binned based upon their distance from the cluster center (in the density – thickness space), then the cumulative distribution of those distances was calculated. We used the cumulative distribution to randomly select 24 representative patients. The CBT and PD% from representative patients were used to inform the generation of breast phantoms.

## III. SIMULATIONS

We used our VCT pipeline [3], [4] to develop populations of software breast phantoms. These breast phantoms simulate normal breast anatomy using an efficient recursive partitioning algorithm optimized to minimize computational complexity [5]. To generate representative software breast phantoms, we varied the parameters that controls the volumetric breast density [5] to match the PD% selected after selecting the clinical patient. We used the method described by Gastouniotti *et. al* to estimate the PD% from the volumetric breast density [6]. We also varied the parameters that controls the shape, volume and size of our software breast phantoms to match the CBT selected after selecting the clinical patient [5].

The simulation of mammographic breast compression uses a GPU accelerated 3D mapping technique with pre-calculated compression meshes [7]. To further save the computational time, instead of individual meshes for each phantom, we have used four scalable template meshes that correspond to the patients' breast dimensions. The CBT and PD% for the selected patients are listed in Table II.

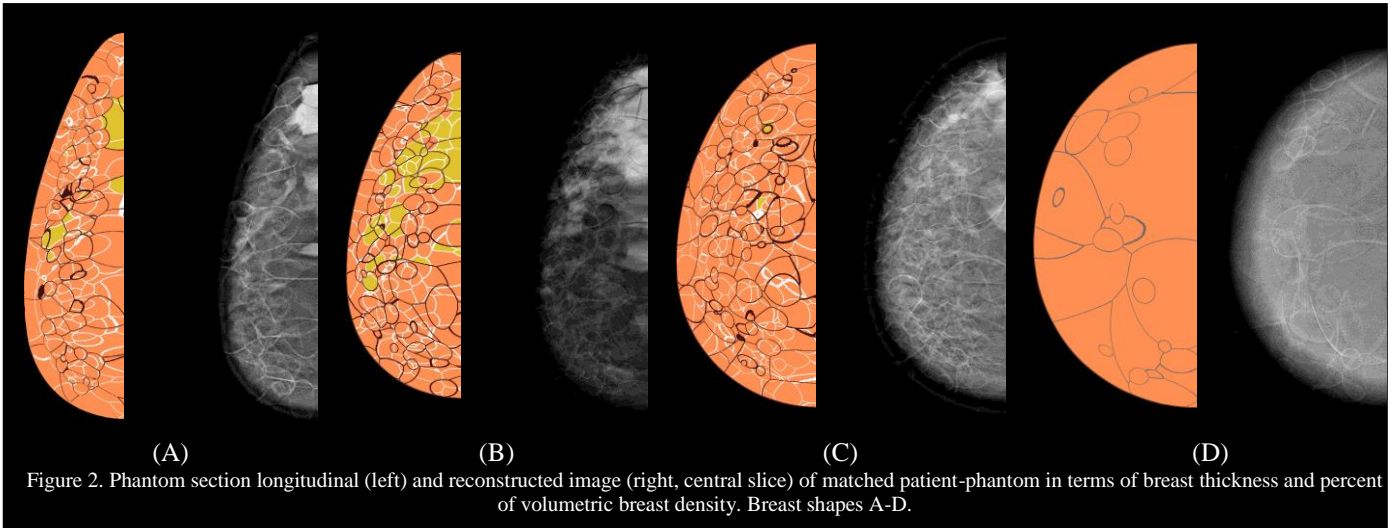


Figure 2. Phantom section longitudinal (left) and reconstructed image (right, central slice) of matched patient-phantom in terms of breast thickness and percent of volumetric breast density. Breast shapes A-D.

The DBT image acquisition is simulated using the Siddon method for GPU [8]. Reconstructed DBT images are generated using a reconstruction method under research license with Real-Time Tomography [9].

TABLE II. Representative patients selected from clusters 1 and 2.

Cluster 1								
Patient ID	1	2	3	4	5	6	7	8
CBT (mm)	61	42	53	66	56	70	63	55
PD (%)	4.7	14.5	8.8	19.6	7.7	13.6	19.1	6.2
Cluster 2								
Patient ID	9	10	11	12	13	14	15	16
CBT (mm)	56	58	54	58	63	70	45	61
PD (%)	10.9	16.9	18.6	5.7	4.4	3.0	6.0	3.1
Cluster 2								
Patient ID	17	18	19	20	21	22	23	24
CBT (mm)	48	48	50	35	29	38	36	50
PD (%)	35	30.1	56.5	74.9	11.6	13.4	17.2	34.8

We illustrate the selected virtual population with four exemplars matching the four sub-populations (associated with the four template meshes). Figure 2 shows phantom sections (central slice, longitudinal) and reconstructed tomosynthesis images from the four phantoms. Table III compares the values of the compressed breast thickness and volumetric breast density from the four phantoms and their corresponding representative patients, which show a good agreement.

TABLE III. Four examples of different breast shapes of the matched phantom-patient population.

Matched Patient (ID)	Patient VBD (%)	Phantom VBD (%)	Difference VBD (%)	Patient CBT (mm)	Phantom CBT (mm)	Difference CBT (%)
22	13.55	16.61	3.06	38	38	0
24	25.19	24.99	-0.20	50	50	0
10	15.77	16.77	1.00	58	58	0
14	5.07	3.46	-1.73	70	70	0

#### IV. CONCLUSION

The method for developing virtual populations for VCTs identifying representative clinical patients and generate software breast phantoms was illustrated using sample phantoms, which showed very good agreement with the clinical data. The matched set of representative phantoms can

be used to generate an arbitrary large virtual database by varying their internal composition. Future work includes additional validation of the software breast phantoms and simulation of additional clinical information (e.g., estimated breast volume or parenchymal descriptors) for more accurate selection of the phantom parameters.

#### References

- [1] National Cancer Institute, "PROSPR: Population-based research optimizing screening through personalized regimens," 2017. [Online]. Available: <https://healthcaredelivery.cancer.gov/prospr/>.
- [2] B. M. Keller, D. L. Nathan, Y. Wang, Y. Zheng, J. C. Gee, E. F. Conant, and D. Kontos, "Estimation of breast percent density in raw and processed full field digital mammography images via adaptive fuzzy c-means clustering and support vector machine segmentation," *Med. Phys.*, vol. 39, no. August, pp. 4903–4917, 2012.
- [3] B. Barufaldi, P. R. Bakic, D. Higginbotham, D. D. Pokrajac, and A. D. A. Maidment, "A GPU-Accelerated Virtual Clinical Trial Pipeline for Digital Breast Tomosynthesis," in *6th International Workshop on Computational Human Phantoms*, 2017, pp. 100–1.
- [4] B. Barufaldi, P. R. Bakic, D. Higginbotham, and A. D. A. Maidment, "OpenVCT: a GPU-accelerated virtual clinical trial pipeline for mammography and digital breast tomosynthesis," in *SPIE Medical Imaging 2018*, 2018, vol. 1057358, no. March, pp. 1–8.
- [5] P. R. Bakic, B. Barufaldi, D. Pokrajac, S. P. Weinstein, and A. D. Maidment, "Optimized simulation of breast anatomy for virtual clinical trials," in *14th International Workshop on Breast Imaging (IWBI 2018)*, 2018, no. July, p. 73.
- [6] A. Gastouniotti, M. Hsieh, E. F. Conant, D. Kontos, A. Gastouniotti, M. Hsieh, L. Pantalone, and E. F. Conant, "Volumetric versus area-based density assessment: comparisons using automated quantitative measurements from a large screening cohort," in *SPIE Medical Imaging 2015*, 2018, no. March, p. 105742H–1.
- [7] M. A. Lago, A. D. A. Maidment, and P. R. Bakic, "Modelling of mammographic compression of anthropomorphic software breast phantom using FEBio," in *Int'l Symposium on Computer Methods in Biomechanics and Biomedical Engineering*, 2013.
- [8] M. De Greef, J. Crezee, J. C. Van Eijk, R. Pool, and A. Bel, "Accelerated ray tracing for radiotherapy dose calculations on a GPU," *Med. Phys.*, vol. 36, no. 9, pp. 4095–4102, 2009.
- [9] J. Kuo, P. A. Ringer, S. G. Fallows, P. R. Bakic, A. D. A. Maidment, and S. Ng, "Dynamic reconstruction and rendering of 3D tomosynthesis images," in *SPIE Medical Imaging*, 2011, vol. 796116, no. March 2011, pp. 796116–796116–11.

# Preliminary study on automatic organ segmentation using machine learning and application in personalized dosimetry for nuclear medicine

Guoxun Zhang<sup>1,2</sup>, Ruiyao Ma<sup>1,2,3</sup>, Jiahao Wang<sup>1,2</sup>, Liang He<sup>1,2</sup>, Rui Qiu<sup>1,2</sup>\*, Weibo Li<sup>3</sup>, Junli Li<sup>1,2</sup>

1. Department of Engineering Physics, Tsinghua University, Beijing, China

2. Key Laboratory of Particle & Radiation Imaging, Tsinghua University, Ministry of Education, Beijing, China

3. Institute of Radiation Medicine, Helmholtz Zentrum München, German Research Center for Environmental Health, München, Germany

\*Corresponding author: qiurui@mail.tsinghua.edu.cn

**Abstract**—The computational phantom is widely used in the field of radiation protection calculation. Development of personalized phantoms is of great significance for the accuracy of radiation dose calculations. However, the traditional manual or semi-automatic modeling methods are cumbersome and time-consuming, which is not conducive to the practical application of personalized phantoms. The large-scale application of artificial intelligence in the field of image segmentation in recent years has inspired the possibility of automatic modeling of personalized phantoms. In this paper, we present a cascade U-net for automatically segmenting organs to model personalized phantoms based on the deep learning method. The cascade U-Net models several thoracic organs and several abdominal organs by inputting a set of CT data. The cascade U-Net consists of two U-Nets, which can complete the overall process in minutes. Preliminary study on the application of this method is performed for a clinical case in nuclear medicine. A patient specific phantom is developed using this method and organ dose is calculated with Monte Carlo simulation with this phantom.

**Index Terms**—patient-specific phantoms; neural network; radiation dose

## I. INTRODUCTION

For decades, radiation dose assessment using human computational models has become a significant topic in radiation protection, medical imaging and radiation therapy [1]. Reference phantoms are usually used in Monte Carlo simulation to obtain the organ dose or effective dose. However, there are differences between individual patients and the reference model in many aspect, such as anatomical differences, the weight and position of patients' organs, body characteristics, height, and weight are often different from the data of phantoms. Moreover, the biokinetic model is not completely consistent with the reference model and it affects the accuracy of the dose calculation. For radiodiagnosis, the differences of organ weight and position have a great impact on the dose calculation results, especially for organs on the edge of the scanning field. In order to achieve more accurate dose assessment results, how to accurately and quickly model personalized phantoms is major open challenge that we are currently confronting [2,3].

Relevant research institutions all over the world have carried out a series of studies on personalized phantom modeling, and the methods can be roughly divided into three types. The first method is to manually segment the organs directly from the individual medical images to model personalized phantoms. For example, MC Gosselin et al. of IT'IS Foundation manually segmented more than 300 tissues or organs from MRI images, and established a ViP phantom library through a series of personalized model generation and processing[4]. The establishment of each personalized phantom takes months or even longer. The second method is to adjust the existing phantoms, construct a model library of different height and weight, and then select the phantom close to the actual individual according to the needs. For example, in 2009, Bolch research team at the University of Florida in the United States transformed the existing UF adult male phantom to establish a male adult phantom with lighter weight, average weight, and heavier weight[5]. In 2010, George Xu research team at RPI established personalized phantoms of different height and weight of RPI phantom by adjusting the quality of skin and some organs[6]. The third method is to extract surface data such as skin according to individual medical images, and construct personalized phantoms by performing overall or partial scaling and quality adjustment on the standard phantom. For example, Segars et al. at Duke University scale the head and limbs of the original XCAT model to splice on a segmented torso model. They obtain personalized model library of Duke University by meticulous splicing and adjustment[7]. Bryn et al. of the IT'IS Foundation used skin data from CT as a registration basis to deform existing phantoms to obtain personalized phantoms[8].

In this paper, we describe a novel method based on a cascade U-net[9] for fully automatic and fast personalized body phantom modeling. Our result demonstrates that after training dozens of hours, our cascade U-Net can model several thoracic organs and several abdominal organs within several minutes.

## II. METHODS

### A. Cascade U-net

We define a deep learning network called cascade U-net[9] which consists of two U-Nets in Fig.1. The first U-Net down samples the imputed 3D CT stack, which will greatly reduce the computational burden of GPU. And the first U-Net will output the location of the target organ. Then the second U-Net will finely segment the target area to obtain the final 3D organ segmentation result. Each of the two U-Nets is made up of 23 convolutional layers and every two convolutional layers are followed by a nonlinear activation layer (ReLU function) and a pooling layer. The final output of cascade U-Net is classified by a softmax classification layer.

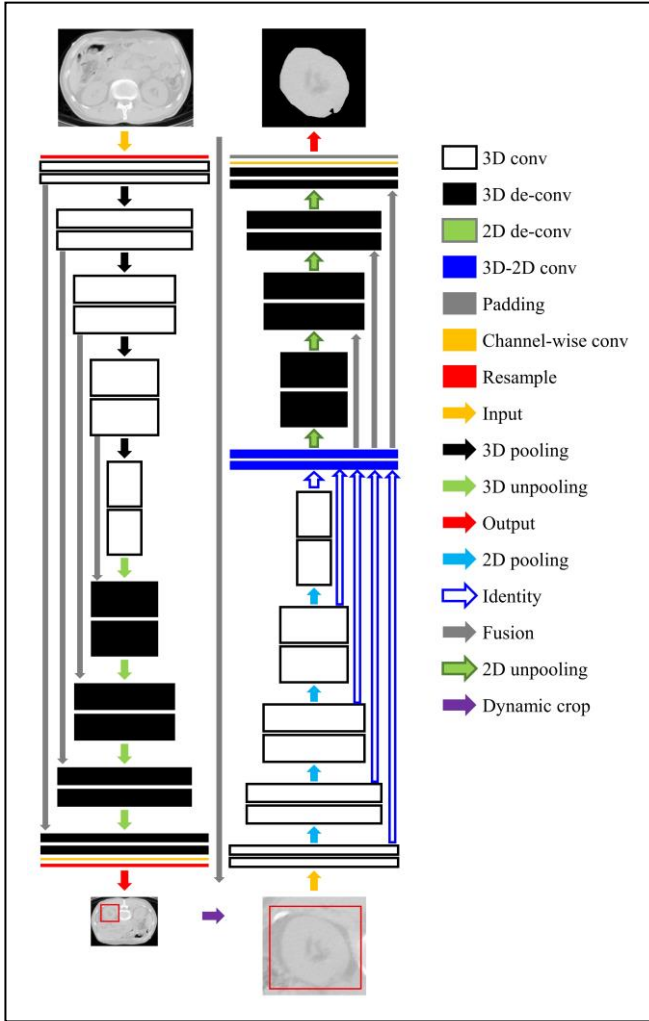


Figure 1. Cascade U-Net[4].

### B. Network Training

We train and test cascade U-Net on thoracic and abdominal CT data. The thoracic CT data were downloaded from the AAPM 2017 Thoracic Organ Segmentation Competition, which consists of 36 sets of CT data for training and 12 sets of CT data for testing. These CT data were labeled with four organs (left lung, right lung, heart, esophagus, spinal cord) by the game organizer. In addition, we get 40 sets of

abdominal CT data from the department of nuclear medicine, the General Hospital of People's Liberation Army and these CT data were labeled by a skilled radiologist with three organs (spleen, liver, left kidney, right kidney). We randomly take 30 sets of CT data for training and 10 sets of CT data for testing. All experiments are performed on a computer with Intel Xeon Gold 6150 CPU and GTX 1080ti GPU. Using Adam as the optimizer, the learning rate is 0.0001, the batch size is 1, the training is 200 epochs, and the training duration is 50 hours. The loss function uses the cross-entropy of the network prediction label and the real label.

### C. Application in Dosimetry for Nuclear Medicine

The patient specific phantoms developed above are applied in dose estimation of Radiation therapy. The SPECT/CT hybrid machine combines SPECT (single-photon emission computed tomography) with CT (computed tomography) to provide hybrid imaging. In this work the Geant4 toolkit is applied to simulate the process of particle interactions to calculate the dose distribution. SPECT images provide decay counts in each voxel. The calibration curve given by pre-experiment can be used to convert the decay count to radioactivity. So that the activity distribution obtained from SPECT imaging serves as the source item. The energy deposited in different sites of interaction is analyzed to estimate the absorbed dose-rate distribution.

## III. RESULT

### A. Testing Result of Cascade U-Net

Using the trained network to segment the CT data, it takes about 3 minutes to segment the 80 slices chest CT image for four organs, and it takes about 2.5 minutes to segment the 80 slices abdominal CT image for three organs. This proves the effectiveness and feasibility of applying this method to phantom construction. The test results on the test set are shown in the following table.

TABLE I. TEST RESULT OF CASCADE U-NET

Testing data set	Organ	Dice coefficient
Thoracic CT data	Heart	0.703
	Lungs	0.892
	Spinal	0.791
	Esophagus	0.823
Abdominal CT data	Spleen	0.724
	Liver	0.713
	Kidneys	0.779

### B. Application in Dosimetry

The absorbed organ dose-rate of individual patient was calculated based on the patient specific phantoms. And the results were compared with the dose estimation with phantoms which were obtained through manual organ segmentation.

#### IV. CONCLUSION

In our study, we validated the effectiveness of segmenting CT data for patient-specific phantoms using a deep learning neural network approach. We deem that the future of patient-specific phantoms modeling will be closely combined with deep learning or neural network[10]. The excellent performance of neural networks in image segmentation will also lead to a new revolution in patient-specific phantoms modeling methods. The application of patient specific phantoms in dose estimation for nuclear medicine can improve the accuracy of individual dose calculation. It can greatly promote the development of precision medicine. In the future we will further improve our dataset, label more organs and collect more nuclear medicine data, enabling our network to segment more organs at once.

#### ACKNOWLEDGMENT

This work was supported by the National Natural Science Foundation of China [Grant No. 11875036].

#### REFERENCES

- [1] Xu X G. An exponential growth of computational phantom research in radiation protection, imaging, and radiotherapy: a review of the fifty-year history.[J]. *Physics in Medicine & Biology*, 2014, 59(18):233-302.
- [2] Stabin M G, Sparks R B, Crowe E. OLINDA/EXM: The Second-Generation Personal Computer Software for Internal Dose Assessment in Nuclear Medicine[J]. *Journal of Nuclear Medicine Official Publication Society of Nuclear Medicine*, 2005, 46(6):1023.
- [3] Xie T, Akhavanallaf A, Zaidi H. Construction of patient - specific computational models for organ dose estimation in radiological imaging[J]. *Medical Physics*. 2019,46(5):2403-2411.
- [4] Gosselin M C, Neufeld E, Moser H, et al. Development of a new generation of high-resolution anatomical models for medical device evaluation: the Virtual Population 3.0[J]. *Physics in Medicine and Biology*, 2014, 59(18):5287-5303.
- [5] Johnson P, Lee C, Johnson K, et al. The influence of patient size on dose conversion coefficients: a hybrid phantom study for adult cardiac catheterization[J]. *Physics in Medicine and Biology*, 2009, 54(12):3613-3629.
- [6] Na Y H , Zhang B , Zhang J , et al. Deformable adult human phantoms for radiation protection dosimetry: anthropometric data representing size distributions of adult worker populations and software algorithms[J]. *Physics in Medicine and Biology*, 2010, 55(13):3789-3811.
- [7] Segars W P, Bond J, Frush J , et al. Population of anatomically variable 4D XCAT adult phantoms for imaging research and optimization[J]. *Medical Physics*, 2013, 40(4):043701.
- [8] Lloyd B, Cherubini E, Farcito S , et al. *Covering Population Variability: Morphing of Computation Anatomical Models[M]// Simulation and Synthesis in Medical Imaging*. Springer International Publishing, 2016.
- [9] Wang C, Macgillivray T, Macnaught G, et al. A two-stage 3D Unet framework for multi-class segmentation on full resolution cardiac data[J]. 2018.
- [10] Lecun Y, Bengio Y, Hinton G. Deep learning[J]. *Nature*, 2015, 521(7553):436.

# Scientific Session

Tuesday, 23 July 2019

<b>11:20 – 13:00</b>	<b>Scientific Session “Dosimetry I”</b> <b>Chair: Chan H. Kim, Co-Chair: David Broggio</b>
11:20	Organ segmentation using machine learning and phantoms atlas for patient-specific CT organ dosimetry Zhao Peng, Xi Fang, Hongmin Shan, Pinkun Yan, Ge Wang, Bob Liu, Mannu Kalra, and <u>X. George Xu</u>
11:40	CT organ dose intercomparison between ICRP and USTC phantoms Shijie Fang, Yifei Pi, Tianyu Liu, Zhi Chen, and <u>X. George Xu</u>
12:00	Assessment of uncertainties associated with Monte Carlo simulation of clinical CT examinations Azadeh Akhavanallaf, Tianwu Xie, and Habib Zaidi
12:20	Establishment of mesh-type detailed breast model and applications in dose estimation Ankang Hu, Rui Qiu, Li Ren, Wenlan Li, Zhen Wu, Chunyan Li, Hui Zhang, Junli Li
12:40	Monte Carlo calculation of age-dependent calibration factors for in-vivo monitoring of $^{131}\text{I}$ in thyroid J.M. Gómez-Ros, V. Berkovsky, D. Broggio, D. Gregoratto, P. Lombardo, M. Moraleda, G. Ratia, M.A. Saizu, P. Teles, K. Tymińska

# Organ Segmentation Using Machine Learning and Phantoms Atlas for Patient-Specific CT Organ Dosimetry

Zhao Peng<sup>1,2</sup>, Xi Fang<sup>1</sup>, Hongmin Shan<sup>1</sup>, Pinkun Yan<sup>1</sup>, Ge Wang<sup>1</sup>, Bob Liu<sup>3</sup>, Mannu Kalra<sup>3</sup>, and X. George Xu<sup>1,2\*</sup>,

<sup>1</sup>\*Rensselaer Polytechnic Institute, Troy, New York, USA

<sup>2</sup>University of Science and Technology of China, Hefei, China

<sup>3</sup>Massachusetts General Hospital, Boston, Massachusetts, USA

\*Corresponding author: xug2@rpi.edu

**Abstract**—Organ doses to patients undergoing CT examinations are needed for purposes of radiation risk assessment and procedure/equipment comparison. This paper demonstrates the feasibility of automatic multi-organ segmentation using latest machine learning methods involving novel convolutional neural network (CNN) models, followed by dose calculations using GPU-based ARCHER Monte Carlo code that can compute in real-time. Training data include a large phantom library and pre-segmented CT image datasets. Results suggest the feasibility of selected CNN models for the proposed tasks.

**Index Terms**—CT; organ dose; segmentation; Monte Carlo; machine learning (5 maximum)

## I. INTRODUCTION

In the United States, the number of diagnostic x-ray CT examinations had increased 20 folds between 1980s and 2010s, owing to rapidly improving multi-detector CT (MDCT) technologies [1-3]. CT is replacing conventional radiography as the initial diagnostic exam in emergency rooms and CT scanners are also integrated with modalities in nuclear medicine (PET/CT) as well as in image-guided radiotherapy where a patient can receive multiple scans [4]. The American College of Radiology (ACR) urgently calls for more effective methods to evaluate and manage such imaging doses [1], citing that existing dose computational tools were insufficient for patient-specific dose quantification, scanner optimization, and protocol comparison.

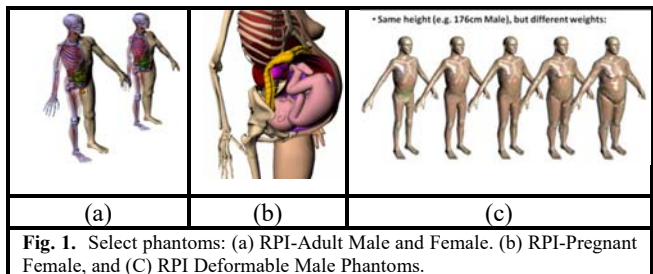
Today, CT scanners are required to supply “Size Specific Dose Estimated (SSDE)” that are not based in patient-specific anatomical and organ dose information [5]. The most advanced organ dose assessment methods rely on off-line software, such as VirtualDose [6], to re-construct patient organ doses using pre-calculated data from a population-averaged anatomical phantoms [7] for risk assessment and procedure/equipment comparison. With recently developed fast Monte Carlo dose computing code, such as ARCHER [8], organ doses can be derived in almost real time if organs can be segmented from patient-specific CT images.

This paper presents a patient-specific CT organ dose assessment method that first performs segmentation of multiple organs from patient-specific CT scans using phantom-based atlas and convolutional neural network (CNN) [9], followed by Monte Carlo-based real-time dose calculations.

## II. METHODS

### Phantoms

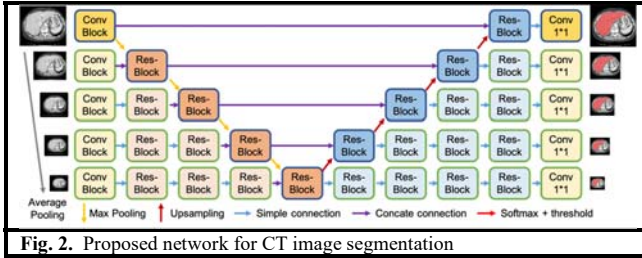
Whole-body computational phantoms are the most common research tool for Monte Carlo based organ dose calculations. Most of the existing computational phantoms can be divided into three categories: stylized phantoms, voxel phantoms and boundary representation (BREP) phantoms [7]. Compared with the other two types of phantoms, BREP phantoms have attractive flexibility and anatomical realism. In this work we use a library of previously developed phantoms, as shown in Figure 1, including RPI-Pregnant Female (3-, 6-, and 9-month gestational period) [10], RPI-Adult Male and Female [11], RPI-Obese Phantoms (representing patients of different weights from normal to overweight and to morbidly obese) [12], as well as USTC Family Phantoms of various ages [13].



### Convolutional neural network (CNN)

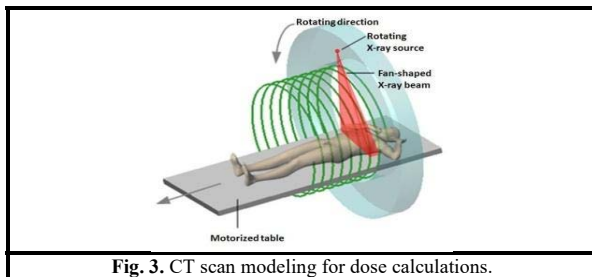
We design a novel method using deep convolutional neural network (CNN) to combine features from multiple views and multiple scales for CT image segmentation based on our

previous work [9]. The proposed network gradually fuses features from images in different scales with hierarchical receptive fields. To build very deep network efficiently with 19 layers, 2D convolutional operations are employed. 3D CT volumes are then segmented separately in three views, i.e. axial, sagittal and coronal, and the results are fused together to achieve the final segmentation. The structure of the designed CNN is shown in Fig. 2.



### Dose Calculations

ARCHER code simulates the transport of low-energy (1~140keV) photons in heterogeneous media where photoelectric effect, Compton scattering and Rayleigh scattering may take place. ARCHER is designed to interface with an extensive library of voxelized phantoms developed from previous research [8]. Besides, ARCHER contains a built-in, validated scanner model based on a GE LightSpeed third-generation 16-multi-detector CT. A series of scan protocols are predefined, including a combination of scan mode (helical or axial), beam collimation (5, 10, or 20 mm) and kVp (80, 100, 120 or 140). Fig. 3 demonstrates one of the simulation cases in which a patient receives a helical CT scan.



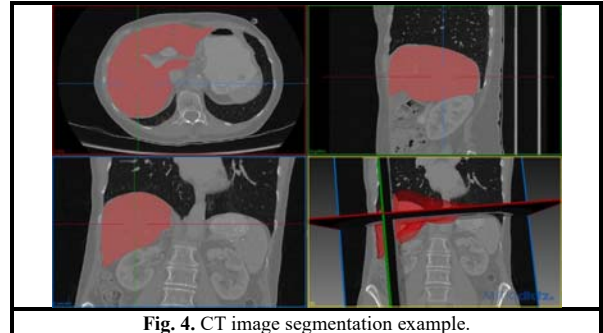
Using the newly segmented patient-specific CT image dataset, a new phantom is constructed and used for ARCHER to calculate organ doses. Results from such calculations are compared against organ doses from population-average phantoms to show the discrepancies in using such phantoms to estimate patient-specific organ doses. Timing performance of the GPU-based ARCHER calculations are also analyzed.

### III. RESULTS

An example of liver CT image automatic segmentation result is shown in Fig. 4.

### IV. CONCLUSION

Convolutional neural network (CNN) models trained with the phantom library and pre-segmented CT image datasets such as those investigated in this study allow organs of interested to be segmented accurately and efficiently for the purposes of calculating organ doses for patients who have received CT examinations.



### ACKNOWLEDGMENT

VirtualDose and ARCHER were developed with NIH grants (R01EB015478, R42EB010404, R42EB019265-01A1).

### REFERENCES

- [1] E.S. Amis, P.F. Butler, K.E. Applegate, S.B. Birnbaum, L.F. Brateman, J.M. Hevezi, F.A. Mettler, R.L. Morin, M.J. Pentecost, G.G. Smith, K.J. Strauss, and R.K. Zeman, "American College of Radiology white paper on radiation dose in medicine." J Am Coll Radiol. 4:272-284,2007.
- [2] de Berrington, and S. Darb, "Risk of cancer from diagnostic x-rays: estimates for the UK and 14 other countries." Lancet 363:345-51. 2004.
- [3] D.J. Brenner and E.J. Hall, "Computed Tomography - An increasing source of radiation exposure." N Engl J Med. 357:2277-84. 2007.
- [4] A. Ding, J. Gu, X.G. Xu, A.V. Trofimov, "Monte Carlo calculation of imaging doses from diagnostic multi-detector CT and kilovoltage cone beam CT as part of prostate cancer treatment plans." Med Phys. 37(12): 6199-6204, 2010.
- [5] American Association of Physicists in Medicine Task Group 204. "Size-specific dose estimates (SSDE) in pediatric and adult body CT examinations". Report of AAPM Task Group 204. College Park, MD: American Association of Physicists in Medicine; 2011.
- [6] A. Ding, Y. Gao, H. Liu, P.F. Caracappa, D.J. Long, W.E. Bolch, B. Liu, X.G. Xu, "VirtualDose: a software for reporting organ doses from CT for adult and pediatric patients" Phys Med Biol. 60(14):5601-25. 2015.
- [7] X.G. Xu, "An exponential growth of computational phantom research in radiation protection, imaging, and radiotherapy: a review of the fifty-year history," Phys Med Biol. 59:R233-R302, 2014.
- [8] Xu XG, Liu T. Real-time Monte Carlo simulation methods: concept and feasibility. ANS RPSD 2018-20th Topical Meeting of the Radiation Protection & Shielding Division of ANS Santa Fe, NM, August 26-31, 2018
- [9] Q. Zhu, B. Du, B. Turkbey, P. L. Choyke, and P. Yan, "Deeply-supervised CNN for prostate segmentation," in International Joint Conference on Neural Networks (IJCNN), 2017, pp. 178-184.
- [10] Xu XG, Taranenko V\*, Zhang J\*, Shi\* C. A boundary-representation method for designing whole-body radiation dosimetry models: pregnant females representing three gestational periods RPI-P3, -P6 and -P9. Phys. Med. Biol. 52: 7023-7044, 2007
- [11] J. Zhang, Y.H. Na, P.F. Caracappa, and X.G. Xu, "RPI-AM and RPI-AF, a pair of mesh-based, size-adjustable adult male and female computational phantoms using ICRP-89 parameters and their

calculations for organ doses from monoenergetic photon beams,”  
*Phys Med Biol.* 54:5885-5908, 2009.

[12] A. Ding, M.M. Mille, T. Liu., P.F. Caracappa, and X.G. Xu,  
“Extension of RPI-adult male and female computational phantoms to

obese patients and a Monte Carlo study of the effect on CT imaging  
dose,” *Phys Med Biol.* 57:2441-2459, 2012.

[13] Pi Y, Liu T, Xu XG. Development of a set of mesh-based and age-  
dependent Chinese phantoms and application for CT dose  
calculations. *Radiat Prot Dosimetry*, 179(4):370-382 (2018).

# CT organ dose intercomparison between ICRP and USTC phantoms

Shijie Fang<sup>1</sup>, Yifei Pi<sup>1</sup>, Tianyu Liu<sup>2</sup>, Zhi Chen<sup>1</sup> and X. George Xu<sup>1,2,\*</sup>

<sup>1,\*</sup>. School of Nuclear Science and Technology, University of Science and Technology of China, Hefei, Anhui Province 230026, PR China

<sup>2</sup>. Nuclear Engineering Program, Rensselaer Polytechnic Institute, Troy, NY 12180, USA

\*Corresponding author: xgxu@ustc.edu.cn

**Abstract**—Computational phantoms are essential in estimating organ doses under various irradiation conditions. However most existing phantoms were designed to match internal and external anatomical structure of the Reference Man as defined by the International Commission on Radiological Protection (ICRP). To reduce errors in anatomical structure between different races and uncertainty in dose calculations caused by anatomical variations, we introduce the USTC phantoms conforming to Chinese characteristics. This paper presents implementation of ICRP phantoms and comparison of CT organ dose values from ICRP phantoms and USTC phantoms using Monte Carlo simulations. Results indicate differences in dose values due to mainly the size and anatomical details of ICRP phantoms and USTC phantoms.

**Index Terms**—phantoms; organ dose; Monte Carlo simulation.

## I. INTRODUCTION

Phantoms for organ dose calculations are essential in radiation protection dosimetry. This article describes the comparison of CT organ dose values from Monte Carlo simulation results using ICRP phantoms and USTC phantoms. The ICRP phantoms are based on the International Commission on Radiological Protection (ICRP) Publication 110 reference male/female phantoms [1]. The USTC phantoms, as shown in Figure 1 (a), are a set of mesh-based and age-dependent phantoms for Chinese populations using reference data recommended by the Chinese government and by the International Atomic Energy Agency (IAEA) [2,3]. All of these phantoms were then converted to the voxel format for Monte Carlo simulations in MCNP [4]. Organ dose coefficients for adult models were derived to compare with those of both ICRP adult male, ICRP adult female and USTC-AM, USTC-AF.

## II. SIMULATIONS

For CT dose calculations in this study, only the photon transport functions in the MCNP code was enabled. Photoelectric effect, Compton scattering and Rayleigh scattering were explicitly simulated. The energy of secondary electrons was assumed to be deposited in the local voxels. The Woodcock tracking method was used to efficiently track particles in a voxel phantom [4]. It is reasonably effective and precise for the photon energy <140 keV applied in most X-ray CT scanners.

The MC simulation includes 27 organs, 'Bone Endosteum', 'Brain', 'Breast', 'Colon', 'Esophagus', 'Gonads', 'Liver', 'Lungs',

'Red Bone Marrow', 'Salivary Glands', 'Skin', 'Stomach', 'Thyroid', 'Urinary Bladder', 'Adrenals', 'ET Region', 'Gall Bladder', 'Heart', 'Kidneys', 'Lymphatic Nodes', 'Muscle', 'Oral Mucosa', 'Pancreas', 'Small Intestine', 'Spleen', 'Thymus', 'Uterus(F)/Prostate(M)'.

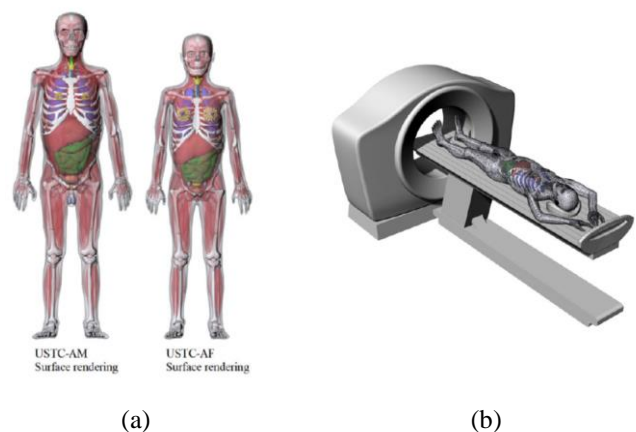


Figure 1. Phantoms and The Monte Carlo dose simulation: (a) Surface rendering pictures of USTC phantoms. (b) CT scanner model and USTC adult male phantom.

In this project, we used the GE LightSpeed Pro 16 multi-detector CT (MDCT) scanner model as shown in Figure 1 (b). The CT scanner model developed using MCNP in our previous studies is parameterized and fully validated [5,6]. CT scans were simulated with 120 kVp and 100 mAs, 20mm collimation width and one pitch. Scan ranges were manually measured from voxel phantoms and summarized from AAPM CT protocols [7].

## III. CONCLUSION

In this project, CT organ dose comparison is utilized by implementation of ICRP and USTC phantoms in MCNP. By comparing organ dose data under the same CT scan parameters, we found difference between ICRP phantom and USTC phantom. These the derived CT organ dose comparisons are helpful to match the difference of Chinese clinical CT organ dose and data from ICRP phantoms. Such Chinese-specific phantoms are better suited for organ dose studies for the Chinese individuals.

#### ACKNOWLEDGMENT

Linli Mao, Yaping Qi and Wanli Huo in University of Science and Technology of China (USTC) assisted with the revision and submission of this article. The Center of Radiological Medical Physics (CRMP) in USTC supplied the high-performance simulation server.

#### REFERENCES

- [1] ICRP, 2009 ICRP. Adult Reference Computational Phantoms. ICRP Publication 110 Ann. ICRP, 39 (2) (2009), pp. 29-118.
- [2] Kawamura, H., Tanaka, G.-i., Shiraiishi, K., Honda, Y., Nishimuta, M., Koyanagi, T., Karim, F., Molla, M., Rab, A. and Wang, J. Compilation of anatomical, physiological and metabolic characteristics for a Reference Asian Man-IAEA-TECDOC-1005. J. Radiat. Res. (Tokyo) 39(4), 350 (1998).
- [3] Tanaka, G., Kawamura, H., Griffith, R. V., Cristy, M. and Eckerman, K. F. Reference man models for males and females of six age groups of Asian populations. Radiat. Prot. Dosim. 79(1-4), 383-386 (1998).
- [4] Pelowitz, D. B. MCNPX User's Manual Version 2.5.0. Los Alamos National Laboratory. 76 (2005).
- [5] Ding, A., Gao, Y., Liu, H., Caracappa, P. F., Long, D. J., Bolch, W. E., Liu, B. and Xu, X. G. VirtualDose: a software for reporting organ doses from CT for adult and pediatric patients. Phys. Med. Biol. 60(14), 5601 (2015).
- [6] Ding, A., Gu, J., Trofimov, A. V. and Xu, X. G. Monte Carlo calculation of imaging doses from diagnostic multidetector CT and kilovoltage cone-beam CT as part of prostate cancer treatment plans. Med. Phys. 37(12), 6199-6204 (2010).
- [7] American Association of Physicists in Medicine. AAPM CT Scan Protocols—The Alliance for Quality Computed Tomography (2017). Available on <http://www.aapm.org/pubs/CTProtocols/>.

# Assessment of uncertainties associated with Monte Carlo simulation of clinical CT examinations

Azadeh Akhavanallaf<sup>1</sup>, Tianwu Xie<sup>1</sup>, Habib Zaidi<sup>1,2,3,4\*</sup>

<sup>1</sup>Division of Nuclear Medicine and Molecular Imaging, Geneva University Hospital, CH-1211 Geneva 4, Switzerland

<sup>2</sup>Geneva University Neurocenter, Geneva University, CH-1205 Geneva, Switzerland

<sup>3</sup>Department of Nuclear Medicine and Molecular Imaging, University of Groningen, 9700 RB Groningen, Netherlands

<sup>4</sup>Department of Nuclear Medicine, University of Southern Denmark, 500 Odense, Denmark

\*Corresponding author: Habib.Zaidi@hcuge.ch

**Abstract**— Monte Carlo simulations-based estimation of organ level radiation dose from diagnostic imaging procedures using patient-specific models is commonly considered the gold standard for the implementation of a reliable framework that can be adopted in clinical setting. The main purpose of this work is to analyze the uncertainties of the estimated organ doses as the parameters used as input to the simulation are obtained from limited DICOM CT image information in comparison with accurate values derived from CT raw data files. We investigated the dosimetric impact of modeling tube current modulation schemes (complete vs. longitudinal only) and tube start angle position implemented in a validated dose tracking Monte Carlo code. Data of an anthropomorphic physical phantom examined using an abdominal helical CT scan was employed. The absolute mean difference between organ-level doses resulting from accurate raw data-based simulation and approximate image-based simulation corresponding to one rotation in the abdominal region is about 6.92% where this difference for the gallbladder exceeds 19%.

**Index Terms**— CT dosimetry, Monte Carlo simulations; computational phantoms; modeling

## I. INTRODUCTION

Monte Carlo simulations are commonly considered as reference (gold standard) for dose estimation in Computed Tomography (CT) imaging. The accuracy of input parameters related to the geometry of the imaging system and the data acquisition protocol has substantial impact on the accuracy of results [1]. The input parameters could be

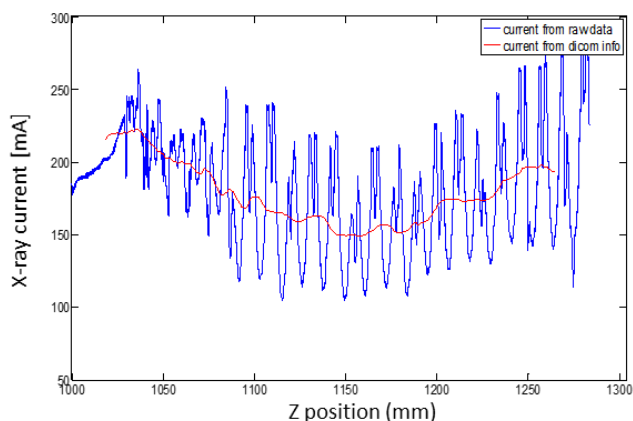


Figure 2. Tube current modulation in routine abdominal helical CT scan.

extracted from CT raw data, which are commonly saved in proprietary format not easily accessible to CT scientists or simply obtained from DICOM information derived from CT images. In this work, we examined the impact of input parameters on the accuracy of organ level doses from a routine abdominal helical CT scan of a physical phantom.

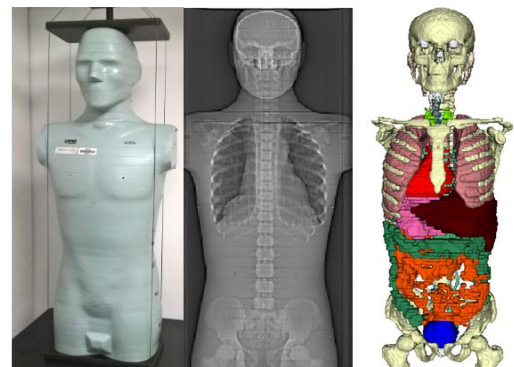


Figure 1. Physical and computational ATOM phantom.

## II. METHODS

### A. Construction of the computational phantom

We used the ATOM adult anthropomorphic phantom (Computerized Imaging Reference Systems, Inc, Norfolk, VA) for a routine abdominal helical CT scan. The ICRP adult male computational phantom was employed as an anchor model to be registered to the ATOM phantom CT images using a 3-D deformable registration algorithm for the construction of a whole-body voxel model with well-defined anatomical structures. Image registration was performed using a previously developed algorithm based on the Insight Toolkit (ITK, <https://itk.org>) [2]. As shown in Figure 1, the registered voxel phantom was used as input for MCNPX-based Monte Carlo calculations of CT radiation dose.

### B. Monte Carlo simulations

Computational models are commonly coupled with Monte Carlo simulations for dosimetry calculations through full simulation of the CT scanner and input parameters used by the scanning protocol. This study was acquired on the GE 750HD CT scanner (GE Healthcare, Waukesha, WI). The geometry of the system was accurately modeled and validated against experimental measurements as described in previous work [3]. The acquisition parameters, including the

revolution time, pitch factor, total collimation width, table speed, tube voltage and modulated tube current and tube start angle extracted from two sources of information: CT raw data files and image DICOM headers. Using CT raw data, we extracted the simulation input parameters for 2305 source point positions per rotation. Using DICOM information, we accessed the data for each slice keeping in mind that the accuracy of the input data depends on the slice thickness. The angular and longitudinal tube current modulation (TCM) profiles were obtained from CT raw data. Only the longitudinal TCM of each slice is accessible from the DICOM header file of CT images. Furthermore, the tube start angle, an important factor in simulations is only available from the CT raw data. Therefore, organ level absorbed doses and effective dose were calculated using a previously validated C++ computer code [3].

### III. RESULTS

The complete TCM obtained from CT raw data is illustrated in Figure 2 where the longitudinal TCM extracted from the DICOM information corresponding to the average movement of the complete TCM per rotation is mapped on it. In raw data-based simulation framework, 2305 point source positions per rotation with complete TCM was modeled where the tube start angle was extracted from raw data. In the image-based framework, the number of simulation point positions was determined based on the slice thickness where the tube start angle was modeled in four different arbitrary angles with  $90^\circ$  differences. The average of four different tube start angles is used for dosimetry calculations. The simulated absorbed dose per particle in one rotation is illustrated in Figure 3. A 4% error results from ignoring the complete TCM. The absolute mean difference between organ-level doses resulting from raw data-based and image-based simulations for one rotation in the abdominal region is about 6.92%, while this difference for the gallbladder exceeds 19%. Organ absorbed doses and effective dose are shown in Figure 4.

### IV. CONCLUSION

We investigated the dosimetric impact of complete TCM and tube start angle modeling in MC simulation-based CT dosimetry. The methodology can be further expanded to produce an accurate MC simulation with a reduced computational burden.

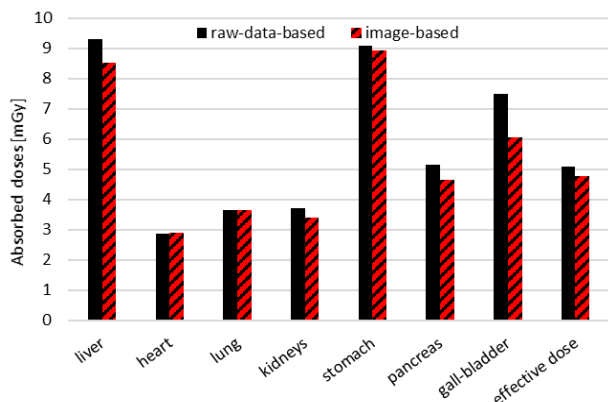


Figure 4. Comparison of absorbed organ doses and effective dose derived from raw data- and image-based simulations.

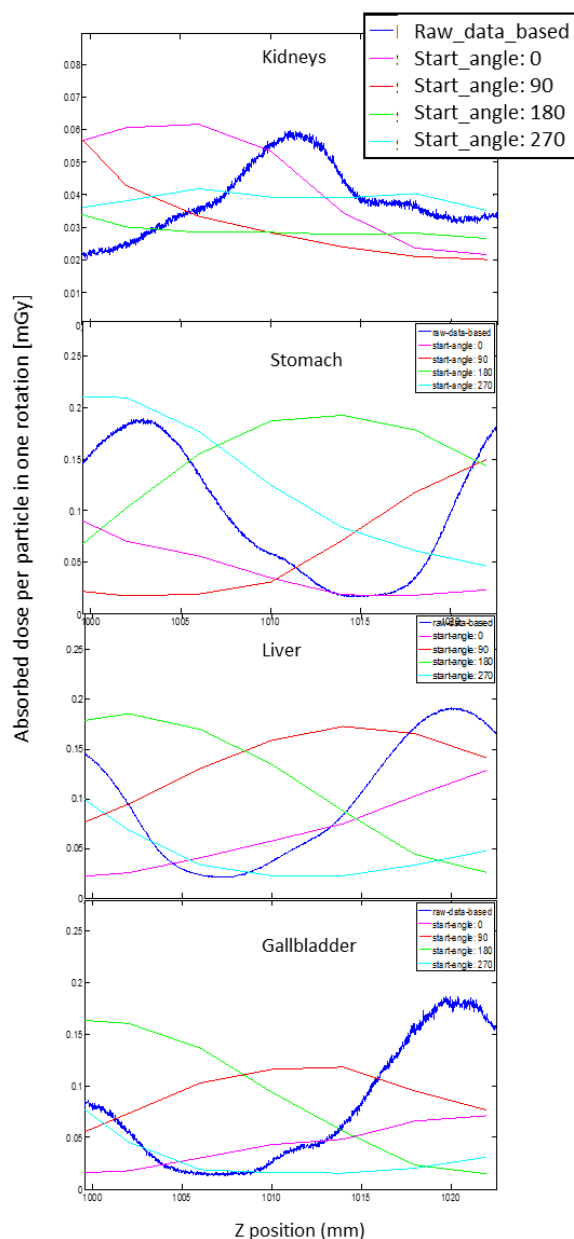


Figure 3. Simulated dose per particle in one rotation for the kidneys, stomach, liver, and gallbladder.

### ACKNOWLEDGMENT

This work was supported by the Swiss National Science Foundation under grant SNSF 320030\_176052 and Iran's Ministry of Science and Technology.

### REFERENCES

- [1] J. S. Muryn, A. G. Morgan, C. L. Liptak, F. F. Dong, W. P. Segars, A. N. Primak, *et al.*, "Analysis of uncertainties in Monte Carlo simulated organ and effective dose in chest CT: scanner- and scan-related factors.," *Phys Med Biol*, vol. 62, pp. 3175-3203, 2017.
- [2] T. Xie, A. Akhavanallaf, and H. Zaidi, "Construction of patient-specific computational models for organ dose estimation in radiological imaging.," *Med Phys*, in press, 2019.
- [3] T. Xie, P. A. Poletti, A. Platon, C. D. Becker, and H. Zaidi, "Assessment of CT dose to the fetus and pregnant female patient using patient-specific computational models.," *Eur Radiol*, vol. 28, pp. 1054-1065, 2018.

# Establishment of Mesh-type Detailed Breast Model and Applications in Dose Estimation

Ankang Hu<sup>1,2</sup>, Rui Qiu<sup>1,2,\*</sup>, Li Ren<sup>1,2</sup>, Wenlan Li<sup>1,2</sup>, Zhen Wu<sup>1,3</sup>, Chunyan Li<sup>1,3</sup>, Hui Zhang<sup>1,2</sup>, Junli Li<sup>1,2</sup>

<sup>1</sup> Department of Engineering Physics, Tsinghua University, Beijing, China

<sup>2</sup> Key Laboratory of Particle & Radiation Imaging, Tsinghua University, Ministry of Education, Beijing, China

<sup>3</sup> Joint Institute of Tsinghua University and Nuctech Company Limited, Beijing, China

\*Corresponding author: qiurui@mail.tsinghua.edu.cn

**Abstract**—This work established a series of mesh-type detailed breast models and combined them with the mesh-type Chinese reference adult female phantom (CRAF). These breast models contain skin, subcutaneous fat, Cooper's ligaments, fibroglandular region, and so on. CRAF's breast shape is deformed to generate 5 mesh-type adult female phantoms with cup sizes ranging from AA to D standards. Besides, the glandularity of phantom with B cup size was changed to generate several phantoms to study the effect of glandularity. As these phantoms have finer anatomical structure in breast and could be deformed flexibly, they provide an advanced tool for dose estimation. CRAF with detailed breast model were used in dose estimation for standard condition exposure and medical exposure. Monte Carlo simulation was performed by using this series of phantoms to calculate dose conversion coefficients of breast gland for photon external exposures in standard irradiation geometries. And for medical exposure, dose conversion coefficients of digital breast tomosynthesis were calculated.

**Index Terms**—*mesh-type detailed breast model; Monte Carlo; external exposure; digital breast tomosynthesis*

## I. INTRODUCTION

The female breast is one of the most sensitive organs to radiation. International Commission on Radiological Protection (ICRP) has changed the recommended tissue weighting factors for breast tissue from 0.05 to 0.12. At the same time, the frequency of medical exposure in Chinese women is increasing year by year, which made the accurate evaluation of breast dose more important.

Female breasts have complex structures. Different kinds of breast tissue differ greatly in elemental composition, density and radiosensitivity. But the most of existing phantoms can't describe the detailed structure of breast limited by the resolution image resolution of CT, MRI or color cryosection. Detailed mathematical breast models and voxel models have been developed for accurate dose estimation. But the mathematical model is not easy to assemble it to a whole body phantom. The voxel models can hardly be deformed. The mesh-type model makes it possible to construct deformable detailed breast models and combine them with a whole-body phantom.

For radiation protection, dose conversion coefficients of external exposure in standard irradiation geometries are widely

used for dose estimation. More accurate data considering size and glandularity of breast provides better reference for female occupational exposure dose estimation.

Digital breast tomosynthesis (DBT) is a new method to improve the accuracy of breast diagnosis and reduce the dose. In order to avoid the shortcoming of mammography from tissue overlapping, DBT adopts the image reconstruction algorithm to get the 3-D images of breast in field of view (FOV) by obtaining several 2-D images in different projection angles. But more projection angles may lead higher dose, which needs to be estimated accurately.

This work established a series of mesh-type detailed breast models considering different breast sizes and glandularity. All these models are combined with CRAF to calculate dose conversion coefficients for photon external exposure. And dose of digital breast tomosynthesis is estimated using these models. These deformable and detailed breast model provide tool for breast dose estimation.

## II. METHODS

### A. Chinese reference adult female phantom

Mesh-type Chinese reference adult female phantom established by Tsinghua University is consist of 63 organs. The breast of the CRAF model is only divided into three parts: skin, subcutaneous fat and breast gland limited by the resolution of image modeling the phantom.

### B. Mesh-type detailed model in Chinese reference adult female phantom

The detailed model contains skin, subcutaneous fat, Cooper's ligaments, fibroglandular region, and so on. They were modeled using polygon-mesh surfaces.

The shape of CRAF's breast was deformed to match different cup sizes to generate a series of phantoms based on Chinese bra sizing standard. And breast gland of B cup size phantom was adjusted to constructed phantoms with different glandularity.

### C. Monte Carlo simulation in extern radiation

Dose conversion coefficients of breast gland for external photon exposures in antero-posterior geometry are calculated

to compare the phantoms with different breast sizes and different glandularity.

#### D. Digital breast tomosynthesis dose estimation

Digital breast tomosynthesis system was modeled. Then simulation was performed using phantoms with detailed breast models. Dose conversion coefficient of each projection angle was calculated.

### III. RESULTS

#### A. Mesh-type detailed breast model

The mesh-type detailed breast model constructed this work and phantom with it are shown in figure 1. And phantoms with different breast size are shown in figure 2.

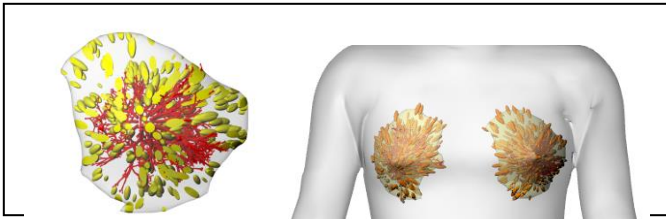


Figure 1. mesh-type detailed breast model and phantom with detailed breast model

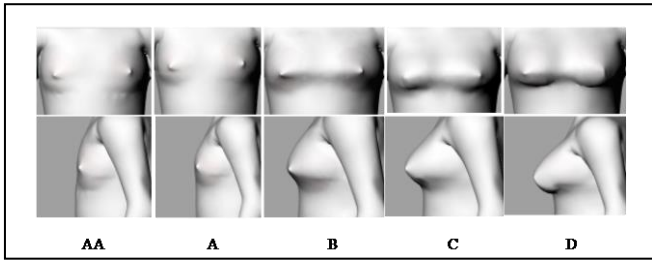


Figure 2. Front view and side view of phantoms with different breast sizes

#### B. Dose conversion coefficients of photon external exposure in standard irradiation geometries

Dose conversion coefficients of photon external exposure in six standard irradiation geometries were calculated using phantoms with different breast parameters. Results of B cup size phantom for different exposure geometry is shown in figure 2 as an example.

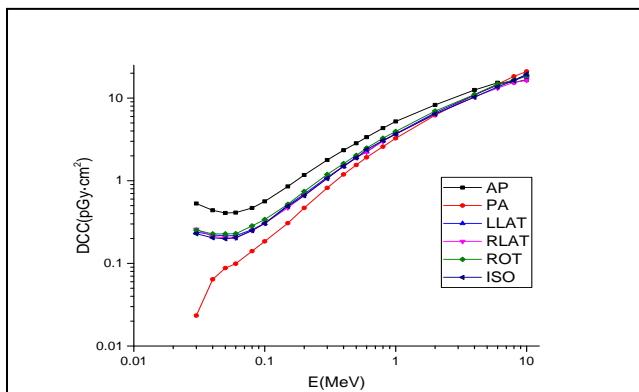


Figure 3. Dose conversion coefficients of B phantom for different exposure geometry

#### C. Dose estimation for digital breast tomosynthesis

The phantom with detailed breast model and the model of Siemens Mammomat Inspiration System were used to simulation. The voltage of X-ray tube is 25kV with W/Rh combination. Dose factors of each projection angle are listed in table 1.

TABLE I. DOSE FACTOR OF EACH PROJECTION ANGLE

Projection Angle [° ]	Dose Factor
1	1.005
3	1.019
5	0.990
7	0.986
9	0.978
11	0.957
13	0.948
15	0.939
17	0.903
19	0.893
21	0.822
23	0.800
25	0.828

### IV. CONCLUSION

This study develops a method of establishing mesh-type organ model with complex structure and a feasible technique of deformation to change the shape of complex structure smoothly. A series of Chinese adult female phantoms with different breast sizes and different glandularity were established by deforming CRAF. Monte Carlo simulations using these phantoms were performed to calculate the dose conversion coefficients of breast gland for photon external exposures in six standard irradiation geometries. And dose estimation of digital breast tomosynthesis was performed. These deformable mesh-type detailed breast model can better represent the finer anatomical structure and provide an advanced tool for dose estimation.

### ACKNOWLEDGMENT

This work was supported by the National Natural Science Foundation of China [Grant No. 11875036].

### REFERENCES

- [1] Rui, Qiu, et al. "Establishment of the Detailed Breast Model of Chinese Adult Female and Application in External Radiation Protection." Radiation Protection Dosimetry (2016).
- [2] Hoeschen, C., Fill, U., Zankl, M. et al. "A highresolutionvoxel phantom of the breast for dose calculationsin mammography," Radiat. Prot. Dosimetry 114(1-3), 406-409 (2005).
- [3] Hegenbart, L, et al. "A Monte Carlo study of lung counting efficiency for female workers of different breast sizes using deformable phantoms." Physics in Medicine & Biology 53.19(2008):5527-38.
- [4] T. Han et al., "Simulation of mammograms and tomosynthesis imaging with cone beam breast CT images," Proc. SPIE 6913, 17.1-17.7 (2008).
- [5] Wang, Wenjing, et al. "Monte Carlo calculation of conversion coefficients for dose estimation in mammography based on a 3D detailed breast model." Medical Physics, 44(6): 2503-2514 (2017)

# Monte Carlo calculation of age-dependent calibration factors for in-vivo monitoring of $^{131}\text{I}$ in thyroid

J.M. Gómez-Ros<sup>1,\*</sup>, V. Berkovsky<sup>2</sup>, D. Broggio<sup>3</sup>, D. Gregoratto<sup>4</sup>, P. Lombardo<sup>5</sup>, M. Moraleda<sup>1</sup>, G. Ratia<sup>2</sup>, M.A. Saizu<sup>6</sup>, P. Teles<sup>7</sup>, K. Tymińska<sup>8</sup>

<sup>1,\*</sup> CIEMAT, Av. Complutense 40, 28040 Madrid, Spain

<sup>2</sup> RPI, Melnikova 53, 04050 Kyiv, Ukraine

<sup>3</sup> IRSN, P.O Box 17, 92262 Fontenay-aux-Roses, France-mail address if desired

<sup>4</sup> PHE-CRCE, Harwell Campus, OX11 0RQ Didcot, United Kingdom

<sup>5</sup> SCK•CEN, Boeretang 200, 2400 Mol, Belgium

<sup>6</sup> IFIN-HH, Strada Reactorului 30, 077125 Bucharest - Magurele, Romania

<sup>7</sup> C2TN, Instituto Superior Técnico, Universidade de Lisboa, Estrada Nacional 10 (km 139.7) 2695-066 Bobadela, Portugal

<sup>8</sup> NCBJ, Andrzej Soltana 7, 05400 Otwock, Poland

\*Corresponding author: email jm.gomezros@ciemat.es

**Abstract**—This work summarizes the results of Monte Carlo simulations for several detectors and voxel phantoms representing different age groups that have been performed to investigate the variation of the detection efficiency with distance, age and thyroid volume. Age-dependent correction factors to be applied to the adult calibration factor have been derived and can be used when calibration factors for children are not available. Moreover, the influence of elapsed time since intake has been investigated taking into account the iodine biokinetics.

**Index Terms**— $I-131$ ; iodine; radioiodine; thyroid

## I. INTRODUCTION

Radioactive iodine is of particular radiological interest among fission products, which can be released into the environment in case of an accident at a nuclear power reactor. The resulting source term can include a variety of chemical and physical forms of radioactive isotopes of iodine. From these,  $^{131}\text{I}$  is the main subject of radiological monitoring as it plays a dominating role in the thyroid exposure.

The measurement of radioactive iodine in the thyroid gland is commonly carried out by in-vivo measurements using gamma spectrometers which need to be calibrated with reference sources and anthropomorphic phantoms including a thyroid gland simulator. This work summarizes the results of the exhaustive Monte Carlo simulation study performed in the framework of the CATHYMARARA project (Child and Adult Thyroid Monitoring After Reactor Accident) within OPERRA project number 604984. One of the project objectives was to obtain age dependent calibration factors for in-vivo monitoring of  $^{131}\text{I}$  for different ages, namely 1-, 5-, 10- and 15-year-old children and adult and to assess the influence of geometrical and anatomical parameters on the detection efficiency. An indicative estimation of the potential contribution of the extrathyroidal  $^{131}\text{I}$  to the reading of collimated and non-collimated detector used for measurements of the  $^{131}\text{I}$  activity content in the thyroid gland is also provided.

## II. METHODS

### A. Detectors

Four spectrometric detectors currently used in four research laboratories were used in this study: a Low Energy Germanium (Ge) detector [1] and three Sodium-Iodide (NaI) detectors of different crystal sizes [2-4]. Among them, one of the NaI detectors included a collimator.

### B. Voxel phantoms

Seven human voxel phantoms: two for adults (male and female) and five for 1-, 5-, 10- and 15-years-old (male and female) children have been built modifying the four anthropomorphic phantoms developed at the HMGU: Babynew, Child, Golem and Laura [5]. Their voxel dimensions were scaled to obtain new phantoms according to the ICRP reference values for thyroid volume and body height [6]. The z-dimension was scaled to fit the body height. The x- and y dimensions were scaled to get the adequate thyroid volume [7].

## III. SIMULATIONS

The detector response was calculated using the Monte Carlo code MCNPX 2.7 [8]. The pulse height tally 'F8 was used to score the pulse height spectra from the detector per emitted particle. The detection efficiency is the ratio between the net count rate and the source activity in the peak of 364.5 keV, the main photon emission in the decay of  $^{131}\text{I}$ .

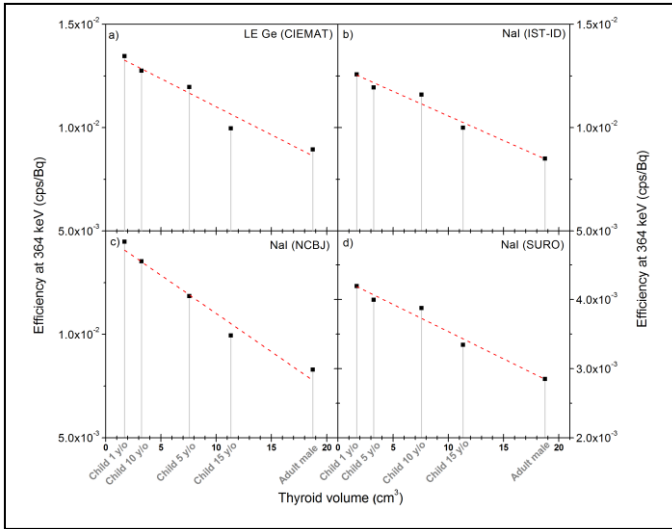
### A. Detection efficiency as a function of age

The correction factors for different age and distance values together with the detection efficiency for adults have been calculated. The differences in detection efficiency between the 5 years old and the adult phantom are between 40 % at 5 cm and 30 % at 17.5 cm.

## B. Detection efficiency as a function of thyroid volume

The thyroid mass in the phantoms varies from 1.8 to 20 g depending on age and gender. Moreover, efficiency is also affected by the thickness of the thyroid overlying tissue. Therefore, the distance has been measured from the thyroid volume centre to the front surface of the crystal in the detector. The calculated efficiencies for a given value of such a distance show a nearly linear dependence with the thyroid volume (correlation coefficient greater than 0.95), as shown in Figure 1.

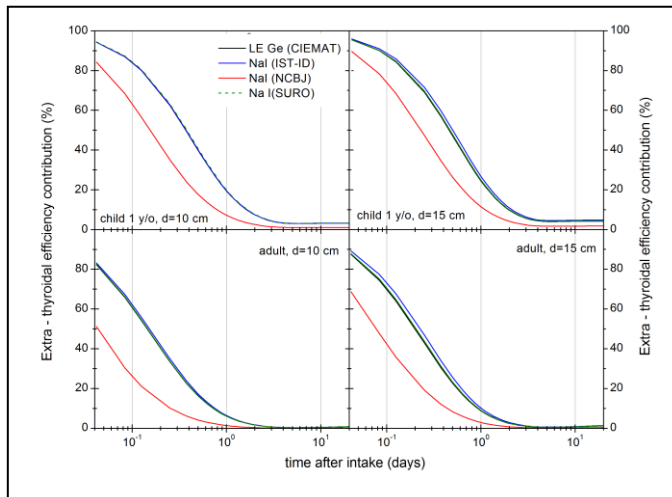
Figure 1. Detection efficiency as a function of thyroid volume for the four considered detectors.



## C. Extra-thyroidal contribution

The contribution of extra-thyroidal  $^{131}\text{I}$  has been obtained by MC simulation of the detection efficiency with  $^{131}\text{I}$  distributed either only in thyroid or in the rest of the body of the voxel phantoms. These values have been combined with the calculated activity ratios between thyroid/rest of the body being considered an acute inhalation of soluble radioactive aerosols (ICRP Type of Material F) with the activity median aerodynamic diameter (AMAD) of  $1\ \mu\text{m}$  [9].

Figure 2. Extra-thyroidal contribution as a function of the elapsed time after inhalation for two age voxel phantoms and two distances neck to detector.



In case of collimated detector (red lines in Figure 2), a delay in the measurement of one day is sufficient to minimize the contribution of extrathyroidal  $^{131}\text{I}$  for all ages. For uncollimated detectors, such a delay should also be sufficient for the adult (6%), but two days would ensure better results for 1- and 5-year-old children (8% - 4% respectively).

## IV. CONCLUSION

The dependence of efficiency versus distance, age and thyroid volume can be used to make adjustments when such information is available. Age-adjusted detection efficiencies is especially relevant for children, for whom the detection should be as accurate as possible, given their higher radiosensitivity.

Based on this study, a two steps procedure can be recommended in case of accidental intake of  $^{131}\text{I}$ : i) short time screening measurements at the closest possible neck-to-detector distance to identify contaminated individuals; ii) more accurate measurements in case of a positive result: longer counting time and larger distance compatible with the detector efficiency to reduce uncertainties due to age as well as variations in thyroid size and overlying tissue thickness. Waiting one or two days to reduce the extra thyroidal contribution is advisable.

## ACKNOWLEDGMENT

This work has been developed within the CATHYMAR project (Child and Adult Thyroid Monitoring After Reactor Accident), funded by the 7th EU framework programme, under the OPERRA Call.

## REFERENCES

- [1] J.M. Gómez-Ros et al. Monte Carlo modelling of Germanium detectors for the measurement of low energy photons in internal dosimetry: results of an international comparison. *Radiat. Meas.* 43, 510–515, 2008.
- [2] T. Beaumont, P. Caldeira-Ideias, M. Rimlinger, D. Broggio, D. Franck. Development and test of sets of 3D printed age-specific thyroid phantoms for  $^{131}\text{I}$  measurements. *Phys. Med. Biol.* 62, 4673–4693, 2017.
- [3] M. Szuchta, J. Oško. Numerical model of thyroid counter. *Nukleonika* 61, 45–47, 2016.
- [4] T. Vrba, P. Fojtik. The design of a NaI(Tl) crystal in a system optimised for high-throughput and emergency measurement of iodine 131 in the human thyroid. *Radiat. Phys. Chemistry* 104, 385–388, 2014.
- [5] N. Petoussi-Hens, M. Zankl, U. Fill, D. Regulla. The GSF family of voxel phantoms. *Phys. Med. Biol.* 47, 89–106, 2002.
- [6] ICRP Publication 89: Basic anatomical and physiological data for use in radiological protection: Reference values. *Ann. ICRP* 32 (3–4), 2002
- [7] P. Teles, M. Mendes, M. Zankl, V. de Sousa, A.I. Santos, P. Vaz. Assessment of the absorbed dose in the kidney of nuclear nephrology paediatric patients using ICRP biokinetic data and Monte Carlo simulations with mass-scaled paediatric voxel phantoms. *Radiat. Prot. Dosim.* 174, 121–135, 2017.
- [8] D.B. Pelowitz (editor), 2011. MCNPX User's Manual Version 2.7. Report LA-CP-11-00438.
- [9] V. Berkovski, G. Ratia, Y. Bonchuk. IMIE computer codes: 10 years in the dosimetry. *Radiat. Prot. Dosim.* 125, 205 – 208, 2007.

# Scientific Session

Wednesday, 24 July 2019

9:00 – 10:00	<b>Scientific Session “Dosimetry II”</b> <b>Chair: Choonsik Lee, Co-Chair: X. George Xu</b>
9:00	Construction of 3D organ dose maps for medical staff exposed to scattered radiation in fluoroscopically-guided interventional procedures: a feasibility study Choonsik Lee, <u>Inseok Baek</u> , David Borrego, Mark Salasky, Daniel J. Valentino
9:20	An algorithm for voxel to mesh phantom conversion with applications to radiation therapy Justin Brown, Takuya Furuta, and Wesley E. Bolch
9:40	Interactive Posture Program: a software for controlling the Realistic Anthropomorphic Flexible phantom Pasquale Alessandro Lombardo, Mahmoud Abdelrahman, Filip Vanhavere, and Lara Struelens

# Construction of 3D organ dose maps for medical staff exposed to scattered radiation in fluoroscopically-guided interventional procedures: a feasibility study

Choonsik Lee<sup>1,\*</sup>, Inseok Baek<sup>2</sup>, David Borrego<sup>1</sup>, Mark Salasky<sup>2</sup>, Daniel J. Valentino<sup>2</sup>

<sup>1</sup>Division of Cancer Epidemiology and Genetics, National Cancer Institute, National Institutes of Health, Rockville, USA

<sup>2</sup>Fluke Health Solutions, Landauer Science & Technology Innovation Center, Chicago, IL, USA

\*Corresponding author: choonsik.lee@nih.gov

**Abstract**—The goal of the present study is to evaluate the feasibility to create 3D phase-space files of radiation scattered from a patient and 3D map of organ doses for a medical staff undergoing Fluoroscopically-Guided Interventional Procedures (FGIPs). X ray from a generic fluoroscopy C-arm was simulated in a general-purpose Monte Carlo code, MCNPX2.7, along with two computational human phantoms representing a physician standing next to the right knee of the patient lying on the bed. Organ doses per air kerma (Gy/Gy) were calculated for five different fluoroscopy beam angles. The staff organ doses were compared with the measurement data published by other researchers, where dose rate was measured on a physical phantom using real time dosimeters. We confirmed that the simulated staff organ doses showed the similar angular dependency to the measurement data. Based on the feasibility tested in the current study, future efforts will focus on the extension of the organ dose maps by simulating more comprehensive beam geometry, patient size, procedure types, and staff locations.

**Index Terms**—computational human phantoms; staff dose; fluoroscopy; Monte Carlo radiation transport

## I. INTRODUCTION

During Fluoroscopically-Guided Interventional Procedures (FGIPs), medical staffs are primarily exposed to scattered radiation from the patient. There are particular concerns about doses and potential cancer risks in medical staffs involved in FGIPs [1], [2]. Accurate estimation of organ doses for physicians and radiologic technologists is crucial for robust risk analysis. However, most of the existing dosimetry studies focus on the characterization of x ray beams and dosimeter measurements surrounding C-arms which cannot be directly used for the analysis of cancer risks. In the current study, we tested the feasibility to generate 3D phase-space files of scattered radiation emanating from the patient and to create a comprehensive organ dose map for medical staff performing FGIPs. The results were then compared with the measurement data published by other researchers.

## II. METHODS

### A. Computational human phantoms

We adopted an adult male computational phantom [3] developed by the University of Florida and the National Cancer Institute to represent the anatomy of an adult patient lying on the fluoroscopy bed and a radiological staff standing next to the patient. The adult male phantom was developed from computed

tomography images through manually segmenting organs and tissues and adjusting their volumes to match the International Commission on Radiological Protection (ICRP) reference data [4]. The phantom is 176 cm in height and 73 kg in weight. More than 140 organs and tissues are defined including cortical and spongiosa bones for accurate active bone marrow dosimetry.

### B. Monte Carlo radiation transport simulations

We simulated a FGIP where an adult male patient is lying on the bed while a medical staff is standing next to the right knee of the patient (about 128 cm from the top of the patient's head). The staff location is common for cardiac catheterization procedures (Figure 1). The x ray source was located 86 cm from the isocenter, the patient's heart, and the source-to-image receptor distance (SID) was set to 100 cm. The field-of-view was collimated to produce a circular image of about 25cm diameter at the image receptor. We used an x ray spectra of 60 kVp to match half-value layer specification in the standard radiation quality series number 4 (RQR) [5].

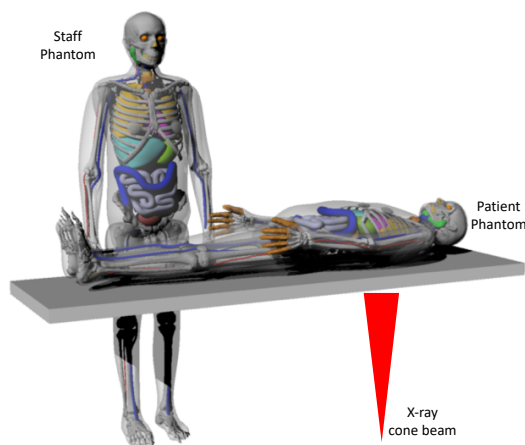


Figure 1. 3D rendering of the simulation geometry where an adult male medical staff is standing next to the right knee of an adult male patient lying on the bed.

Our simulation was conducted in two steps. First, we created phase-space files for scattered x rays from the patient phantom as shown in Figure 2. We scored the energy and angle of photons entering a cylinder (40 cm diameter) surrounding the adult patient phantom by using the Surface-Source-Write (SSW) feature in MCNPX2.7. Phase-space files were generated for five positioner primary angles ranging from -90 (left lateral beam), -

45 (right anterior oblique), 0 (antero-posterior beam), 45 (left anterior oblique), and 90 (right lateral beam) degree. Each phase-space file was created using  $10^8$  photon particle histories. Second, we simulated the medical staff phantom standing next to the phase space cylinder (Figure 1). We rotated and shifted the cylindrical phase spaces created from the previous step to the typical staff-patient geometry. We calculated major organ absorbed doses (Gy) of the patient phantom and measured air kerma (Gy) in the x ray beam path, which were then used to derive organ dose conversion coefficients (Gy/Gy).

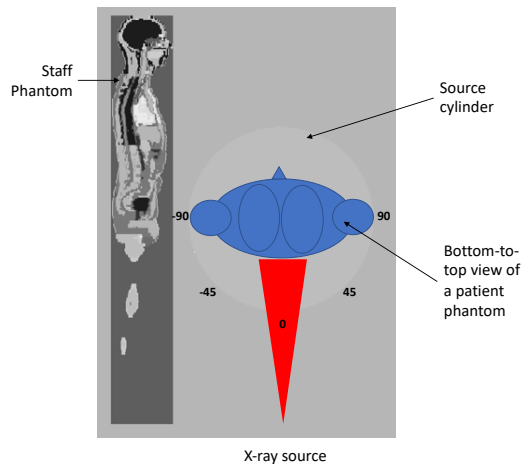


Figure 2. Cross-sectional view of the medical staff phantom with the patient phantom for five X-ray beam angles (-90 to 90 degree) around the patient.

### III. RESULTS AND DISCUSSION

#### A. Phase space files for scattered radiation

From the simulation Step 1, we created five phase space files for scattered radiations surrounding the patient phantom. File size of a single phase-space about 1GB contained the energy and angle of radiation scattered from the patient phantom. These files would make it simple to conduct the simulation Step 2 by adjusting the location and size of the staff phantom.

#### B. Staff organ dose maps

Organ dose conversion coefficients (Gy/Gy) for the adult male medical staff phantom are tabulated in Table I for five different x ray beam angles. Air kerma measurements (Gy) are generally available from C-arm console, which can be multiplied to the organ doses per air kerma to obtain organ absorbed doses. Figure 3 shows the ratio of dose conversion coefficients for major organs and different beam angles to that for the reference angle (0 degree). A peak dose to the staff phantom is observed in left anterior oblique geometry, which is consistent with the measurement data published by Rehn *et al.* [6]

### I. CONCLUSION

We conducted a feasibility study to create 3D organ dose maps for medical staffs undergoing FGIP. Future efforts will focus on the extension of the organ dose maps by simulating more comprehensive beam geometry, patient size, procedure types, and staff locations.

Table I. Major organ doses per air kerma (Gy/Gy) for a medical staff standing beside the patient bed undergoing FGIP.

Staff Organs	Positioner Primary Angle (degree)				
	-90	-45	0	45	90
Brain	3.93E-08	3.96E-08	3.89E-08	4.10E-08	3.86E-08
Lens	1.61E-07	1.61E-07	1.61E-07	1.61E-07	1.61E-07
Thyroid	4.14E-07	4.24E-07	4.08E-07	5.23E-07	5.41E-07
Esophagus	4.56E-08	5.29E-08	4.47E-08	5.18E-08	4.15E-08
Lung	1.44E-07	1.46E-07	1.41E-07	1.46E-07	1.39E-07
Breast	9.21E-07	9.30E-07	9.71E-07	9.47E-07	9.42E-07
Heart W	1.52E-07	1.57E-07	1.57E-07	1.55E-07	1.46E-07
Stomach W	2.82E-07	2.80E-07	2.71E-07	2.82E-07	2.67E-07
Liver	8.94E-08	7.92E-08	8.68E-08	8.24E-08	8.47E-08
Kidney	5.30E-08	5.19E-08	5.07E-08	5.49E-08	5.07E-08
Small Intestine Wall	2.64E-07	2.59E-07	2.69E-07	2.79E-07	2.56E-07
Colon Wall	5.71E-07	5.52E-07	5.51E-07	5.99E-07	5.57E-07
Urinary bladder Wall	2.30E-07	2.36E-07	2.23E-07	2.45E-07	2.24E-07
Testes	2.36E-06	2.32E-06	2.34E-06	2.50E-06	2.31E-06
Skin	2.05E-06	2.04E-06	2.05E-06	2.07E-06	2.01E-06

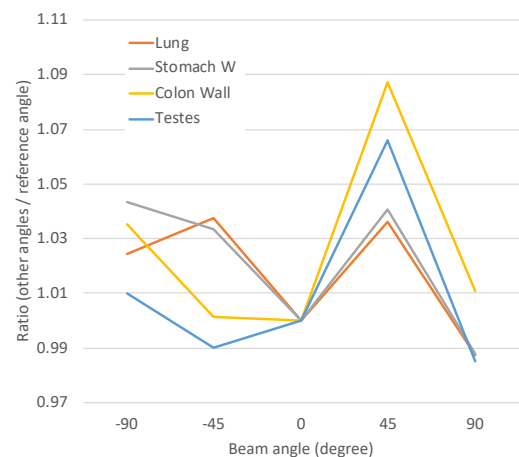


Figure 3. Ratio of organ dose conversion coefficients for beam angles to those for the reference angle (0 degree).

### ACKNOWLEDGMENT

This research was funded by the intramural research program of the National Institutes of Health (NIH), National Cancer Institute, Division of Cancer Epidemiology and Genetics.

### REFERENCES

- [1] C. M. Stahl, Q. C. Meisinger, M. P. Andre, T. B. Kinney, and I. G. Newton, "Radiation Risk to the Fluoroscopy Operator and Staff," *Am. J. Roentgenol.*, vol. 207, no. 4, pp. 737–744, Sep. 2016.
- [2] S. Ko *et al.*, "Health Effects from Occupational Radiation Exposure among Fluoroscopy-Guided Interventional Medical Workers: A Systematic Review," *J. Vasc. Interv. Radiol. JVIR*, vol. 29, no. 3, pp. 353–366, 2018.
- [3] C. Lee, D. Lodwick, J. Hurtado, D. Pafundi, J. L. Williams, and W. E. Bolch, "The UF family of reference hybrid phantoms for computational radiation dosimetry.," *Phys. Med. Biol.*, vol. 55, no. 2, pp. 339–363, Jan. 2010.
- [4] ICRP, "Adult Reference Computational Phantoms," *ICRP Publ. 110 Ann ICRP*, vol. 39, no. 2, pp. 1–166, Jan. 2009.
- [5] IAEA, "Dosimetry in Diagnostic Radiology: An International Code of Practice," Text Technical Report 457, 2007.
- [6] E. Rehn, "Modeling of scatter radiation during interventional X-ray procedures," Linkoping University, Linkoping, Sweden, 2015.

# An Algorithm For Voxel to Mesh Phantom Conversion With Applications to Radiation Therapy

Justin Brown<sup>1</sup>, Takuya Furuta<sup>2</sup>, and Wesley E. Bolch<sup>3</sup>\*

<sup>1</sup>\*Medical Physics Graduate Program, College of Medicine, University of Florida, Gainesville, Florida, USA

<sup>2</sup> Nuclear Science and Engineering Centre, Japan Atomic Energy Agency, Ibaraki, Japan

<sup>3</sup>. J. Crayton Pruitt Family of Biomedical Engineering, University of Florida, Gainesville, FL USA

\*Corresponding author: wbolch@ufl.edu

**Abstract**—The coupling of computation phantoms with Monte Carlo codes has been commonplace for over 20 years. However, only recently has radiation transport via polygon or tetrahedral meshes been possible. Both voxel and mesh phantoms allow for a realistic representation of human anatomy. Mesh type phantoms allow for articulation and inclusion of thin tissue layers of radiobiological importance; this is generally not possible in a voxel phantom. The present work describes an efficient and robust algorithm to convert voxel-based data to polygon mesh format suitable for radiation transport. This work also describes a workflow for implementing this algorithm into the clinic allowing Monte Carlo external beam treatment planning to be performed by converting segmented patient CT images to polygon meshes for radiation transport. This conversion results in a significant speedup over those using voxelized models in radiation transport.

**Index Terms**—Voxel Phantom, Mesh Phantom, Conversion Algorithm, Radiation Therapy, Treatment Planning

## I. INTRODUCTION

Beginning in the early 2000's human computational mesh phantoms became widely used. These mesh-type phantoms allowed for the scalability and deformability provided by stylized phantoms, yet they retained the anatomical realism of voxel phantoms. Within the past several years many advanced have been made in particle tracking and localization algorithms allowing direct use of mesh geometries on Monte Carlo (MC) radiation transport. These developments were initially introduced into the MCNP code in 2009 [1], into the GEANT4 code in 2013 [2], and into the PHITS code in 2015 [3][4]. This work implements an algorithm developed to convert voxel phantoms or segmented patient images to a polygon mesh phantom suitable for MC radiation transport. This method eliminates all geometric redundancies from the voxel data, allowing for an optimized and minimalistic representation of the tissue structures. This process is highly beneficial for computational human phantoms as voxel size is governed by the smallest anatomical structure to be represented and in patient images is determined by the reconstruction protocol used. The current algorithm allows both segmented patient images and voxel phantoms to be utilized in MC transport codes.

## II. METHODS

The voxel to mesh conversion algorithm can be divided into 5 mesh generation steps and 1 post processing steps: (1) data preparation, (2) gridded surface generation, (3) surface simplification, (4) line simplification, (5) polygon detection, and polygon correction and hole detection (6) post processing

### A. Data Preparation

Prior to meshing the voxelized data, it is first read into a 3D array of specified size  $\langle n_x, n_y, n_z \rangle$ . Then, additional four-dimensional arrays are created of dimensions  $\langle n_x, n_y, 3, 12 \rangle$  and  $\langle n_x, n_y, 3, 8 \rangle$  which represent sliding windows of temporary data used to ensure the uniqueness of every facet, vertex, and line that is generated in the newly created mesh phantom. This approach minimizes memory requirements and insures proper particle localization in MC simulations. The array is only 3 units wide as only adjacent voxels can possibly contain information relevant to the current voxel. Several other data arrays are generated to include a vertex array (3D points), a line array (containing two integers representing two connected vertices within the vertex array), a facet array (containing integers representing connected lines within the line array), and a facet tag array (containing the ordered materials which separate the facets)

### B. Gridded Surface Generation

Upon creation of the necessary data arrays, the voxel data is then parsed. Voxels are checked to determine if neighboring voxels are of a different material (or organ) than the current voxel. If a neighboring voxel is found to be of a different material, a facet may be produced. At this step, a facet is simply a rectangle between two voxels of different materials. Facets, vertices, and lines are produced depending on data stored in neighboring voxels. Given neighbors data, the required lines and vertices are determined. Once the required lines and vertices are determined, the sliding window of vertices and lines is checked to determine if this information already exists. If the data already exists, it is added to the current voxel in the sliding data window. If it does not already exist, it is generated and then added to the data window. This process is repeated over the entire voxel array.

### C. Surface Simplification

At this step, a surface mesh has been generated whose boundaries separate the desired organs or segmented structures. These boundaries are represented by a gridded surfaces. To simplify these surfaces they are grouped by three values: (1) separated material, (2) whether or not x, y, or z are constant, and (3) the value of this constant. To simplify, the facets are then merged by performing a Boolean union operation if they satisfy a single criteria: they *must* share a common line. If the two facets indeed share one line, then they may be combined. The Boolean union process involves determining the line in common and then removing the line and combining the facets. This process is repeated until no more facets are found to share lines. The facets marked for removal are then removed.

#### D. Line Simplification

Prior to simplifying the lines of a polygon, they are grouped similarly to the facets. First, lines are scanned iteratively to determine for every vertex how many lines use that vertex. Next, lines are subdivided into co-linear groups. Within each group, lines are checked to determine if they share a common vertex. If the lines share a common vertex, a Boolean union operation can be performed if the vertex in common is only used by two lines globally within the phantom. The Boolean union process is performed for these two lines in a manner similar to that used for the facets. This is repeated within each group until the criteria can no longer be satisfied.

#### E. Polygon Detection, Correction and Hole Detection

Now facets of are comprised of an unordered set of lines and polygons. By construction, the lines contained within each facet must form at least one closed loop (i.e., a polygon). Within each facet, polygons are formed by simply end matching lines until all lines are used. If multiple polygons are formed by construction within one facet, one of these polygons must be interior to the other, thus forming a hole within the outer polygon. This is repeated for each facet.

Once all the necessary polygons are formed it is possible, they may contain self-intersections due to the simple end-matching process used to generate them. To correct this, each polygon is checked to determine if each vertex is used only twice. If the vertex is used more than twice, the polygon contains a self-intersection. To correct, an “ear clipping” method is used. To ear-clip a polygon, one creates a new polygon from the lines between the vertex that is used multiple

times. These lines are then removed from the larger polygon and a new polygon is added to the facet. Once this process is complete, the facet is determined to contain a hole if it contains more than one polygon. A simple bounds check is used to determine which polygons are inside the outmost polygon, and then the inner polygons are labelled as holes.

#### F. Post Processing

At this point, the polygon mesh is composed of facets containing n-gons and holes within these n-gons. To allow use in modern CAD software, these meshes must be triangulated as most software codes do not allow n-gon meshes. To do triangulate this mesh, the Triangle Library [5] is used. This library allows n-gons with holes to be triangulated. Once the triangulation is complete, the mesh is smoothed using a Laplacian smoothing technique with alternating positive and negative weights [6]. This allows for the preservation of mesh volume. To utilize the mesh in MC transport, it can be converted into a tetrahedral mesh as well using Tetgen [7].

### III. BENCHMARKING

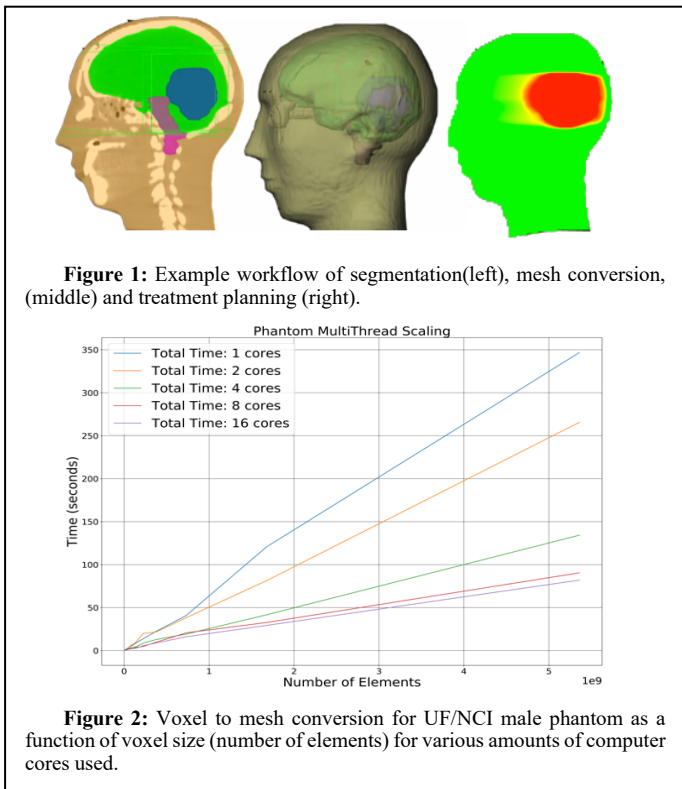
The mesh conversions were applied to the UF/NCI reference adult male phantom at voxel resolutions ranging from  $1 \text{ cm}^3$  to  $1 \text{ mm}^3$  as shown. To assess how this conversion algorithm scales across multiple processors. Thus, the previous two benchmarking studies were performed using 1, 2, 4, 8, and 16 cores, respectively.

### IV. CONCLUSION

The presented methodology converts voxel phantoms or segmented voxelized data into a polygon mesh suitable for CAD modeling and MC transport (**Figure 1**). The conversion process is rapid and capable of scaling a 5-billion element voxel phantom in a few minutes (**Figure 2**).

### REFERENCES

- [1] C. J. Werner *et al.*, “Title: MCNP Version 6.2 Release Notes,” *LA-UR-18-20808*, pp. 1–39, 2018.
- [2] S. Agostinelli *et al.*, “GEANT4 - A simulation toolkit,” *Nucl. Instruments Methods Phys. Res. Sect. A Accel. Spectrometers, Detect. Assoc. Equip.*, vol. 506, no. 3, pp. 250–303, Jul. 2003.
- [3] T. Furuta *et al.*, “Implementation of tetrahedral-mesh geometry in Monte Carlo radiation transport code PHITS,” *Phys. Med. Biol.*, vol. 62, no. 12, pp. 4798–4810, 2017.
- [4] T. Sato *et al.*, “Features of Particle and Heavy Ion Transport code System (PHITS) version 3.02,” *J. Nucl. Sci. Technol.*, vol. 55, no. 6, pp. 684–690, Jun. 2018.
- [5] J. R. Shewchuk, “Triangle: Engineering a 2D quality mesh generator and Delaunay triangulator,” in *Applied Computational Geometry: Towards Geometric Engineering*, Springer, Berlin, Heidelberg, 1996, pp. 203–222.
- [6] G. Taubin, “Curve and surface smoothing without shrinkage,” in *Proceedings of IEEE International Conference on Computer Vision*, pp. 852–857.
- [7] H. Si, “TetGen, a Quality Tetrahedral Mesh Generator,” *AMC Trans. Math. Softw.*, vol. 41, no. 2, p. 11, 2015.



# Interactive Posture Program: a software for controlling the Realistic Anthropomorphic Flexible phantom

Pasquale Alessandro Lombardo<sup>1,\*</sup>, Mahmoud Abdelrahman<sup>1</sup>, Filip Vanhavere<sup>1</sup>, and Lara Struelens<sup>1</sup>

<sup>1,\*</sup> SCK•CEN, Research in Dosimetric Applications, Boeretang 200, 2400 Mol, Belgium

**Abstract**—B-Rep phantoms are characterized by high levels of flexibility and anatomical accuracy. However, they are also very complex to use, as they require advanced knowledge of graphic modeling software. With this work, we aimed to fill this gap by developing the Interactive Posture Program (IPP). Thanks to its interactive graphic interface, IPP allows to make use of all the features of the Realistic Anthropomorphic Flexible (RAF) B-Rep phantom without need of mastering graphic modeling software.

**Index Terms**—computational phantom applications, postural flexibility, voxelization.

## I. INTRODUCTION

In the last decade, the introduction of modeling techniques based on Boundary-Representation (B-Rep) promoted the development of a new generation of Computational Phantoms (CP). B-Rep techniques are characterized by advanced modeling tools making the development of phantoms more flexible compared to that of previous generations. On the one hand, the B-Rep modeling flexibility widened the range of application both in computational dosimetry and in medical imaging, leading to a rapid increase in the number of CPs over the last decades. On the other hand, B-Rep phantoms are very complex to use, as they often require to master advanced graphic modeling tools such as 3Ds Max, Maya or Rhino. These types of software have steep learning curves and non-negligible costs, which compromise the possibility of dissemination of new generation phantoms. Furthermore, the implementation of B-Rep phantoms in simulations is not yet straightforward, as most of deterministic and Monte Carlo particle transport codes do not offer complete support to this type of geometry.

For these reasons, we developed a standalone software for facilitating the use and the dissemination of the Realistic Anthropomorphic Flexible (RAF) B-Rep phantom. This is achieved by means of an interactive graphical interface, named Interactive Posture Program (IPP), which allows to easily set the posture, and change some anthropometric parameters (like height and weight).

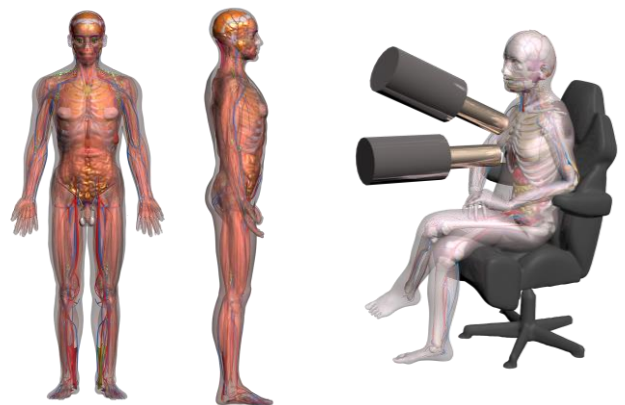
## II. MATERIAL AND METHODS

### A. RAF phantom

The Realistic Anthropomorphic Flexible (RAF) phantom [1] was modeled by means of a particular type of B-Rep, called Polygonal Meshes (PM). The RAF phantom represents an average Caucasian adult male, its anthropomorphic measurements (176 cm, 76 kg) and organ masses are close to those of the ICRP reference adult male [2].

PM modeling was chosen based on the current trend in computer graphics that sees both hardware (GPU) and software evolving towards PM as standard methodology for rendering complex geometries. This allowed to give to the phantom a high level of anatomical accuracy and a realistic postural flexibility, as shown in Figure 1. The postural flexibility of the phantom can be employed in real-time thanks to an animation framework called mathematical skeleton. The RAF phantom is currently being used for applications in computational dosimetry and in medical imaging.

Figure 1. Realistic Anthropomorphic Flexible phantom.



### B. Interactive Posture Program

In its original format, the RAF phantom is compatible only with the 3Ds Max software by Autodesk. 3Ds Max files have a closed file format which is not accessible outside Autodesk SDK environment by means of any publicly available API. For

this reason, the phantom was initially converted to a newly-defined mesh format based on the common \*.obj file format. This new format was designed to host all the meshes (corresponding to the various organs of the phantom) into a single file, while maintaining the same world-space coordinates and floating precision for the vertex positions. Based on this file structure, a series of programs were developed to control specific features and parameters of the RAF phantom. Some of these features have direct effect on the phantom geometry, such as its level of segmentation, its postural deformation (based mostly on forward and inverse kinematic chains) and its dimension. Others are instead dedicated to the visualization and to maintaining the meshes quality when applying deformations.

Due to the increase number of the single programs, they were all incorporated into a single standalone software, named Interactive Posture Program (IPP). IPP handles the RAF phantom geometry, its features and its visualization by means of 3D graphic interface rendered through Direct3D. Figure 2 shows the main interface of IPP. The advantage of this methodology is that besides the RAF phantom, IPP can load any object represented as mesh geometry and make it interact with the phantom. This feature allowed to integrate the geometry of an interventional radiology room, including a C-Arm (with its kinematic), the operating bed and the patient body. For this application, protective garments can be also added to the RAF phantom (apron, thyroid collar and headcap), as shown in figure 3.

Figure 2. Main interface of the Interactive Posture Program.



An export command was developed for exporting the RAF phantom in two formats to be used with Monte Carlo particle transport codes. The first format is compatible with the G4TessellatedSolid class of Geant4 (however, this class presents some limitations in terms of maximum number of polygons). The other file format is a voxelized compressed (lossless) image, following the MetaImage standard \*.mha of itk. The voxelized format is compatible with most of the voxel image visualization tools (like ImageJ), and it can be easily converted to any Monte Carlo voxelized input. The voxelization algorithm, as described in [1], allows to define any voxel resolution. If the total amount of voxels is smaller than 100 million, the algorithm is executed on the GPU. In this case, the speed-up in the conversion is in order of 50 compared to the processing time on CPU. With the default voxelization settings, priority is given to those organs that are considered more relevant for dosimetry in SCK.CEN. However, the

priority can be tweaked by means of a configuration file. Together with the voxelized image of the RAF phantom, IPP prints a text file with a summary of the phantom voxelization data, including the IDs associated to each tissue (figure 4).

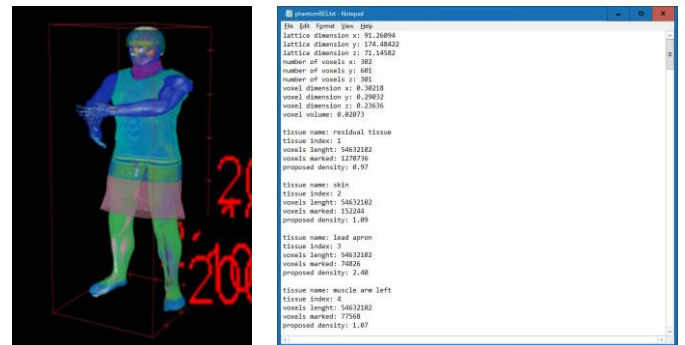
Figure 3. Interventional radiology room geometry within the Interactive Posture Program.



### III. CONCLUSION

Thanks to the introduction of B-Rep modeling, computational phantoms have been evolving dramatically in the last years. However, due to the added complexity, B-Rep phantoms such as the RAF phantom are also less user friendly, making them more difficult to disseminate. The Interactive Posture Program tries to answer to this by providing a user-friendly interface to access all the features of the RAF phantom. Thanks to this software, the RAF phantom can be actively used by anyone to define the input geometry for Monte Carlo simulations.

Figure 4. Voxelized RAF phantom with lattice dimension of 302 x 601 x 301 voxels and resolution of 0.3 x 0.29 x 0.24 cm<sup>3</sup>.



### REFERENCES

- [1] P. A. Lombardo, F. Vanhavere, A. L. Lebacqz, L. Struelens, and R. Bogaerts. "Development and Validation of the Realistic Anthropomorphic Flexible (RAF) Phantom" *Health Phys.*, 114(5), pp 486-499, 2018.
- [2] ICRP, 2009. Adult reference computational phantoms. ICRP Publication ICRP Publication 110, International Commission on Radiological Protection, Oxford, UK. Ann. ICRP 39(2).

# Scientific Session

Wednesday, 24 July 2019

<b>10:00 – 11:00</b>	<b>Scientific Session “Radiation Therapy / Epidemiological Studies”</b> <b>Chair: Rui Qiu, Co-Chair: Chan H. Kim</b>
10:00	Use of mesh-based phantom for organ dose and cancer risks estimations for radiation therapy of unilateral retinoblastoma involving Co-60 unit Suleiman Ameir Suleiman, Yaping Qi, Zhi Chen, and X. George Xu
10:20	Conversion of computational human phantoms into DICOM-RT for normal tissue dose assessment in radiotherapy patients Keith T. Griffin, Matthew M. Mille, Christopher Pelletier, Mahesh Gopalakrishnan, Jae Won Jung, Choonik Lee, John Kalapurakal, Anil Pyakuryal, and <u>Choonsik Lee</u>
10:40	The J45 phantom series and their potential for updates to the atomic bomb survivor organ doses Wesley Bolch, Keith Griffin, Colin Paulbeck, Choonsik Lee, Harry Cullings, Stephen Egbert, Sachiyo Funamoto, Tatsuhiko Sato, Akira Endo, and Nolan Hertel

# Use of Mesh-based Phantom for Organ Dose and Cancer Risks Estimations for Radiation Therapy of Unilateral Retinoblastoma Involving Co-60 Unit

Suleiman Ameir Suleiman<sup>1,2\*</sup>, Yaping Qi<sup>1</sup>, Zhi Chen<sup>1</sup>, and X. George Xu<sup>1,3</sup>

<sup>1</sup>\*School of Physical Sciences, University of Science and Technology of China, Hefei, China

<sup>2</sup>Ionizing Radiation Department, Tanzania Atomic Energy Commission, Arusha, Tanzania

<sup>3</sup>Nuclear Engineering Program, Rensselaer Polytechnic Institute: NES Building, Troy, New York, USA

\*Corresponding author: [njeketu@mail.ustc.edu.cn](mailto:njeketu@mail.ustc.edu.cn)

**Abstract**—The use of Co-60 teletherapy for the treatment of unilateral retinoblastoma (Rb) cancer patient can result in higher secondary exposure to healthy organs. This radiation exposure can cause secondary cancer risks. In this study, a Monte Carlo package MCNPX and set of age dependant computational male phantoms are used to estimate out-of-field organs dose. The estimated doses were used to calculate the secondary cancer risks in out-of-field organ by using the Biological Effects of Ionizing Radiation (BEIR)-VII methodology.

**Index Terms**—Monte Carlo Simulation; Phantom; Unilateral Retinoblastoma; Secondary cancer risk; Co-60 teletherapy;

## I. INTRODUCTION

The risk of radiation-induced secondary cancer after patients with primary cancer undergo radiation treatment has been widely reported by various studies [1,2]. The problem has been known and related studies have been focused to the successful use of new clinical treatment modalities. Several dosimetry research have concluded that the use of new treatment modalities has potential increased out-of-field organ dose and risk of secondary cancer risk [3].

In comparison with the above studies, which are associated to modern treatment devices, this article focuses on traditional technology, the Co-60 teletherapy and cancer disease is known as retinoblastoma (Rb). Rb is the most common malignant eye tumour in young children with estimated rate 1/15000-20000 live births [4]. In many developing countries including Tanzania Rb treated with Co-60 teletherapy.

This study presents organ-specific absorbed doses and the secondary cancer risk calculation to patient with Rb underwent Co-60 teletherapy. The treatment procedures were simulated using the MCNPX Monte Carlo code and a set of advanced computational male phantoms of different ages.

## II. METHODS

### A. Patient Phantoms

A set of mesh-based computational family phantoms were developed at University of Science and Technology in Hefei, China and consisted of the triangular meshes. This set of age-

dependent phantoms include male and female with age of new born, 5-year-old, 10-year-old, 15-year-old and adult. Every phantom comprises more than 100 organs and tissues and all the anatomical parameters were adjusted to agree within 0.5% with the reference people records of China. For the purpose of Monte Carlo methods, mesh-based phantoms were converted to voxel-based formats with a resolution of 0.2cm. The phantoms used in this study resemble an adult male, 10 and 5-year-old which weighed 63, 32 and 19kg. A spherical cell with radius of 1 cm at the precisely location of the retina of the left eye was defined in each phantom used as the tumour target to measure deposited energy at the isocentre.

### B. The Monte Carlo Technique

The Monte Carlo technique is a well-established method as well as the most perfect method to calculate radiation dose for medical physics application. In this study, the MCNPX (Monte Carlo N-Particle eXtended) version 2.7.0 [5] was used for Monte Carlo simulations. The software has been designed at the Los Alamos National Laboratory (LANL) can simulate many types of particles including photons, electrons, neutrons, and heavy ions for complex three-dimensional geometries in a broad range of energies

### C. Secondary cancer incidence risk calculation

The lifetime attributed risk (LAR), which is defined as the probability that an irradiated person will develop a cancer incidence during their lifetime is calculated as follows

$$LAR(D, e) = \int_{e+L}^{a_{max}} \left( ERR \cdot \lambda_1^c \cdot \frac{S(a)}{S(e)} da \right)^{0.7} \times \int_{e+L}^{a_{max}} \left( EAR \cdot \frac{S(a)}{S(e)} da \right)^{0.3}$$

where,  $L$  is the latency period after exposure (for solid tumour is 5 years),  $D$  is dose equivalent,  $e$  is age at treatment in years and  $a$  is the total time since treatment in years,  $\lambda_1^c$  is baseline risk for an exposed individual and  $S(a)/S(e)$  is the possibility of a cancer patient surviving from age  $e$  to age  $a$  founded on the data existing at National Bureau of Statistics in Tanzania.  $\gamma$ ,  $\beta_s$  and  $\eta$  represent the model parameters which are offered for ERR and EAR in the BEIR VII [6].

### III. SIMULATIONS

#### A. Co-60 Teletherapy and beam modelling

The Rb patients were represented by voxelized phantoms which were located at source-to-axial distance of 80cm from the source. A direct anterior of photon beam of 4cm × 4cm field size was used to irradiate isocentre per 40Gy total tumor dose. The MCNPX \*F8 tally was used to record energy deposited in the organs contributed by photons and electrons. All the results were normalized per source history and converted to Gray (Gy). Energy cut-off of 0.01 and 0.5MeV were used for photons and electrons. All simulations were performed on a 24-core Monte Carlo computer server with 2.6GHz RAM and the Ubuntu operating system. It took average time about 9.6 CPU hours for each Monte Carlo simulation to achieve acceptable statistical error of less than 1% for each organ.

#### B. Key Results

Figure 1 shows the comparison of out-of-field absorbed dose in terms of mSv per 40 Gy tumour dose for three unilateral Rb patients of different ages. Table I and 2 shows the comparison of LAR for organs according to the age of exposure using the BEIR VII methodology

### IV. CONCLUSION

In this study, MCNPX Monte Carlo code and a set of computational male phantoms were used to calculate organs absorbed doses of unilateral Rb patients undergo radiotherapy using Co-60 source in Tanzania. The organs doses were used to estimated lifetime attributed cancer risk. Younger patients experienced higher in absorbed doses to out-of-field organs away from the target volume. The secondary cancer risks were

**Table 2.** LAR for organs according to the age of exposure to Co-60 teletherapy (per 100000 population) using the BEIR VII methodology for an adult male

Organ	Age at Exposure (years)			
	35	40	45	50
Stomach	$8.49 \times 10^{-4}$	$8.31 \times 10^{-4}$	$7.32 \times 10^{-4}$	$4.84 \times 10^{-4}$
Colon	$2.97 \times 10^{-4}$	$2.91 \times 10^{-4}$	$2.56 \times 10^{-4}$	$1.69 \times 10^{-4}$
Liver	$5.41 \times 10^{-4}$	$5.29 \times 10^{-4}$	$4.66 \times 10^{-4}$	$3.08 \times 10^{-4}$
Prostate	$2.49 \times 10^{-6}$	$2.43 \times 10^{-6}$	$2.14 \times 10^{-6}$	$1.42 \times 10^{-6}$
Bladder	$1.94 \times 10^{-5}$	$1.90 \times 10^{-5}$	$1.67 \times 10^{-5}$	$1.11 \times 10^{-5}$
Oesophagus	$2.37 \times 10^{-2}$	$3.31 \times 10^{-2}$	$2.04 \times 10^{-2}$	$1.35 \times 10^{-2}$
Kidneys	$1.13 \times 10^{-3}$	$1.10 \times 10^{-3}$	$9.73 \times 10^{-3}$	$6.43 \times 10^{-4}$
Brain	$6.62 \times 10^1$	$6.48 \times 10^1$	$5.71 \times 10^1$	$3.77 \times 10^1$
Lungs	$2.28 \times 10^{-3}$	$2.23 \times 10^{-3}$	$1.97 \times 10^{-3}$	$1.30 \times 10^{-3}$
Thyroid glands	$2.33 \times 10^{-1}$	$1.54 \times 10^{-1}$	$1.02 \times 10^{-1}$	$6.72 \times 10^{-2}$

also calculated and found that organs of younger patients are in higher risks of developing secondary cancer. This is due to organs of younger patients are very close to target volume and are more sensitive to ionizing radiation.

### ACKNOWLEDGMENT

This research was financial supported by the National Key R&D Program of China (Grant No. 2017YFC0107504) and the Natural Science Foundation of China (Grant Nos. 11375182).

### REFERENCES

- [1] S. F. Kry, B. Bednarz, R. M. Howell, L. Dauer, D. Followill, E. Klein, H. Paganetti, B. Wang, C. S. Wu, X. G. Xu, "AAPM TG 158: Measurement and calculations of doses outside the treatment volume from external-beam radiation therapy," *Medical Physics*, vol. 44, pp. e391-429, 2017.
- [2] X. G. Xu, B. Bednarz, H. Paganetti, "A review of dosimetry studies on external-beam radiation treatment with respect to secondary cancer induction," *Physics in Medicine Biology*, vol. 53, pp. 193-241, 2008
- [3] S. D. Sharma, R. R. Upreti, S. Laskar, C. M. Tambe, D. D. Deshpande, S. K. Shrivastava, K. A. Dinshaw, "Estimation of risk of radiation-induced carcinogenesis in adolescents with nasopharyngeal cancer treated using sliding window IMRT," *Radiotherapy Oncology*, vol.86, pp.177-181, 2008.
- [4] P. M. Elmar, S. Wolfgang, H. Thomas, H. Wolfgang, D. Klueter-Reckmann, B. Norbert, S. Horst, F. Michael, H. Wernert, "New and recurrent tumor foci following local treatment as well as external beam radiation in eyes of patients with hereditary retinoblastoma," *Graefes's Archive for Clinical and Experimental Ophthalmology*, vol.228, pp.426-431, 1990.
- [5] Denise B. Pelowitz, 2011. "MCNPX User's Manual Version 2.7.0". LLNL, Los Alamos..
- [6] BEIR. Health Risks From Exposure to Low Levels of Ionizing Radiation: BEIR VII, Phase 2 (Washington, DC: National Academy of Science), 2006.

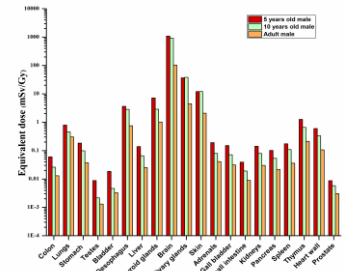


**Figure 1.** Comparison of out-of-field organs absorbed doses in terms of mSv per 40 Gy tumour dose for three unilateral Rb patients of different ages

**Table 1.** Comparison of LAR for organs according to the age of exposure to Co-60 teletherapy (per 100000) population using BEIR VII methodology for 5-year-old, 10-year-old and adult (35-year-old) male

Organ	Age at Exposure (years)		
	5	10	Adult (35)
Stomach	$6.07 \times 10^{-3}$	$2.58 \times 10^{-3}$	$8.49 \times 10^{-4}$
Colon	$2.79 \times 10^{-3}$	$1.14 \times 10^{-3}$	$2.97 \times 10^{-4}$
Liver	$4.04 \times 10^{-3}$	$1.89 \times 10^{-3}$	$5.41 \times 10^{-4}$
Prostate	$2.70 \times 10^{-5}$	$4.35 \times 10^{-6}$	$2.49 \times 10^{-6}$
Bladder	$2.19 \times 10^{-4}$	$8.12 \times 10^{-5}$	$1.94 \times 10^{-5}$
Oesophagus	$1.19 \times 10^{-1}$	$4.92 \times 10^{-2}$	$2.37 \times 10^{-2}$
Kidneys	$8.05 \times 10^{-2}$	$3.32 \times 10^{-3}$	$1.13 \times 10^{-3}$
Brain	$1.35 \times 10^2$	$1.16 \times 10^2$	$6.62 \times 10^1$
Lungs	$3.24 \times 10^{-2}$	$7.00 \times 10^{-3}$	$2.28 \times 10^{-3}$
Thyroid glands	$2.81 \times 10^0$	$1.86 \times 10^0$	$2.33 \times 10^{-1}$

# Conversion of computational human phantoms into DICOM-RT for normal tissue dose assessment in radiotherapy patients

Keith T. Griffin<sup>1</sup>, Matthew M. Mille<sup>1</sup>, Christopher Pelletier<sup>2</sup>, Mahesh Gopalakrishnan<sup>3</sup>, Jae Won Jung<sup>2</sup>, Choonik Lee<sup>4</sup>, John Kalapurakal<sup>3</sup>, Anil Pyakuryal<sup>5</sup>, and Choonsik Lee<sup>1,\*</sup>

<sup>1</sup>Division of Cancer Epidemiology and Genetics, National Cancer Institute, National Institutes of Health, Rockville, MD, USA

<sup>2</sup>Department of Physics, East Carolina University, Greenville, NC, USA

<sup>3</sup>Department of Radiation Oncology, Northwestern Memorial Hospital, Chicago, IL, USA

<sup>4</sup>Department of Radiation Oncology, University of Michigan, Ann Arbor, MI, USA

<sup>5</sup>Division of Science and Mathematics, University of District of Columbia, Washington, DC, USA

\*Corresponding author: choonsik.lee@nih.gov

**Abstract**— Radiotherapy treatment planning systems are designed for the fast calculation of dose to the tumor bed and nearby organs at risk using x-ray computed tomography (CT) images. However, CT images for a patient are typically available for only a small portion of the body, and in some cases, such as for retrospective epidemiological studies, no images may be available at all. When dose to organs that lie out-of-scan must be estimated, a convenient alternative for the unknown patient anatomy is to use a matching whole-body computational phantom as a surrogate. The purpose of the current work is to connect such computational phantoms to commercial radiotherapy treatment planning systems for retrospective organ dose estimation. A custom software with graphical user interface, called the *DICOM-RT Generator*, was developed in MATLAB to convert voxel computational phantoms into the Digital Imaging and Communications in Medicine radiotherapy (DICOM-RT) format, compatible with commercial treatment planning systems. DICOM CT image sets for the phantoms are created via a density-to-Hounsfield unit conversion curve. Accompanying structure sets containing the organ contours are automatically generated by tracing binary masks of user-specified organs on each phantom CT slice. The software was tested on a library of body size-dependent phantoms, taking only a few minutes per conversion. The resulting DICOM-RT files were tested on several commercial treatment planning systems. The converted phantom library, in DICOM format, and a standalone MATLAB-compiled executable of the *DICOM-RT Generator* are available for others to use for research purposes (<http://ncidose.cancer.gov>).

**Index Terms**—*DICOM, automatic contouring, voxel phantom, retrospective dose, phantom library*

## I. INTRODUCTION

Populations that have undergone radiotherapy offer unique insight into the link between radiation exposure and subsequent health risks, as the radiotherapy procedure is ordinarily well-documented, allowing organ doses to be retrospectively calculated from treatment details. However, for many retrospective dosimetry studies, anatomical x-ray computed tomography (CT) data are either unavailable or do not cover out-of-field organs at risk. In these circumstances, computational

phantoms can be a convenient surrogate for the unknown patient anatomy. Whereas CT images typically cover only part of the body and require manual segmentation of all tissues of interest, state-of-the-art computational phantoms [1] provide whole-body anatomy for extended dosimetry with detailed organs and tissues already delineated.

Such phantom resources could be used to reconstruct or extend patient anatomy for a multitude of radiotherapy applications, if the phantom can first be properly defined in a file format compatible with commercial treatment planning systems (TPS). This file format, the Digital Imaging and Communications in Medicine - Radiotherapy (DICOM-RT), is the international standard for the storage of medical image information. Previous research has established workflows using computer-aided design software to make the conversion from voxel phantom to DICOM-RT format possible, but manually rigorous and slow [2]. The current work aims to make this connection between phantom resources and radiotherapy software fully-automatic and more efficient.

## II. METHODS

### A. Creation of phantom DICOM CT image set

As a first step, the *DICOM-RT Generator* converts the voxel phantom into a simulated x-ray CT image set. Voxel values of the organ-associated 8-bit unsigned integers, referred to as organ tags, are read into MATLAB and stored as a three-dimensional matrix. Scripts were written to convert organ tags to their associated mass density based on a user-provided tag dictionary file. These densities are converted into Hounsfield units (HU) based on a linear interpolation of a mass density-to-HU calibration curve which was clinically commissioned at the University of Michigan [2]. Resultant CT data were written out as a DICOM CT image set.

### B. Creation of phantom DICOM RT-structure file

The RT-Structure file contains metadata describing the contours for all organs requested of the *DICOM-RT Generator*.

Within the metadata fields, the contour sequence must be specified, which hold the physical coordinates of the organ contour boundary locations. To calculate these locations, the organ tag values are read into a three-dimensional matrix. A binary mask of the organ is then found on each z-dimensional slice by searching for voxels containing the organ's tag value(s). If an organ can be separated into left and right components (e.g. kidneys, ovaries, etc.) the *DICOM-RT Generator* has the capability to define them as separate structures by considering only one side of the matrix. Scripts were written to trace the boundaries of the organ, including boundaries of hole regions, and return a set of boundary locations defining a closed polygon for each boundary; for the same image slice, this can include one external boundary and one or more internal boundaries, or multiple external island boundaries. Boundary tracing is performed using the Moore-Neighbor tracing algorithm modified by Jacob's stopping criteria; voxels are considered connected if their edges or corners touched. Boundary locations were translated to Cartesian positions and stored within nested branches of the RT-Structure file metadata as required by DICOM standard.

### III. RESULTS AND DISCUSSION

A graphical user interface for the *DICOM-RT Generator* has been created, with entry modes available for any type of voxel phantom. The software performance was tested on a variety of phantoms created in-house and gathered from external sources.

The entirety of the UF/NCI phantom library [3] was converted to DICOM format using the *DICOM-RT Generator*, producing 351 total DICOM file sets. Run-times of the software were around seven minutes for converting each phantom, with resultant total DICOM file size (RT-Structure file and all DICOM CT files) of around 100 MB each. Fifty-five organ contours are included, such as: the brain, eyes, eye lens, spinal cord, trachea, colon (ascending, descending, sigmoid, and total), kidneys, and many more. Cortical and spongiosa bones, grouped into nineteen different bone sites, were also contoured for future red bone marrow dosimetry. Figure 1 shows visualization of organ contours for one of the 351 phantoms using Varian Eclipse TPS; smooth transitions from one slice to the next occur within these automatically-generated contours.

TABLE I. ORGAN VOLUME COMPARISON BETWEEN ORIGINAL PHANTOM AND CONVERTED DICOM STRUCTURE IMPORTED INTO VARIAN ECLIPSE TPS

Organ	Age	Original Volume [cm <sup>3</sup> ]	Eclipse TPS Volume [cm <sup>3</sup> ]	% difference
Brain	1	921.0	925.1	0.4
	15	1359.9	1346.1	-1.0
Colon	1	99.0	94.5	-4.5
	15	525.6	503	-4.3
Heart	1	93.4	93.2	-0.2
	15	624.5	615.3	-1.5

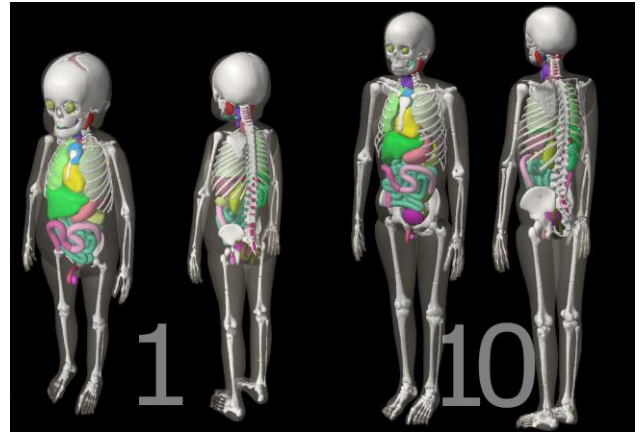


Figure 1: Three-dimensional rendering (not to scale) of the one- and ten-year old UF/NCI male phantoms, visualized within Varian Eclipse TPS. Major organ and skeletal contours are shown.

Table I quantifies the contouring accuracy through a comparison between the original voxel phantom organ volume and the Eclipse TPS-calculated organ contour volume for the brain, colon, and heart in the one- and fifteen-year-old male UF/NCI phantoms. Validation of the organ contour volume is shown to within 5% of the original volume.

### IV. CONCLUSION

This work constitutes a novel method to automatically convert multiple binary voxel phantom files into DICOM-RT format. Extensive testing, beyond what was able to be discussed here, has proven its flexibility to properly convert voxel phantoms into the standard DICOM-RT files compatible with several different commercial TPSs. Auto-generation of contours can be helpful for those organs which are difficult for dosimetrists to segment, such as the skeleton and colon. The converted phantom library, in DICOM format, and a standalone MATLAB-compiled executable of the *DICOM-RT Generator* are available for others to use for research purposes.

### ACKNOWLEDGMENT

The authors would like to thank Niek Schreuder, M.Sc. DABR, of the ProvisionCares Proton Therapy Center for helping to test the converted phantoms within the Raystation treatment planning system. The contents of this work are solely the responsibility of the authors and do not necessarily represent the official views of the National Institutes of Health.

### REFERENCES

- [1] Xu, X. G. "An exponential growth of computational phantom research in radiation protection, imaging, and radiotherapy: a review of the fifty-year history." *Phys. Med. Biol.* 59 R233-302.
- [2] Lee C. et al. "Reconstruction of organ dose for external radiotherapy patients in retrospective epidemiologic studies." *Phys. Med. Biol.* 55 399-63.
- [3] Geyer et al. "The UF/NCI family of hybrid computational phantoms representing the current US population of male and female children, adolescents, and adults – application to CT dosimetry." *Phys. Med. Biol.* 59 5225.

# The J45 Phantom Series and their Potential for Updates to the Atomic Bomb Survivor Organ Doses

Wesley Bolch<sup>1\*</sup>, Keith Griffin<sup>2</sup>, Colin Paulbeck<sup>3</sup>, Choonsik Lee<sup>2</sup>, Harry Cullings<sup>4</sup>, Stephen Egbert<sup>5</sup>, Sachiyo Funamoto<sup>4</sup>, Tatsuhiko Sato<sup>6</sup>, Akira Endo<sup>6</sup>, and Nolan Hertel<sup>7</sup>

<sup>1\*</sup>J. Crayton Pruitt Family of Biomedical Engineering, University of Florida, Gainesville, FL USA

<sup>2</sup>Division of Cancer Epidemiology and Genetics, National Cancer Institute, Rockville, MD USA

<sup>3</sup>Medical Physics Program, College of Medicine, University of Florida, Gainesville, FL USA

<sup>4</sup>Department of Statistics, Radiation Effects Research Foundation, Hiroshima, Japan

<sup>5</sup>Consultant, San Diego, CA USA

<sup>6</sup>Nuclear Science and Engineering Center, Japan Atomic Energy Agency, Tokai-mura, Japan

<sup>7</sup>George W. Woodruff School of Mechanical Engineering, Georgia Institute of Technology, Atlanta, GA USA

\*Corresponding author: wbolch@ufl.edu

**Abstract**— One of the largest sources of data on radiation exposure effects to humans lies in the study of the atomic bomb survivors at Hiroshima and Nagasaki, Japan performed by the Radiation Effects Research Foundation (RERF). As part of their retrospective dosimetry efforts for the atomic bomb survivors, RERF has published two core systems: Dosimetry System 1986 (DS86) and Dosimetry System 2002 (DS02). Due to computing limitations of the time, only three stylized phantoms were used in DS86 and DS02 to represent the entire Japanese population: hermaphroditic models of an infant, child, and adult. Our study aimed to evaluate the dosimetric impact that should be expected from using an updated and age-expanded RERF phantom series with the survivor cohort. Furthermore, the DS86 and DS02 systems report dose to the uterine wall in the non-pregnant adult stylized phantom as a surrogate for the organs of the developing fetus, even at the very latest stages of gestation. To this end, we developed a new series of hybrid phantoms, based on the Japanese population of 1945, which has greater anatomical realism and improved age resolution over those used by RERF.

**Index Terms**—LSS Study, RERF, Organ Dosimetry, Radiation Epidemiology, Fetal Organ Dose

## I. INTRODUCTION

Our study aimed to evaluate the dosimetric differences that should be expected from using an updated and age-expanded J45 phantom series with the Japanese atomic bomb survivor cohort. To this end, we have developed a new series of hybrid computational phantoms, based on the Japanese population in 1945, which has greater anatomical realism and improved age resolution (0-, 1-, 5-, 10-, 15-year-old, and adults) than those used previously by RERF [1-3]. These phantoms were converted to voxel format and compared to their older counterparts through the computation of organ dose coefficients using DS02 total FIA neutron and photon fluences at three distances from the hypocenter. Organ dose coefficients were compared between the age groups to see how new computational phantom technology, as well as a greater resolution of subject age (and thus body size), may impact the dose calculation results within the RERF Dosimetry System.

Organ dose coefficients were also compared against one another to determine the accuracy of the epidemiological use of one organ dose as the surrogate to another (e.g., colon dose as a surrogate for any solid cancer site). We further explored the appropriateness of using the uterine wall as a dosimetric surrogate for whole fetus and for individual fetal organs. It is also important to remember that the pregnant female is herself a member of the atomic bomb cohort, and so we additionally explored changes in maternal organ dose as a function of gestational age as only an anatomic model of the non-pregnant female was used in DS86 and DS02.

## II. METHODS

We developed a new series of computational human phantoms, representing Japanese atomic bomb survivors, by adjusting the existing series of the pediatric and adult hybrid phantoms representing reference Caucasians developed by the University of Florida and National Cancer Institute (UF/NCI) [4]. We obtained the body size of the Japanese children and adult population in 1945 published in RERF DS86: height (cm), weight (kg), and length of trunk, neck, and head (corresponding to sitting height) (cm). The original hybrid phantoms were modified according to the following steps. First, we performed 3D scaling of the whole phantom to match targets on Japanese sitting heights. Second, we performed 1D scaling of the legs to match targets on Japanese standing height. Finally, the amount of adipose tissue (mainly within the abdominal region) was adjusted to match targets on Japanese total body weight to within 1%, which was iteratively performed between adjusting the original hybrid phantoms, which are in Non-Uniform Rational B-Spline (NURBS) and polygon mesh formats, and counting voxels following the voxelization process conversion of surface format to voxel format. The new J45 phantoms were voxelized at resolutions ranging from 0.663 x 0.663 x 0.663 mm (newborn) to 1.579 x 1.579 x 2.207 mm (adult male). After voxelization, lymphatic nodes and muscle were generated by using previously published methods. The male and female

phantoms from newborn to 10-year-old share the identical anatomy with the exception of the gender-specific organs: the prostate and testes for male phantoms, the uterus and ovaries for female phantoms, and the gender-specific shape and position of the urinary bladder. Four of the eight members of the UF pregnant female models were scaled to match appropriate body morphometry targets for 1945 Japanese adult pregnant females. Four parameters were used as the basis for phantom scaling. The first two were the standing and sitting heights of the non-pregnant adult female as shown in Table 1, as taken from Chapter 8 of the DS86 report series, and then applied across all gestational ages. Next, the total fetal mass at 38-weeks' gestation was set equivalent to that of the DS86 at-term newborn. The ratio between the UF 38-week fetus to the J45 38-week fetus was then applied to all fetal weights of the UF series to generate targets at the younger J45 fetal ages. Similarly, the ratio of the weights of the DS86 non-pregnant adult female to the weight of the UF/NCI non-pregnant female were applied across the UF pregnant female phantom series to generate targeted weights for the new J45 pregnant female phantom series. The sitting and standing heights for the DS86 non-pregnant adult female were assumed to be the same for all members of the J45 pregnant female phantom series.

### III. RESULTS

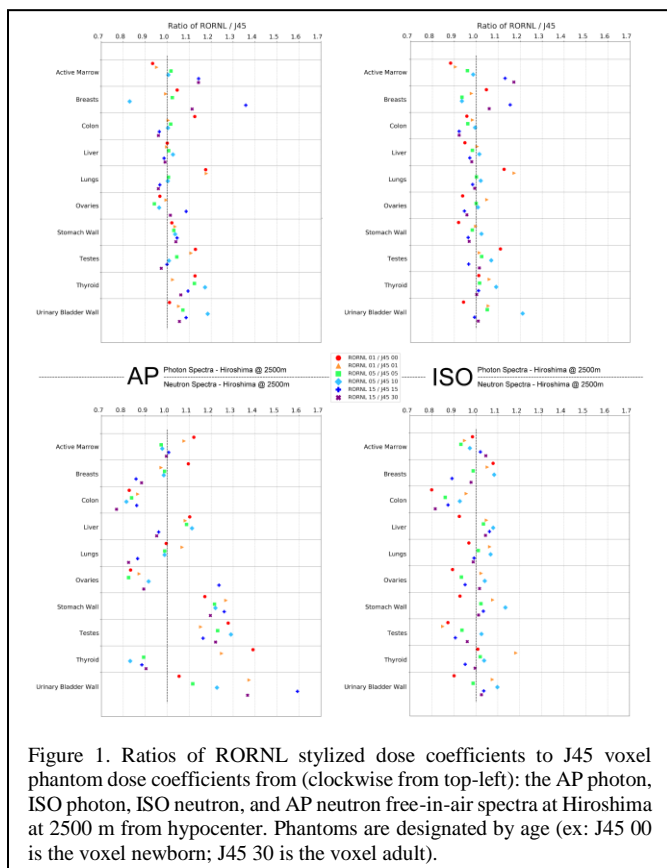


Figure 1. Ratios of RORNL stylized dose coefficients to J45 voxel phantom dose coefficients from (clockwise from top-left): the AP photon, ISO photon, ISO neutron, and AP neutron free-in-air spectra at Hiroshima at 2500 m from hypocenter. Phantoms are designated by age (ex: J45 00 is the voxel newborn; J45 30 is the voxel adult).

Figure 1 gives ratios of ORNL to J45 voxel dose coefficients for ten radiosensitive organs from the AP and ISO irradiation

fields, using FIA fluences at Hiroshima at 2500 m distance from hypocenter.

### IV. CONCLUSION

An updated and age-expanded series of voxel phantoms for future use in an RERF Dosimetry System has been shown to provide significant improvements to survivor organ dosimetry, mostly to those survivors who were misrepresented in body size at the extremes of the age bin groups and to those who experienced a highly-directional irradiation field. Photon dose estimates using the stylized DS86/02-style phantom series showed overall comparable results to the new voxel phantom series, with exception in the newborn and 10-year-old estimates for some organs. On the other hand, neutron dose estimates were dissimilar between the phantom series, mostly for the mono-directional AP field. The increased availability of organs within the new phantom series has also been shown to provide significant enhancements in dosimetry to organs which previously were estimated through the use of surrogate organs.

Our study results for fetal organs indicate that the uterine wall of the non-pregnant female generally underestimates fetal organ dose within the pregnant female. The magnitude of these differences varies with both radiation type and irradiation geometry, with the smallest differences (5-7%) seen for ISO photon fields and the largest differences (20-30%) seen for AP neutron fields. Significant discrepancies were seen in fetal brain dose and its uterine wall surrogate, particularly for photon AP fields (ratio of uterine to brain dose from 0.9 to 1.3) and neutron AP fields (dose ratios from 0.75 to 2.0). The impact of fetal position on estimates of fetal organ dose will be explored in a future study. As for the maternal organ doses, the use of organ doses in a non-pregnant female were shown to, in general, overestimate the corresponding organ doses in the pregnant female, with greater deviations seen at later stages of pregnancy (12-16% for AP photons and 44-53% for AP neutrons). The one exception was the uterine wall dose in pregnancy which was seen to be underestimated by that in the non-pregnant female phantom, particularly for ISO and AP neutron fields.

### ACKNOWLEDGMENT

The Radiation Effects Research Foundation of Hiroshima and Nagasaki, Japan is a public interest foundation funded by the Japanese Ministry of Health, Labour, and Welfare and the US Department of Energy. This publication was supported by RERF Research Protocol 18-59.

### REFERENCES

- [1] Cullings HM, Fujita S, Funamoto S, Grant EJ, Kerr GD, Preston DL. Dose Estimation for Atomic Bomb Survivor Studies: Its Evolution and Present Status. *Radiat Res.* 2006 Jul 1;166(1):219–54.
- [2] US-JAPAN joint reassessment of atomic bomb radiation dosimetry in Hiroshima and Nagasaki: Final report (W. C. Roesch, Ed.) Hiroshima, Japan: Radiation Effects Research Foundation, 1987.
- [3] Young RW, Kerr GD, eds. Reassessment of the Atomic Bomb Radiation Dosimetry for Hiroshima and Nagasaki - Dosimetry System 2002. Hiroshima and Nagasaki, Japan: Radiation Effects Research Foundation; 2005.
- [4] Lee C, Lodwick D, Hurtado J, Pafundi D, Williams JL, Bolch WE. The UF family of reference hybrid phantoms for computational radiation dosimetry. *Phys Med Biol.* 2010 Jan 1;55(2):339–63

# Scientific Session

Wednesday, 24 July 2019

<b>11:30 – 12:50</b>	<b>Scientific Session “Radiation Protection”</b> <b>Chair: Andrew Maidment, Co-Chair: Wesley E. Bolch</b>
11:30	Shielding verification and optimization for proton therapy based on Monte Carlo simulation Zhuo Yan, Hongdong Liu, X. George Xu, and Zhi Chen
11:50	Development of Chinese pediatric reference phantoms series and application in CT dose estimation Ruiyao Ma, Rui Qiu, Ankang Hu, Li Ren, Zhen Wu, Chunyan Li, and Junli Li
12:10	Virtual calibration of whole-body counter using a library of statistical phantoms Laleh Rafat-Motavalli, Elie Hoseinian-Azghadi, and Hashem Miri-Hakimabad
12:30	Using phantoms and HoloLens for virtual reality based operator radiation safety training in interventional radiology Yi Guo, Li Mao, Yongzhe Li, Gongsen Zhang, Yiming Gao, Larry Dauer, Xi Pei, Zhi Chen, and X. George Xu

# Shielding Verification and Optimization for Proton Therapy Based on Monte Carlo Simulation

Zhuo Yan<sup>1</sup>, Hongdong Liu<sup>1</sup>, X. George Xu<sup>1,2</sup>, and Zhi Chen<sup>1,\*</sup>

<sup>1</sup>School of Physical Science, University of Science and Technology of China, Hefei, China

<sup>2</sup>Rensselaer Polytechnic Institute, Troy, New York, USA

\*Corresponding author: zchen@ustc.edu.cn

**Abstract**—In this paper, shielding design of a new proton therapy facility in Hefei, China is evaluated through the calculation of the effective dose using Monte Carlo simulations and voxelized computational human phantoms and comparison with the dose equivalent values from empirical formulas. The results demonstrate the accuracy of Monte Carlo methods in the shielding design of a new proton facility.

**Index Terms**—Proton therapy; Monte Carlo simulation; Shielding; Human Phantoms

## I. INTRODUCTION

Proton therapy is becoming increasingly popular worldwide including China. According to PTCOG [1], as of February 2019, 80 proton therapy facilities were in operation, and 41 were under construction around the world. The shielding design and evaluation for such relatively new facilities in China remain to be a challenge [2]. Considered to be the most accurate method for complex accelerator shielding analysis, Monte Carlo (MC) simulations have been used in proton therapy systems [3].

The goal of this study is to evaluate a proton therapy shielding system using MC methods and human phantoms. We use a cylinder made of copper as the proton accelerator nozzle, and voxelized computational human phantoms representing members of the general publics, doctors and technicians working in or near the therapy equipment.

First, we use empirical formulas to calculate dose equivalent rate (DER) in a treatment room at points of interest (POI) inside and outside the shielding. Then, we use Geant4/TOPAS code to calculate the absorbed dose (AD) in different parts of human body and then the effective dose (ED) for various conditions (the position of human phantoms and the role they serve as) in order to evaluate the shielding design strategies.

## II. METHODS

In this study, we consider the proton beams of a superconducting cyclotron for proton therapy system designed by ASIPP (Hefei, China) and JINR (Dubna, Russia) involving a maximum proton energy of 202 MeV with the maximum beam current of 0.5  $\mu$ A [4].

In Figure 1, the blueprint of the treatment room for proton therapy is depicted. It includes: A cyclotron vault, where the

protons are emitted, beam lines where the energy selection system is located, cyclotron power supply and control room, a treatment room with gantry and a fixed treatment room where 6 POIs (numbered 1 to 6) are set to represent the locations of people.

In the treatment room, assuming there is only random beam loss from the entrance to the nose, and the emitted beams are entirely used for medical treatment. Considering that the proton energy ranges from 130 MeV to 202 MeV, there is a neutron-photon mixed field produced by protons interacting with materials. However, the radiation field is dominated by neutrons because of low photon dose rate [5].

The DER limitation is 2.5  $\mu$ Sv/h where the occupancy factor T is no less than 1/2 and 10  $\mu$ Sv/h where T is less than 1/2 [6], respectively. The basic geometry of shielding calculation is depicted in Figure 2. In order to improve radiation safety, both MC simulations and conservative calculation are needed.

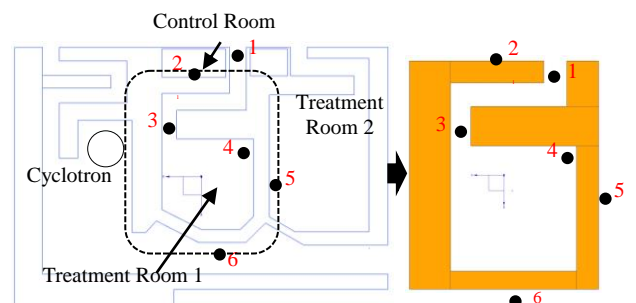


Figure 1. Blueprint of the Hefei Ion Medical Center operating a 202 MeV proton medical cyclotron (POIs are represented by black dots).

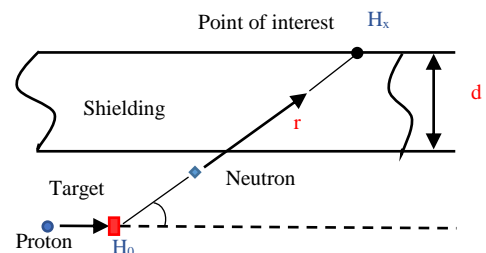


Figure 2. The geometry relevant to shielding calculations for proton accelerators

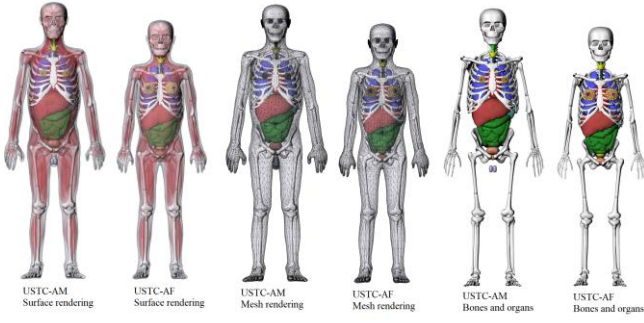


Figure 3. The 3D rendering of adult phantoms

### Conservative calculation of DER

In Figure 2, The DER  $H_0$  at the impact point produced by protons impinging on the target reduced to  $H_x$  at POI on the outer side of the shielding (whose thickness is “ $d$ ”). The distance between target and POI is “ $r$ ”. Then, the DER outside a wall can be described as the follows [7]:

$$H = H_0 \frac{\exp(-\frac{d}{\lambda(E)})}{r^2} \quad (1)$$

where  $\lambda(E)$  represents the energy dependent neutron attenuation length for which  $138 \text{ g cm}^{-2}$  is used according to this paper [8]. In addition, the DE at maze is also described in NCRP No. 144:

$$H(r_i) = 2H_0(r_0) \left(\frac{r_0}{r_i}\right)^2 \quad (2)$$

$$H(r_i) = \left( \frac{e^{-r_i/0.45} + 0.022A_i^{1.3} e^{-r_i/2.35}}{1 + 0.022A_i^{1.3}} \right) H_{0i} \quad (3)$$

where  $r_0$  is the distance between the source and the entrance of the first maze,  $r_1$  and  $r_i$  are the depth of the first or  $i^{\text{th}}$  maze,  $H_0(r_0)$ , and  $H_{0i}$  are the DER at the entrance of the first or  $i^{\text{th}}$  maze, and the  $A_i$  is the cross-sectional area of the  $i^{\text{th}}$  maze.

### MC simulations of ED

In this paper, the mesh-based USTC adult male (USTC-AM) is used (shown in Figure 3) to represent the human body [9]. Then, the AD of different organs are simulated by using TOPAS code, which can later be converted into the ED of a human body through the following steps:

$$\text{Equivalent Dose} = \sum (\text{Absorbed Dose}) \times W_R \quad (4)$$

$$\text{Effective Dose} = \sum (\text{Equivalent Dose}) \times W_T \quad (5)$$

where  $W_R$  and  $W_T$  are the radiation weighting factor and the tissue weighting factor, respectively, and the value of these two factors are given by the ICRP Publication 103 [10].

### III. RESULT

In order to find out the connection between the DER at POI (using conservative calculation) and the ED of human phantoms (using MC simulation), an extra case is considered—the simulation of AD at POI (using MC simulation). Hence, the main results are as follows:

- (1) The comparison between the conservatively calculated DER and the results using MC simulation.
- (2) On the condition of using MC simulation, the ED of human phantoms and the dose at corresponding POI are also compared, which could provide evidence for the connection between shielding design and radiation safety of people.

### IV. CONCLUSION

This paper highlights the importance of MC simulations in the shielding and radiation safety for a new proton facility in China, compared to conservative calculation shown in NCRP report No. 144. The results by Monte Carlo simulations using TOPAS provide more accurate shielding design, although it takes a very long computing time to obtain the results.

### FUNDING

This work was supported by research funding from the National Key Research and Development (R&D) Program of China (Grant no. 2017YFC0107504).

### REFERENCES

- [1] Particle Therapy Co-Operative Group. 2019. Available at <http://ptcog.web.psi.ch/>.
- [2] ICRP. “Relative biological effectiveness, radiation weighting and quality factor,” *Annals of the ICRP*, 2003, pp. 92-33.
- [3] H. Paganetti, “Range uncertainties in proton therapy and the role of Monte Carlo simulations,” *Phys. Med. Biol.*, vol. 57, R99–R117, 2012.
- [4] Karamysheva G.A. et al., “Compact Superconducting Cyclotron SC200 for proton therapy,” *Cyclotrons and Their Applications 2016*, Sept. 2016, Zürich, Switzerland, paper THC03, pp. 371-373.
- [5] Newhauser W, Titt U, Dexheimer D, Yan X, Nill S. “Neutron shielding verification measurements and simulations for a 235-MeV proton therapy center,” *Nucl Instrum Methods Phys Res A*, vol. 476, pp. 80-84, 2002.
- [6] GBZT201.5-2015, “Radiation shielding requirement for radiotherapy rooms-Part5: Radiotherapy room of proton accelerators,” 2015.
- [7] NCRP Report No. 144. *Radiation protection for particle accelerator facilities*, NCRP, 2005.
- [8] Moritz LE., “Radiation protection at low energy proton accelerators,” *Radiat Prot Dosimetry*, vol. 96, pp. 297-309, 2001.
- [9] Pi Y., Liu T., and Xu X. G., “Development of a set of mesh-based and age-dependent Chinese phantoms and application for CT dose calculations,” *Radiation protection dosimetry*, vol. 179, pp. 370-382, 2018.
- [10] Valentin J. “The 2007 Recommendation of the International Commission on Radiological Protection 103,” *Annals of the ICRP*, 2007, pp. i-i.

# Development of Chinese Pediatric Reference Phantoms Series and Application in CT Dose Estimation

Ruiyao Ma<sup>1,2</sup>, Rui Qiu<sup>1,2\*</sup>, Ankang Hu<sup>1,2</sup>, Li Ren<sup>3</sup>, Zhen Wu<sup>3</sup>, Chunyan Li<sup>3</sup> and Junli Li<sup>1,2</sup>

<sup>1</sup>. Department of Engineering Physics, Tsinghua University, Beijing, China

<sup>2</sup>. Key Laboratory of Particle & Radiation Imaging, Tsinghua University, Ministry of Education, Beijing, China

<sup>3</sup>. Joint Institute of Tsinghua University and Nuctech Company Limited, Beijing, China

\*Corresponding author: qiurui@mail.tsinghua.edu.cn

**Abstract**—A series of mesh-type Chinese pediatric reference phantoms for 3 months, 1 year, 5 years, 10 years, 15 years male and female were developed based on the CT medical images of different ages. The mass of individual organs has been adjusted to the Chinese reference value with the difference less than 5 %. The Monte Carlo simulation model of a GE LightSpeed 16 CT scanner was modeled. The organ doses of Chinese pediatric reference phantoms from single axis scan were calculated based on the Chinese reference phantom and an organ dose database was established for different scanning parameters. The organ doses calculated in this work were compared with simulation data in other studies.

**Index Terms**—*pediatric phantoms series; mesh-type phantom; computed tomography scan*

## I. INTRODUCTION

Recently, the amount of radiation exposure from medical sources continues to increase for children. In addition, compared with the adult, the growing children are more vulnerable to the ionizing radiation. Therefore, it is necessary and urgent to assess the dose of medical exposure to children. Monte Carlo simulation using the computational phantoms is the main method of dose calculation.

For children in the growing period, considering the characteristics of the quick growth and development of the tissue and organ, it is of great significance to establish the phantoms of the children for different ages. For the advantage of greater deformability and more accurate organ description to the voxel-type model, the mesh-type model can be the better choice to establish the computational phantoms.

In recent years, the CT examination frequency for pediatric examinee increased a lot in China. The dose contribution of CT examination in various X-ray diagnosis is large. More and more attention has been paid to the radiation dose caused by CT examination. Therefore, the developed Chinese pediatric reference phantoms were applied in CT dose estimation.

## II. METHODS

### A. Development of Chinese pediatric reference phantoms

The computed tomography (CT) images were obtained from the Capital Institute of Pediatrics, Beijing. The basic

statistic was not a whole body CT imaging, but composed of CT imaging sets of different body parts from several patients. Therefore, it is necessary to perform primary registration manually, according to the rudimentary knowledge of anatomy. A software named 3D-DOCTOR was used to segment the contours of different organs and bones from the CT tomographic slices. The surface rendering function of the 3D-DOCTOR can develop the contours of the different organs and bones into polygon-mesh (PM) models.

The polygon-mesh (PM) models constructed by the 3D-DOCTOR were always composed of extreme excess meshes, which was not convenient for the phantom adjustment. The number of the meshes were reduced to appropriate quantity in the Rhinoceros software. The primitive models were refined to turn into high-quality models by smoothing and mending the surface. Considering that the patient's physical data cannot be completely consistent with the reference data, it is required to adjust the mass of each organs to fit the reference data. The reference volume of each organs were calculated referring to the ICRU46 report [1], GBZ/T 200.2 — 2007[2], Asian reference man [3] data. The volume of the refined organs and bones were adjusted to consist with the reference data via scale scaling and so on.

The basic PM models of skeleton were produced by using the same conversion procedure employed for the general organs and tissues. Furthermore, the bones were divided into two parts, external cortical bone and internal cancellous bone. The GBZ/T 200.2—2007 provides reference masses of different skeletal tissues. The distribution of each skeletal tissues was given by the ICRP Publication 70 [4] and ICRP Publication 89 [5]. The nonuniform bone model constructed distinguished the different skeletal tissues, which is beneficial to adjust the skeleton closely to the real anatomical structure.

The organs, which had not been recognized in the CT, were developed via non-uniform rational B-spline (NURBS) method. The large intestine was constructed as a changing diameter pipe, while the small intestine as a constant diameter pipe. The organs such as rib cartilage, salivary glands and tongue were transformed from the basic geometry to be similar to the real shape. The NURBS can be converted into PM model via the Rhinoceros software.

Established organs and bones were assembled into a complete phantom. The overlapping parts were adjusted appropriately. It was achieved by subtle movement of the position and transformation of the organ shape. In Rhinoceros software, we can set series control points on the NURBS surface to complete partial adjustment and keep the mass fit with the reference data at the same time.

### B. Application in CT dose estimation

#### 1) Development of CT and simulation based on THUDose

THUDose is a Monte Carlo modeling and simulation software with user-friendly UI, which is developed by our laboratory based on Geant4. And the modeling and simulation processes of this work were carried out based on THUDose. The Monte Carlo model of LightSpeed 16 CT developed from GE company was established. The distance from source to phantom center of this type CT is 54 cm. The energy spectrums adopted by X ray are generated by XCOMP5 software. And the tube voltage of X ray includes 140, 120, 100 and 80 kVp. The width of collimator can be chosen as 20, 10, and 5 mm. The two types of filter include head and body type to be applied in head and body scanning, with beam angle of 27.5° and 55° respectively. The establishment of CT model was verified by experiment and published in journals.

CT scanning includes spiral scanning and axial scanning. Organ doses obtained from spiral scanning are related with the pitch, and it is approximately equal with organ doses obtained from the axial scanning with same scanning parameters. Therefore, axial scanning type is simulated in this work to calculate organ doses database. And this method was verified with calculate experience. 16 X ray sources and filters are uniform arranged in circle to simulate X ray tube rotating one circle in fact. The collimators were moved from the head to the feet of the phantom (z axial), and the organ doses were calculated for once axial scanning in each position. Scanning conditions including tube voltages with 140, 120, 100 and 80 kVp, collimators with 20, 10, and 5 mm width, filters with head and body types were simulated, and the datasets including organ doses obtained from single layer axial scanning were established. Using the database, organ and effective doses in any scan mode were obtained easily. And a web-based CT dose assessment software were developed to promote the clinical use.

### III. RESULTS

The heights of the six established phantoms were 62 cm, 77 cm, 110 cm, 139 cm, 168 cm and 158 cm, respectively, and the weights were 7 kg, 10 kg, 19 kg, 32 kg, 55 kg and 50 kg, complied with the reference value in GBZ / T 200.2-2007. Each mesh-type phantom consists of 108 different tissues and organs, which includes all the radiation-sensitive organs contained in the latest ICRP proposal. The differences of the organ mass with the Chinese reference value are less than 5%.

The organ doses of Chinese pediatric examinee from single axis scan were calculated based on the Chinese pediatric reference phantoms and an organ dose database was established. A web-based CT dose assessment software was

developed to read data from the organ dose database according to the CT scanning parameters entered by the user and calculate the organ absorbed dose and effective dose rapidly.



Figure 1. Interface of the software for CT dose assessment

### IV. CONCLUSION

This series established mesh-type reference phantoms can be transformed into voxel phantoms, which can be applied in Monte Carol method for variety dosimetry simulation. Organ and effective doses conversion coefficients of pediatric examinee undergoing CT scanning are calculated using Geant4 based on Chinese pediatric reference phantoms. The data calculated in this paper will be used for the revision of China's national standard for estimation of examinee's organ doses. The CT dose assessment software provides a powerful tool for the simple and rapid assessment of radiation dose of pediatric examinees undergoing CT examinations.

### ACKNOWLEDGMENT

This work was supported by the National Natural Science Foundation of China [Grant No. 11875036] and Tsinghua University Initiative Scientific Research Program [20151080355].

### REFERENCES

- [1] International Commission on Radiation Units and Measurements, *Photon, electron, proton, and neutron interaction data for body tissues. Report 46*, ICRU, 1992.
- [2] Ministry of Health, P.R.China, *GBZ/T 200.2—2007 Reference individuals for use in radiation protection Part2:Masses of main organs and tissues*. Beijing, People's Medical Publishing House, 2007.
- [3] Gi-ichiro Tanaka, and Hisao Kawamura, *Anatomical and physiological characteristics for Asian reference man : Male and female of different ages : Tanaka model*. Hitachinaka, National Institute of Radiological Sciences. Division of Radioecology, 1996.
- [4] ICRP, "Basic Anatomical & Physiological Data for use in Radiological Protection: The Skeleton. ICRP Publication 70," *Annals of the ICRP*, vol. 25(2), 1996.
- [5] ICRP, "Basic anatomical and physiological data for use in radiological protection: reference values : ICRP Publication 89," *Annals of the ICRP*, vol. 32, pp. 3-4, 2002.

# Virtual calibration of whole-body counter using a library of statistical phantoms

Laleh Rafat-Motavalli, Elie Hoseinian-Azghadi, and Hashem Miri-Hakimabad\*  
Physics Department, Faculty of Science, Ferdowsi University of Mashhad, Mashhad, Iran  
\*Corresponding author: mirihakim@um.ac.ir

**Abstract**—In this study, virtual calibration of a whole-body monitoring system was performed using a library of 100 statistical phantoms. The counting efficiency (CE) was obtained as a function of time after  $^{131}\text{I}$  radionuclide intake. The results highlight the necessity of using statistical phantoms in the process of virtual calibration because it was found that the CE for  $^{131}\text{I}$  is not a simple function of height, weight, BMI or any other morphometric variable. Despite, it was shown that the counting efficiency is strongly dependent on the geometrical location of the thyroid and the thickness of soft tissue between the thyroid and the detectors.

**Index Terms**—whole-body counter; Monte Carlo method; virtual calibration; statistical phantoms, radiation contamination

## I. INTRODUCTION

In the virtual calibration of in vivo monitoring instruments, computational phantoms which include the complicated structure of human anatomy are used to assess the organ specific counting efficiency (OSCE) [1]. Although utilizing a realistic computational phantom instead of simple physical models increases the accuracy; without personalized models, this method has another source of uncertainty pertained to the anatomical variations in measurement subjects [2]. Therefore, some researchers created phantom libraries comprising of various weight and height percentiles to take into account the statistical uncertainty of the morphometric features. However, because of lacking the anatomical information, the internal organs were assumed identical for the same height phantoms. To make the other height percentiles, all the organs were just scaled with the whole body [3]. This issue could effectively contribute to the systematic error in OSCE estimation, especially when contamination is concentrated in a specific organ. In this work, a library of 100 phantoms with internal and external statistical features were used to calibrate a whole body counter (WBC) for  $^{131}\text{I}$  which is assumed to be predominant contributor to the internal dose after a nuclear power plant accident.

## II. METHODS

### A. Simulating of statistical phantoms inside the WBC

The phantom series used in this study were constructed as a library of 100 statistical boundary representation phantoms. The sampling of height and weight of the patients were done uniformly and including adult males and females.

A FASTSCAN WBC unit (Canberra Inc., USA) was simulated in MCNPX 2.6 code which has a free standup geometry. The unit houses two sodium iodide (NaI) gamma-ray detectors [4].

### B. Biokinetics of radiation contamination in body

The compartmental biokinetic model of the inhaled  $^{131}\text{I}$  was created as a combination of human respiratory tract model (HRTM) from ICRP Publication 130 [5] and the new iodine biokinetic model developed by Leggett [6]. The activity curves versus time after intake were then obtained for inhalation of iodine vapor/gases  $\text{I}_2$ ,  $\text{CH}_3\text{I}$ , and aerosols with AMAD of 1 and  $5\mu\text{m}$ . In addition, the solutions of biokinetic model for blocked and unblocked thyroid as well as various breathing rates and durations were found.

### C. Evaluation of CE

The OSCE,  $\varepsilon_S$ , were evaluated and the total CE,  $\varepsilon_{\text{Total}}$ , were then obtained as a summation of  $\sum A_S(t) \times \varepsilon_S$  for each computational phantom, where  $A_S(t)$  is the activity function for the source region (S).

## III. RESULTS AND DISCUSSION

### A. The total CE and OSCEs for the reference phantom

Monte Carlo simulation was performed and organ specific CEs were obtained for 15 different source regions, separately. The total CE were then obtained by summing the activity-weighted organ-specific CEs. Figure 1 shows the total CE for the adult male ICRP reference phantom as a function of time after inhalation of  $^{131}\text{I}$  aerosols with  $1\mu\text{m}$  AMAD. The

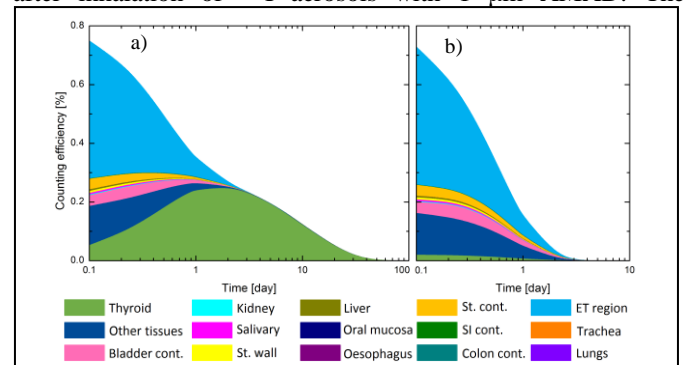


Figure 1. Total CE as a function of time after intake of  $^{131}\text{I}$  aerosols with  $1\mu\text{m}$  AMAD for a reference subject with (a) unblocked and (b) blocked thyroid.

contribution of each source region in the total CE is shown for both blocked and unblocked thyroid in this figure. In the case of unblocked thyroid, the key point is that the thyroid is the major contributor to the total CE after 2 days of radionuclide intake. This implies that the thyroid could be considered alone in the evaluation of total CE. However for blocked thyroid, it was shown that the CE is not considerable after 2 days.

### B. The total CE for the library of statistical phantoms

The total CEs for 100 statistical phantoms were evaluated (figure 2). Figure 3 shows the scatter plot of weight versus height of the computational phantoms. The symbols filled with the color corresponding to the thyroid CE as the major contributor to the total CE. The polygon mesh models of the phantoms pertained to the region indicated with a dashed magenta line was shown in the upper panel from the front view. As can be seen from this figure, there is no obvious correlation between the thyroid CE and its corresponding weight/height percentile.

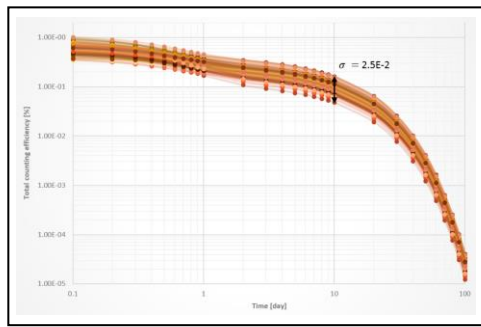


Figure 2. Total CE as a function of time after intake of  $^{131}\text{I}$  aerosols with  $1\ \mu\text{m}$  AMAD for the library of computational phantoms.

### C. The total CE vs. other morphometric parameters

The correlation between thyroid CE versus various parameters including body mass index (BMI) and thyroid mass were investigated and no obvious correlation was found. Then, we explored more deeply and some level of correlation was observed for the thyroid location with respect to the detectors. Therefore, we analytically estimated the solid angle ( $\Omega$ ) of the detectors observed from the thyroid center of mass, multiplied by the attenuation factor ( $\exp(-\mu x)$ ), where  $x$  is the thickness of the soft tissue lied in front of the thyroid and  $\mu$  is the attenuation coefficient of the soft tissue for energy of 0.365 MeV. One may expect that the value would be proportional to the thyroid CE as shown in figure 4.

To sum up, the total CE is dependent on the thyroid CE after 2 days of radionuclide intake, which in turns depends on the thyroid location and the thickness of thyroid frontal layer. Thus, in order to estimate the total CE for each individual subject more precisely, one may fix the location of the thyroid by a neck or chin stabilizer and assess the thickness of soft tissue layer by palpation.

## I. CONCLUSION

The total CE for  $^{131}\text{I}$  as a function of time after intake were evaluated for different scenarios using a library of phantoms, new biokinetics of iodine and Monte Carlo calculations. The influencing factors on the total CE were also investigated.

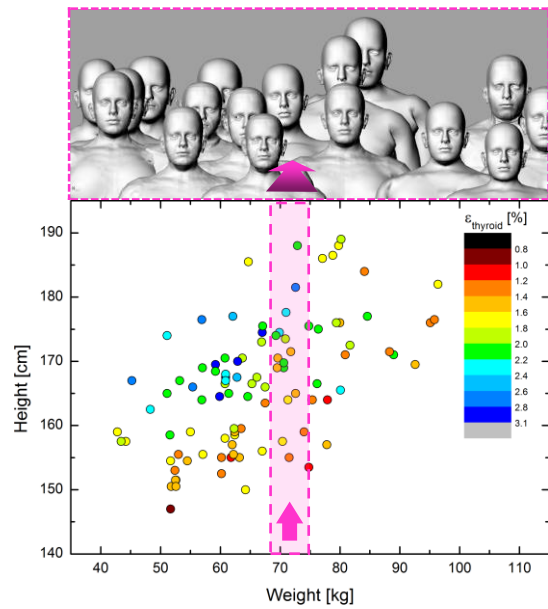


Figure 3. Scatter plot of height versus weight of the phantoms. the symbols filled with the color corresponding to the thyroid CE.

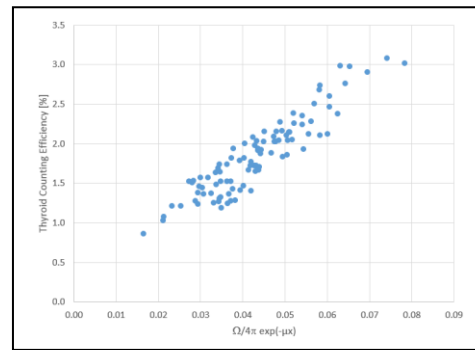


Figure 4. The correlation observed between the thyroid CE and the detectors' solid angle multiplied by attenuation factor for  $^{131}\text{I}$  aerosols with  $1\ \mu\text{m}$  AMAD, plotted

The outcome of this study helps us to reduce the systematic uncertainty of CE pertained to the body habitus of the subject. To conclude, this study highlights the importance of using statistical phantoms in virtual calibration of whole body monitoring systems which we intend to share with computational phantoms workshop.

## REFERENCES

- [1] J. G. Hunt, and L. Bertelli, "Calibration of in vivo measurement systems and evaluation of lung measurement uncertainties using a voxel phantom," *Radiat Prot Dosim* vol. 76, pp. 179–84, 1998.
- [2] S. Pözl, and B. Breustedt, "Personalised body counter calibration using anthropometric parameters," *Radiat Prot Dosim*, vol. 70(1-4), pp. 221-224, 2016.
- [3] Y. Chen, R. Qiu, C. Li, Z. Wu, and J. Li, "Construction of Chinese adult male phantom library and its application in the virtual calibration of in vivo measurement," *Phys Med Biol*, vol. 61(5), pp. 2124, 2016.
- [4] R. Hayano. "Measurement and communication: what worked and what did not in Fukushima", *Ann ICRP*, vol. 45(2\_suppl), pp. 14-22, 2016.
- [5] F. Paquet, G. Etherington, M. R. Bailey, R. W. Leggett, J. Lipsztein, et al., "ICRP Publication 130: Occupational Intakes of Radionuclides: Part 1," *Ann ICRP*, vol. 44(2), pp. 5-188, 2015.
- [6] R. Leggett, "An age-specific biokinetic model for iodine," *J Radiol Prot*, vol. 37(4), pp. 864-882, 2017.

# Using Phantoms and HoloLens for Virtual Reality based Operator Radiation Safety Training in Interventional Radiology

Yi Guo<sup>1</sup>, Li Mao<sup>2</sup>, Yongzhe Li<sup>1</sup>, Gongsen Zhang<sup>1</sup>, Yiming Gao<sup>3</sup>, Larry Dauer<sup>3</sup>, Xi Pei<sup>1</sup>, Zhi Chen<sup>1</sup>, and X. George Xu<sup>1,2\*</sup>,

<sup>1</sup> University of Science and Technology of China, Hefei, China

<sup>2,\*</sup>Rensselaer Polytechnic Institute, Troy, New York, USA

<sup>3</sup> Memorial Sloan Kettering Cancer Center, New York, New York, USA

\*Corresponding author: xug2@rpi.edu

**Abstract**—Interventional radiology suite is known to be a high radiation environment where interventional radiologists, cardiologists and staff members are reportedly associated with an increased potential of developing brain and neck tumors, as well as cataracts. To improve the occupational radiation safety awareness, we developed a virtual reality (VR) software training tool to help operators learn to avoid high radiation areas, through game-like interactive simulation and visualization of the spatial distribution of the X-ray field. Results suggest VR visualization tool is an important means of safety training in interventional therapy

**Index Terms**—virtual reality; organ dose; radiation field; Monte Carlo;

## I. INTRODUCTION

Each year over 10 million fluoroscopically guided interventional (FGI) procedures are performed for diagnostic or therapeutic purposes [1]. Medical staff (typically the physician, technologist, and nurse) must stand near the patient bed and the X-ray source, thus resulting in the highest occupational radiation exposure level among all medical professionals. An alarming number of brain and neck tumors, as well as cataracts, have been reported for FGI operators who are found to have insufficient training of radiation physics and safety [2-8]. Occupational radiation protection during FGI procedures has been a top concern for regulatory agencies, professional societies, and radiologists [9-13].

Previous studies [11,14-17] showed that radiation doses to the eye lens and brain depended heavily on operator's posture and protective equipment. It is worth noting that this X-ray field is invisible to the interventionist who is occupied with the surgical procedure, often failing to minimize radiation exposure. Therefore, it is necessary to develop a visualization tool to visualize the radiation field for operators during interventional therapy.

This paper presents a visualization training tool using virtual reality and Monte Carlo radiation transport code, MCNP. This is the first time a VR-based training tool is reported that aims to help operators learn to avoid high

radiation areas, through game-like interactive simulation and visualization.

## II. METHODS

### Radiation field calculation

The radiation field and three operator phantoms are simulated using Monte Carlo radiation transport code, MCNP to generate a large amount of position- and posture-specific organ dose database. We modeled the radiation source in MCNP according to the real interventional therapy process, and calculated the dose of organs and radiation field using RPI phantoms. Figure 1 shows RPI phantoms we used, the actual interventional therapy scene, as well as 3D rendering of the operator phantoms and a patient.

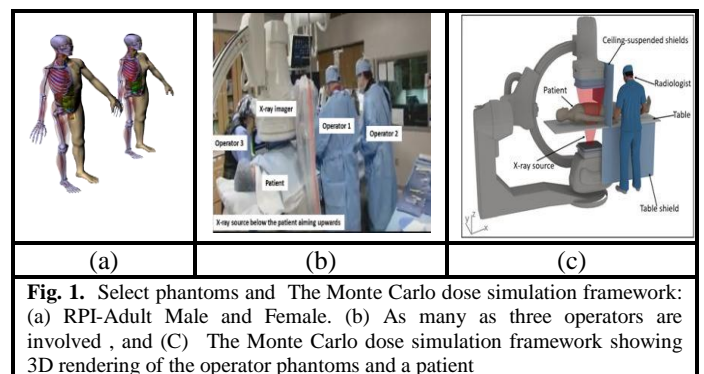


**Fig. 1.** Select phantoms and The Monte Carlo dose simulation framework: (a) RPI-Adult Male and Female. (b) As many as three operators are involved, and (c) The Monte Carlo dose simulation framework showing 3D rendering of the operator phantoms and a patient

### Virtual Reality Equipment

We used Microsoft HoloLens Head-mounted Display Device for our visualization research. By wearing MS HoloLens glasses, users can change their position arbitrarily in the simulated interventional therapy scene to achieve omnidirectional observation. At the same time, MS HoloLens can integrate with the actual environment and get more realistic sensory effects.

### Modeling

In order to simulate real interventional therapy procedures, we need to build virtual models like interventional radiologists, couch and X-ray devices using 3D Studio Max and unity3D. The size and position of the field of X-ray beam can be adjusted manually according to the actual situation. A VR script is written to define radiation field and operator phantoms into the HoloLens environment. Figure.2 shows an interventional procedure and the models we built.

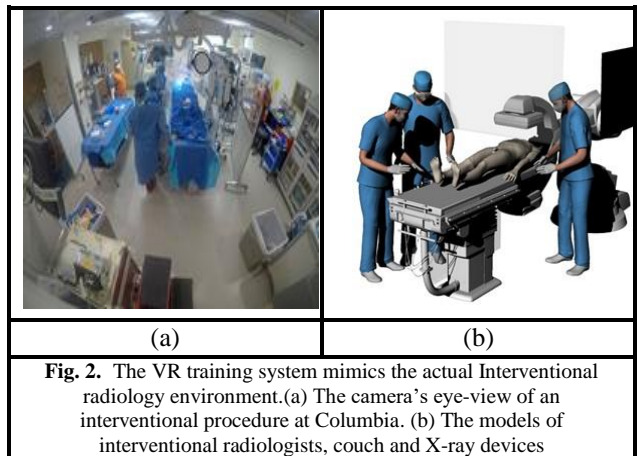


**Fig. 2.** The VR training system mimics the actual Interventional radiology environment.(a) The camera's eye-view of an interventional procedure at Columbia. (b) The models of interventional radiologists, couch and X-ray devices

### III. RESULT

The radiation field in the environment has been calculated and imported into the virtual reality program. By wearing Microsoft HoloLens glasses, the distribution of X-ray beam and radiation field are shown in different colors that red color represents high radiation area and blue color represents low radiation area. Users can feel the radiation intensity intuitively when using different postures and positions. Figure.3 shows the images on HoloLens glasses mapped onto a computer screen and a user manipulates the eye view by gesturing.

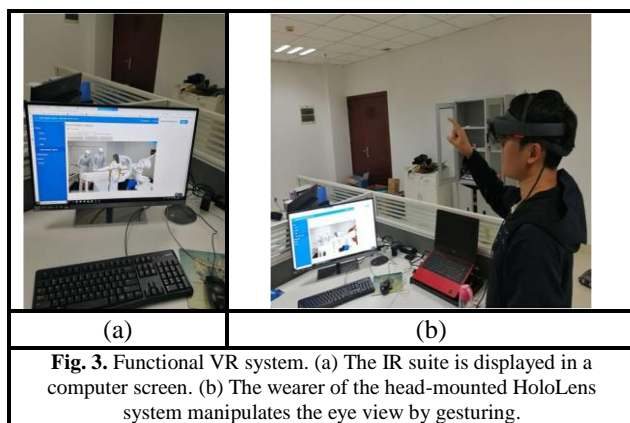


**Fig. 3.** Functional VR system. (a) The IR suite is displayed in a computer screen. (b) The wearer of the head-mounted HoloLens system manipulates the eye view by gesturing.

### IV. CONCLUSION

A preliminary VR-based radiation safety training tool for operators in interventional radiology has been developed and tested using the MS HoloLens system. Pre-calculated X-ray field in the environment alert operators to adjust their postures and positions to minimize exposure to high radiation situations.

### REFERENCES

- [1] Balter, Stephen, "Interventional fluoroscopy: physics, technology, safety". Wiley-Liss, 2001.
- [2] Kitahara CM, Linet MS, Balter S, et al, "Occupational radiation exposure and deaths from malignant intracranial neoplasms of the brain and CNS in U.S. radiologic technologists, 1983–2012" *AJR* 2017; 208:1278–1284.
- [3] Organization for Occupational Radiation Safety in Interventional Fluoroscopy, "Invisible impact: the risk of ionizing radiation on cath lab staff". [www.youtube.com/watch?v=rXgt0bF3GJM&feature=youtu.be](http://www.youtube.com/watch?v=rXgt0bF3GJM&feature=youtu.be). Accessed January 23, 2018.
- [4] Roguin A, Bartal G, "Radiation and your brain". *Endovascular Today*, 2016; 15:63–65.
- [5] Miller DL, Vaño E, Bartal G, et al, "Occupational radiation protection in interventional radiology: a joint guideline of the Cardiovascular and Interventional Radiology Society of Europe and the Society of Interventional Radiology". *J Vasc Interv Radiol* 2010; 21:607–615.
- [6] Roguin A, Goldstein J, Bar O, Goldstein JA, "Brain and neck tumors among physicians performing interventional procedures". *Am J Cardiol*. 2013 May 1;111(9):1368-72.
- [7] Morillo A J, "Occupational Radiation Exposure in Interventional Radiology and the Risks of Acquiring a Brain Tumor". *American Journal of Roentgenology* 2017 209:6, W402-W402.
- [8] Kitahara C M and Miller D L, "Reply to "Occupational Radiation Exposure in Interventional Radiology and the Risks of Acquiring a Brain Tumor"". *American Journal of Roentgenology* 2017 209:6, W403-W403.
- [9] National Council on Radiation Protection and Measurements, "Radiation Dose Management for Fluoroscopically-guided Interventional Medical Procedures", NCRP Report No. 168 (National Council on Radiation Protection and Measurements, Bethesda, 3899 Maryland),2010.
- [10] Kim, K.P., Miller, D.L., Berrington de Gonzalez, a., Balter, S., Klenerman, R.A., Ostroumova, E. SIMON, S.L. and LINET, M.S. , "Occupational radiation doses to operators performing fluoroscopically-guided procedures". *Health Phys*. 103(1), 80,2012.
- [11] Balter, S., "Stray radiation in the cardiac catheterization laboratory". *Radiat. Prot. Dosim*. 94(1–2), 183–188,2001.
- [12] Vano E, Gonzalez L, Guibelalde E, Fernandez JM, Ten JJ, "Radiation exposure to medical staff in interventional and cardiac radiology". *Br J Radiol*, 71(849):954–960,1998.
- [13] Koukorava C, Carinou E, Simantirakis G, Vrachliotis TG, Archontakis E, Tierris C et al, "Doses to operators during interventional radiology procedures: focus on eye lens and extremity dosimetry". *Radiat Prot Dosimetry*, 144(1–4):482–486,2011.
- [14] Dauer, L.T, "Exposed medical staff: challenges, available tools, and opportunities for improvement". *Health Physics*, 106(2):217–224,2014.
- [15] Dauer, L.T., Thornton R.H., "Comparing strategies for IR eye protection in the interventional suite". *Journal of Vascular and Interventional Radiology*, 21(11):1859-1861,2010.
- [16] Dauer, L.T., Thornton R.H., Solomon S.B., St.Germain J., "Unprotected operator eye lens doses in oncologic interventional radiology are clinically significant: estimates from patient kerma-area product data". *Journal of Vascular and Interventional Radiology*, 21(11):1703-1707,2010.
- [17] Dauer, L.T., et al., "Occupational radiation protection of pregnant or potentially pregnant workers in IR: a joint guideline of the Society for Interventional Radiology and the Cardiovascular and Interventional Radiological Society of Europe". *Journal of Vascular and Interventional Radiology*, 26:171-181,2015.

# Posters

# A Hybrid Computational Phantom for Out-of-Field Dose Calculation in Proton Therapy

Erika Kollitz <sup>1\*</sup>, Haegin Han <sup>2</sup>, Chan Hyeong Kim <sup>2</sup>, Clarissa Kroll <sup>1</sup>, Marco Riboldi <sup>1</sup>, Florian Kamp<sup>‡</sup>, Claus Belka<sup>‡</sup>, Wayne Newhauser <sup>4</sup>, Georgios Dedes <sup>1</sup>, and Katia Parodi <sup>1</sup>

<sup>1</sup>Experimental Physics - Medical Physics, Ludwig-Maximilians-Universität München (LMU Munich), Munich, Germany

<sup>2</sup>Nuclear Engineering, Hanyang University, Seoul, Republic of Korea

<sup>‡</sup>Department of Radiation Oncology, University Hospital, LMU Munich, Munich, Germany

<sup>4</sup>Physics and Astronomy, Louisiana State University (LSU), Baton Rouge, USA

\*Corresponding author: E.Kollitz@physik.uni-muenchen.de

**Abstract**—Modern clinical treatment planning fails to account for dose distributions over the whole body, however even low doses to the far field can result in a significant risk increase of developing second cancer. This work aims to create a custom hybrid whole body computational phantom that will improve the accuracy of out-of-field dose predictions. The hybrid phantom is composed of a scaled tetrahedral mesh reference phantom (based on the ICRP 110 adult reference phantoms) to represent out-of-field and patient computed tomography data for the in-field. This is of particular relevance for proton therapy, where the production of high energy neutrons means that there is a gap in knowledge regarding the potential risk of developing a second cancer for patients undergoing proton therapy. With this hybrid phantom, we aim to improve estimates of neutron dose in far field organs of interest accumulated during proton therapy. This computational framework has been integrated in Geant4 for coupling to an in-house treatment planning system (TPS) research engine. Initial results of the project, including validation of the proposed methodology, will be presented.

**Index Terms**— *Out-of-Field Dose, Mesh-type Reference Computational Phantom*

## I. INTRODUCTION

Voxel reference phantoms have some inherent disadvantages such as holes in organ surfaces at steep gradients and an inability to represent small anatomical structures accurately. To overcome these disadvantages, a tetrahedral polygon mesh type phantom has been developed [1]. Some of these Mesh-type Reference Computational Phantoms (MRCPs) have been created based on the ICRP 110 adult reference phantoms. These MRCPs are more easily deformable in orientation or scale, have continuous surfaces, and implement several structures too fine to be included in the ICRP 110 phantom (multiple skin layers, additional structures within the eye, etc.). The goal of this work is to utilize the MRCPs to create a patient specific computational phantom.

Survival of the primary cancer has continually increased as radiotherapy technology has improved and research has provided methods to create more effective treatment plans. Thus, a greater focus is now on patient quality of life post treatment, and minimizing the risks of radiation therapy such as heart disease and secondary cancers. A study from Diallo et. al showed that many of the secondary cancers are developed outside of the primary cancer treatment field, in the low dose area [2]. Clinical treatment planning systems (TPS) do not currently take this far field dose into account when optimizing treatment plans, nor can they even accurately predict the dose distribution far out-of-field [3]. By creating this custom extended computational phantom, we hope to create a manageable way to

elucidate the whole body dose distribution and dose to organs at risk outside the treatment field.

We chose to examine this hybrid phantom in the context of neutron dose received during proton therapy. The main benefits of proton therapy are based on the shape of the spread-out Bragg peak (SOBP), which applies an even dose throughout the tumor, lower dose proximal to the tumor, and nearly zero exit dose. However, the high energy protons required for treatment create neutrons within the treatment head and within the patient that can result in dose far from the treatment field. Furthermore, the variable biological effectiveness of neutrons introduces further uncertainty to the risks of proton therapy. This work aims to use the hybrid phantom to examine the distribution of neutron dose throughout the whole body so that future works can couple this with modern risk models to estimate the risk of secondary risk of cancer due to proton therapy, which in turn will be used to further optimize treatment planning to take into account the risk of developing a second malignancy.

## II. METHODS AND PRELIMINARY RESULTS

### A. Hybrid Phantom Components

The hybrid phantom is composed of three elements covering out-of-field, in-field, and a transitional border segment. The in-field segment of the phantom is represented by patient computed tomography (CT) data, the out-of-field by a patient-specific scaled MRCP, and a transition area created by voxelizing the MRCP at the in-field portion of the anatomy and registering it to the patient image. A flowchart describing the creation process is given in Figure 1.

### B. Voxelized MRCP Equivalence

As part of creating the transitional slices, we must verify that voxelizing the MRCP does not severely affect the dose distribution for a given beam in a given anatomy. To this end, four anatomical regions were selected (head, chest, abdomen, and pelvis) to test the conformity of the voxelization to the original MRCP. The tetrahedral mesh was initially voxelized to the same resolution as the ICRP 110 reference phantom (2.08 mm, 2.08 mm, 8 mm), but other voxel resolutions (slice thicknesses of 4 mm and 6 mm) were also tested.

A circular 140 MeV mono-energetic proton beam with a 5 cm radius was simulated using Geant4 version 10.02.p01. Command based scoring was used to tally total dose using the QGSP\_BIC\_HP physics list. Global gamma index analysis was used to quantitatively compare the simulated dose distributions from the original and voxelized MRCP (results in Table 1).

### C. Registering Voxelized MRCP Slices

We have devised and validated a method of excising any segment of the MRCP and voxelizing it to an arbitrary resolution, limited by

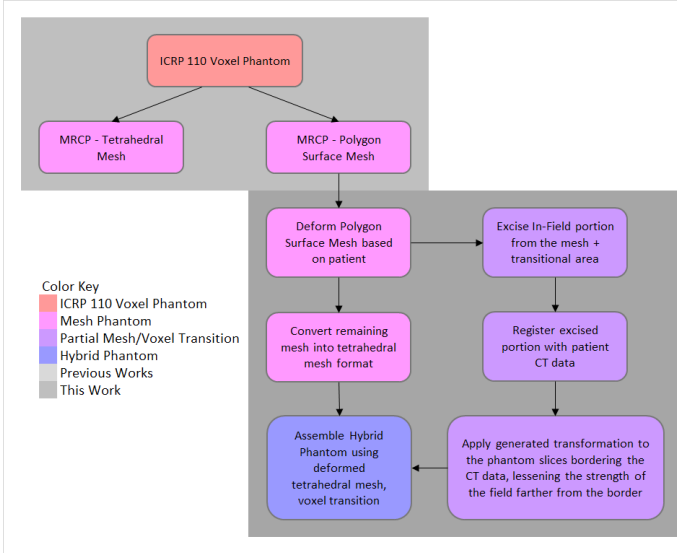


Fig. 1: Flowchart illustrating the hybrid phantom creation process

computation time. The algorithms being considered for deformable registration are b-spline with Plastimatch, Demons with BRAIN-STools, and Morphons with Reggui. Once the registration method is selected, the transform created by registering the voxelized MRCP to the CT data is then applied to the slices of the voxelized MRCP that border the imaged area. The farther the slices are from the edge of the image, the smaller the magnitude of the transform, facilitating a smoother transition from the true patient anatomy to the deformed MRCP.

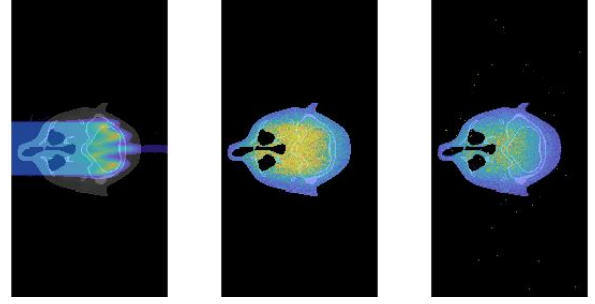
#### D. Assembling the Hybrid and Simulation Details

Once all hybrid phantom components are created, they are built using an in-house Geant4 code that can flexibly create sensitive detector geometries from multiple data source files. A clinically applicable treatment plan will be created using our in-house planning system and performed on a reference whole body CT, the hybrid phantom, the unadjusted MRCP, and an appropriately selected voxel-based library reference phantom. The dose tallied in individual organs (with a focus on those out-of-field) will be compared, and the alignment of the dose distributions will be examined using gamma index analysis.

The total and neutron dose is tallied. The default command-based neutron particle filter tallies the dose directly deposited by a neutron, however we wanted to track any dose which could be tracked back to a neutron. To this end, we have developed a custom filter for Geant4 that can be applied to any scorer, and that tags any neutron that is produced as well as any of its descendants. The custom filter was validated by checking that the tag was applied and counted throughout the full track history. An illustration of this custom filter is given in Figure 2, showing that the custom filter tallies more dose than the

TABLE I: Influence of voxel resolution on dose distribution: gamma index analysis for original vs voxelized MRCP

	Beam Position			
	Head	Chest	Abdomen	Pelvis
Slice Thickness (mm)				
8	.833	.880	.891	.889
6	.944	.965	.971	.975
4	.984	.984	.992	.995



(a) (color scale 2e-3 Gy) (b) (color scale 2e-6 Gy) (c) (color scale 2e-8 Gy)

Fig. 2: Comparison of dose tallies for (a) total dose, (b) custom neutron filter, and (c) default neutron filter, in the 4mm slice resolution phantom

default neutron filter, as expected since it tallies all dose which can be traced back to a neutron, and not just the direct dose from a neutron.

### III. CONCLUSION

The preliminary results of the hybrid phantom are promising, as the voxelization does not appear to cause any significant changes to dose prediction at the tested resolutions with slice thicknesses of 4-6 mm. Furthermore, the voxel resolution was limited for whole body voxelization due to computational limitations, but smaller segments can be voxelized at higher resolutions to better replicate the MRCP.

Further tests still need to be done regarding the scaling of the MRCP and the optimization of the deformable registration algorithm. However, a previous study from A. Zvereva et al. has shown in principle that scaling a reference phantom based on patient measurements can improve dose distribution accuracy [4], so this is not a significant concern. Each stage of the hybrid creation will be checked for improvement in accuracy (for example a scaled MRCP vs unscaled) prior to the creation of the final hybrid. This work postulates that the new hybrid phantom can improve predictions of neutron dose, especially out-of-field, during proton therapy, while maintaining high in-field accuracy. Next steps upon completion and validation of the hybrid phantom are for the Monte Carlo-based dose estimations produced in the hybrid to be coupled with various risk models to estimate the risk of secondary cancer due to the therapy, and this in turn will be used to further optimize treatment planning.

### ACKNOWLEDGMENT

The authors would like to thank Dipl. Math. Zankl, Dr. A. Kamp, and Dr. Giussani for advice and fruitful discussions. This work was supported by the German Research Foundation (DFG) within the Research Training Group GRK 2274.

### REFERENCES

- [1] Y. S. Yeom, H. Jeong, M. Han, and C. H. Kim, "Tetrahedral-mesh-based computational human phantom for fast monte carlo dose calculations," *Physics in Medicine and Biology*, vol. 59, May 2014.
- [2] I. Diallo, N. Haddy, E. Adjadj, A. Samand, E. Quiniou, J. Chavaudra, I. Alziar, N. Perret, S. Guérin, D. Lefkopoulou, and F. de Vathaire, "Frequency distribution of second solid cancer locations in relation to the irradiated volume among 115 patients treated for childhood cancer," *Int J Radiat Oncol Biol Phys*, vol. 74, pp. 876–83, July 2009.
- [3] L. Wilson and W. Newhauser, "A simple and fast physics-based analytical method to calculate therapeutic and stray doses from external beam, megavoltage x-ray therapy," *Physics in Medicine and Biology*, vol. 60, pp. 4753–4775, June 2015.
- [4] A. Zvereva, H. Schlattl, M. Zankl, J. Becker, N. Petoussi-Hens, Y. S. Yeom, C. H. Kim, C. Hoeschen, and K. Parodi, "Feasibility of reducing differences in estimated doses in nuclear medicine between a patient-specific and a reference phantom," *Physica Medica*, vol. 39, June 2017.

# Application of the Chinese reference adult computational phantoms to internal dosimetry: calculation of specific absorbed fractions for photons

Ruiyao Ma<sup>1,2</sup>, Rui Qiu<sup>1,2</sup>, Zhen Wu<sup>3</sup>, Chunyan Li<sup>3</sup> and Junli Li<sup>\*1,2</sup>

<sup>1</sup>. Department of Engineering Physics, Tsinghua University, Beijing, China

<sup>2</sup>. Key Laboratory of Particle & Radiation Imaging, Tsinghua University, Ministry of Education, Beijing, China

<sup>3</sup>. Joint Institute of Tsinghua University and Nuctech Company Limited, Beijing, China

\*Corresponding author: [lijunli@mail.tsinghua.edu.cn](mailto:lijunli@mail.tsinghua.edu.cn)

**Abstract**—In this work the Chinese reference adult computational phantoms were applied to internal dosimetry. A set of SAFs for photons were calculated with Monte Carlo method. The calculation results were compared with the results calculated based on mathematical phantom and ICRP/ICRU phantom. The difference of phantoms has a certain impact on the calculation results. SAFs obtained by this work is more suitable for the calculation of internal dose of Chinese people.

**Index Terms**—Chinese reference adult computational phantoms; SAFs; Monte Carlo simulation

## I. INTRODUCTION

The specific absorbed fractions (SAFs) are import parameters for calculation of the absorbed dose for internal emitters. Dose and Risk Calculation (DCAL) is an internal dosimetry software developed in the Life Science Division at Oak Ridge National Laboratory (ORNL). The SAFs used in the DCAL were calculated based on standard mathematical anthropomorphic phantoms [1]. To represent the anatomy structure of the human body more accurately, voxel computer phantoms were published by ICRP [2]. A set of SAFs were calculated using the ICRP/ICRU phantoms in 2010 by Hadid, L. et al. [3]. The ICRP phantoms represent the caucasian anatomy, which is different with the Chinese population. In this paper, Chinese reference adult computational phantoms were applied in calculation of specific absorbed fractions of energy for photons. The computer program was verified, and the results were compared with the results of Hadid, L. et al. and the SAFs of DCAL software.

## II. METHODS

### A. Chinese reference adult computational phantoms

Chinese reference adult male and female computational phantoms (CRAM and CRAF) were developed by our laboratory [4].

The height of the CRAM is 170 cm and the weight is 60 kg. For CRAF the height is 160 cm and the weight is 57.7 kg. These parameters are consistent with the Chinese national standards. The horizontal dimensions of CRAM voxel are

1.741 mm \* 1.741 mm, and the vertical dimensions are 1 mm, 3 mm and 5 mm respectively for head, torso and legs. For CRAF the horizontal dimensions of voxel are 0.613 mm \* 0.613 mm, and the vertical dimensions are 1.98 mm and 3.96 mm for head and under the head section.

There are more than 80 organs and tissues in CRAM and CRAF respectively, including almost all radiation sensitive organs required by the ICRP new recommendation. The mass of individual organs has been adjusted to the Chinese reference value with the difference less than 5%. Detailed skeleton and lung model are involved in CRAM and CRAF[4,5]. Special considerations were given to representing the gross spatial distribution of various bone constituents as realistically as possible during the construction of the site-specific skeleton. The detailed lung model includes completed 16-generation bronchial structure. The detailed breast model of CRAF is divided into skin, subcutaneous fat and fibrous gland, and the structures of fat, ducts and lobules in the fibrous glands are established.

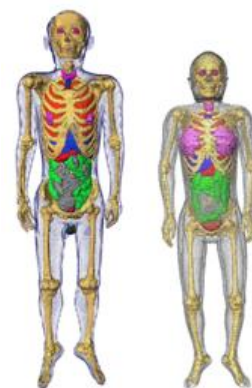


Figure 1. CRAM (left) and CRAF (right)

It is found the reference values of organ quality of CRAM and CRAF are quite different from the target organ of DCAL software. The SAFs were calculated by using the CRAM and CRAF, which can better represent the characteristics of Chinese people.

### B. Monte Carlo calculations and verification

The Monte Carlo simulation software Geant4 was used to simulate and calculate the SAFs of photons based on CRAM and CRAF. The emission position of the source particle is uniformly distributed in the source organ, and the emission direction is isotropic. The energies range from 0.01 MeV to 10 MeV. 33 source organs are considered in this work referring to the ICRP biodynamic model. According to the ICRP103 recommendation for sensitive organs or tissues, 15 target organs are involved in the simulation.

Hadid, L. et al. calculated the SAFs of protons and electrons using EGSncr Monte Carlo software based on the ICRP reference adult male phantom. To verify the SAF calculation program of this work, the same phantom was applied in the program processed by this work. And the results were compared with Hadid, L. et al.'s work. The SAFs calculated with three source organs (lungs, thyroid and liver) and four target regions (lungs, colon wall, breasts and stomach wall) were compared. Some of the results are shown below. The calculation results of this work are in good agreement with the data in the literature.

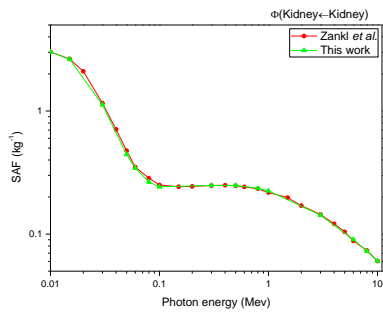


Figure 2. Verification of the calculation process: photons SAFs (Kidney ← Kidney) for the ICRP adult male phantom obtained in this work and reference.

### III. RESULTS

The photon SAFs were calculated for 33 source organs and 15 target organs of CRAM and CRAF for photon energy from 0.01 to 10 MeV. The results of this work were compared with the DCAL input data and Hadid, L. et al.'s results. Some of the results are shown below. When the source and target organ are the same organ, the difference of photon SAFs calculated by different models is not significant, and the difference is mainly caused by the difference of organ quality. When the source organ and target organ are different, the difference of relative position of organs in different models will also contribute to the difference of results. The photon SAFs from contents to organ wall were also analyzed, and the results of this work were consistent with those of the literature. Due to the involvement of detailed skeleton and lung model, the corresponding results were different from the literature. The differences were analyzed in the full paper.

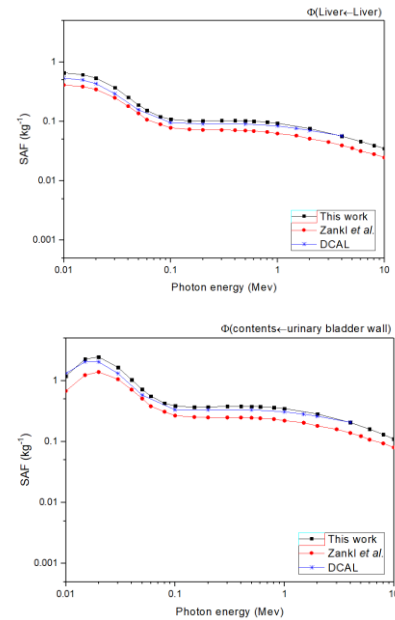


Figure 3. Photon SAFs for adult male (parts of the results)

### IV. CONCLUSION

CRAM and CRAF can represent the anatomical structure of Chinese adults more accurately compared to the standard mathematical anthropomorphic phantoms and ICRP phantoms. Application of the CRAM and CRAF to the calculation of SAFs can give a more complete and more accurate database for Chinese population. This set of SAFs provides key parameters for the calculation of the conversion coefficient of internal exposure dose. It is of great significance for the assessment of internal dose assessment for Chinese population with SAFs calculated by this work.

### ACKNOWLEDGMENT

This work was supported by the National Natural Science Foundation of China [Grant No. 11875036] and Tsinghua University Initiative Scientific Research Program [20151080355].

### REFERENCES

- [1] Eckerman K F, Leggett R W, Cristy M, et al. User's Guide to the DCAL System, *Ornl/tm*, 33(4), 1-2, 1993.
- [2] ICRP, "Adult reference computational phantoms: ICRP Publication 110," *Annals of the ICRP*, vol.39(2). 1-164, 2009.
- [3] Hadid, L., Desbrée, A, Schlattl, H., Franck, D., Blanchardon, E., & Hadid, L., M. "Application of the icrp/icru reference computational phantoms to internal dosimetry: calculation of specific absorbed fractions of energy for photons and electrons," *Physics in Medicine and Biology*, 55(13), 3631-3641, 2010.
- [4] Liu, L., Zeng, Z., Li, J., Qiu, R., Zhang, B., Ma, J., et al. "Organ dose conversion coefficients on an icrp-based chinese adult male voxel model from idealized external photons exposures," *Physics in Medicine and Biology*, 54(21), 6645-6673. 2009.
- [5] Hongyu Zhu et al., Establishment of detailed respiratory tract model and Monte Carlo simulation of radon progeny caused dose, CP2017

# Creation of a set of computational phantoms including clinical task for optimization studies in chest radiography

Sunay Rodríguez Pérez<sup>1,2\*</sup>, Dayana Castillo Seoane<sup>1</sup>, Lara Struelens<sup>1</sup>, Hilde Bosmans<sup>2,3</sup>, Nicholas W. Marshall<sup>2,3</sup>

<sup>1</sup>\* SCK•CEN, Research in Dosimetric Applications, Boeretang 200, 2400 Mol, Belgium

<sup>2</sup> KU Leuven, Medical Physics & Quality Assessment Group, Herestraat 49, B-3000 Leuven, Belgium

<sup>3</sup> UZ Gasthuisberg, Department of Radiology, Herestraat 49, B-3000 Leuven, Belgium

\*Corresponding author: srperez@sckcen.be

## I. INTRODUCTION

Optimization in diagnostic radiology is intended to ensure sufficient image quality to achieve the clinical outcome while keeping the patient exposure as low as possible. Different clinical imaging tasks demand different levels of image quality, therefore optimization in digital radiology should be linked to the clinical task. Computer simulations provide a practical, inexpensive and flexible way to investigate every element of the imaging chain. Realistic computational models of patient anatomy can be used as input for the simulations, in which the variability in the human anatomy and the different pathologies and devices can be included. This makes computer simulations powerful tools for dose and image quality assessment in diagnostic radiology.

This work aims to create a set of clinical tasks commonly found in chest radiography, which are modelled within two computational thorax phantoms. These models are meant to be used in a simulation framework for task-based optimization in chest radiography.

## II. METHODS AND RESULTS

### A. Lungman phantom

The Lungman is a physical thorax anthropomorphic phantom (Kyoto Kagaku, Japan). To create a computational model of the Lungman, we started from the segmentation of its 3D image dataset. Segmented organs were then converted to polygonal mesh format and processed by means of 3D graphic modelling software. Mesh modelling allowed improving the airway structures and correct staircasing artefacts coming from the segmentation (Figure 1) [1]. Although the phantom does not represent very accurately the human anatomy, the possibility to have the physical version for further validation of computer simulations was an important factor in our study. The physical phantom includes additional chest plates to simulate different body thicknesses, which were also included in the computational version.

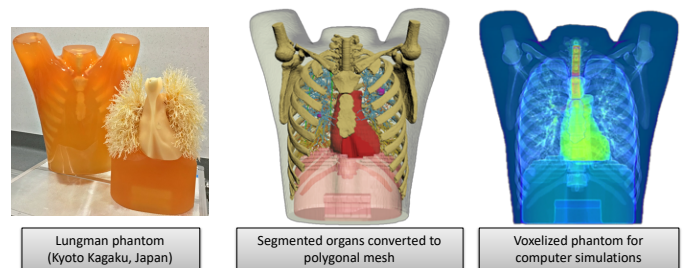


Figure 1. Lungman phantom

### B. RAF phantom

The Realistic Anthropomorphic Flexible (RAF) phantom is a full body male phantom. The phantom was developed by Lombardo et al [2] using polygonal mesh modelling. Different from the Lungman, this phantom does not have a physical version, but it provides a more realistic anatomy. To be used for image simulation of the chest some adaptations were necessary. A more realistic lung background was developed and only the organs within the chest were selected for this study. Because of its flexibility the arms could be adapted to patient equivalent position during a Posterior Anterior (PA) chest examination (Figure 2). A female version was created by including breast and three patient thicknesses for the male version were simulated (normal, obese and overweight).

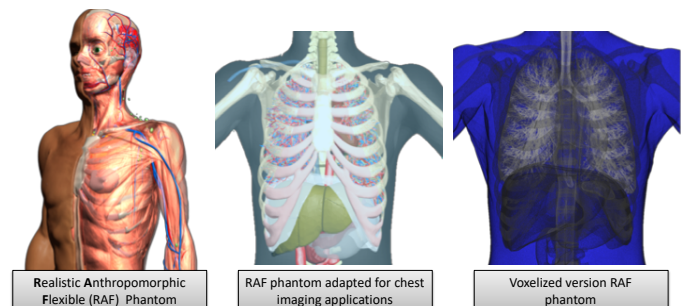


Figure 2. RAF phantom.

### C. Creation of clinical tasks within the phantom models

A wide variety of clinical tasks were added to the Lungman and the RAF phantom. Several phantom models were developed featuring pathologies like: lung nodules, rib fractures, spine compression, pneumothorax, haemothorax, pulmonary consolidation, heart enlargement, and medical devices such as catheters (Figure 3). Task modelling was supported by an experienced radiologist, especially in the case selection and task positioning within the model in order to make them clinically realistic.

Synthetic radiographic images of these phantoms were created using a hybrid simulation framework. The framework combines Monte Carlo simulations, ray tracing techniques and sharpness and noise modification routines. To be used in the simulations the phantom models were previously voxelized. Images include real noise and sharpness characteristics measured in a digital detector (Figure 4).

### III. CONCLUSION

A database of anthropomorphic chest phantoms including a range of clinical tasks was created. These models are being used in imaging simulation of the chest. They are ready for practical applications, such as virtual clinical trials to improve the impact of technology on radiologists' performance.

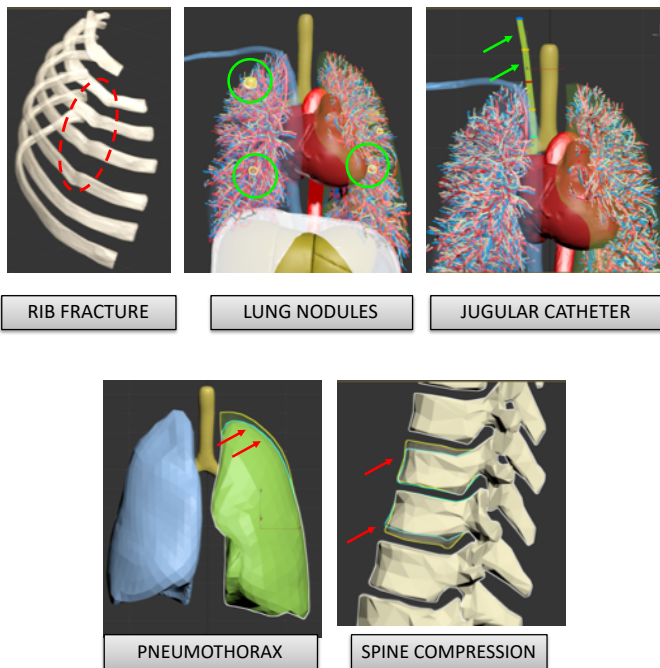


Figure 3. Example clinical tasks: ribs fracture, lung nodules, catheter, pneumothorax and spine compression.

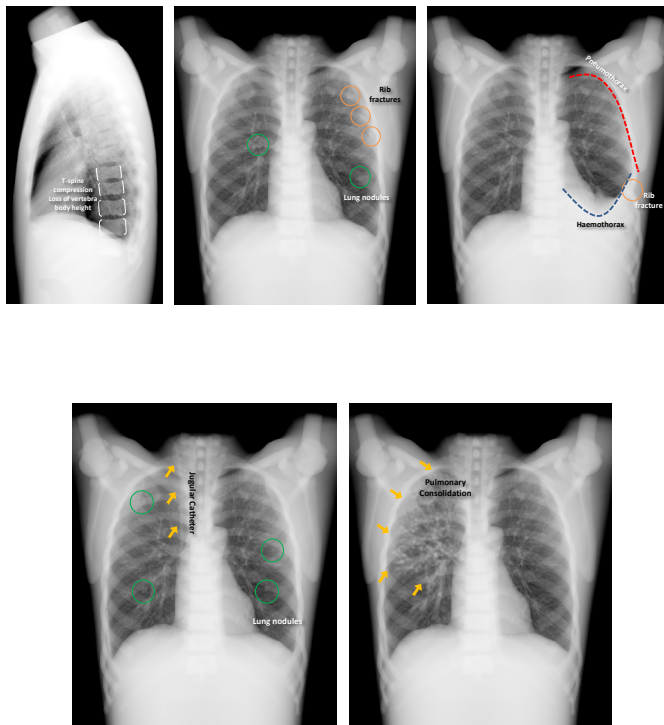


Figure 4. Synthetic radiographic images including a set of clinical tasks.

### ACKNOWLEDGMENT

Authors would like to thank Prof. Johan Coolen for the feedback given in the clinical task creation process and to Pasquale Lombardo for providing the RAF phantom.

### REFERENCES

- [1] S. Rodríguez Pérez, N W Marshall, L Struelens, H Bosmans. "Characterization and validation of the thorax phantom Lungman for dose assessment in chest radiography optimization studies," J. Med. Imaging 5(01), 2018.
- [2] P A. Lombardo, F Vanhavere, A L. Lebacqz, L Struelens, and R Bogaerts. "Development and Validation of the Realistic Anthropomorphic Flexible (RAF) Phantom" Health Phys., 114(5), pp 486-499, 2018.